

Computational Modeling of Strong and Weak Discontinuities

vom Fachbereich Maschinenbau und
Verfahrenstechnik der Universität Kaiserslautern
zur Verleihung des akademischen Grades
Doktor–Ingenieur (Dr.–Ing.)
genehmigte Dissertation

von
Dipl.–Ing. Julia Mergheim
aus Bochum

| | |
|----------------|---|
| Hauptreferent: | Prof. Dr.–Ing. P. Steinmann |
| Korreferenten: | JP Dr.–Ing. E. Kuhl Prof. Dr.–Ing. P. Hansbo |
| Vorsitzender: | Prof. Dr.–Ing. habil. D. Eifler |
| Dekan: | Prof. Dr.–Ing. J. C. Aurich |

| | |
|-------------------------|-------------------|
| Tag der Einreichung: | 05. Oktober 2005 |
| Tag der mündl. Prüfung: | 19. Dezember 2005 |

Kaiserslautern, März 2006

D 386

Vorwort

Die vorliegende Arbeit entstand während meiner Zeit als Stipendiatin im DFG Graduiertenkolleg *Ingenieurmaterialien auf verschiedenen Skalen: Experiment, Modellierung und Simulation* an der TU Kaiserslautern. Ich war in den Jahren von 2002 bis 2005 am Lehrstuhl für Technische Mechanik tätig. Die finanzielle Unterstützung der DFG im Rahmen des Graduiertenkollegs ermöglichte erst diese Arbeit.

Besonders herzlich möchte ich Herrn Professor Steinmann danken, der es mir ermöglicht hat, diese Arbeit erfolgreich durchzuführen. Herr Professor Steinmann hat mich konsequent unterstützt und gefördert und mir trotzdem die nötige wissenschaftliche Freiheit eingeräumt. Seine kreativen Vorschläge und Anregungen waren ausschlaggebend für das Gelingen dieser Arbeit.

Frau JP Kuhl möchte ich für die intensive Betreuung in den letzten drei Jahren danken. Zahlreiche motivierende Gespräche und ihr großes Interesse an meiner Arbeit haben entscheidend zum erfolgreichen Abschluss dieser beigetragen. Herrn Professor Hansbo danke ich sehr herzlich für die Übernahme des Korreferats und die zügige Begutachtung der Arbeit.

Sehr wichtig in der Zeit in Kaiserslautern waren meine Kollegen vom Lehrstuhl für Technische Mechanik. Ich möchte mich bei allen LTMLern für ihre Hilfsbereitschaft und die angenehme Arbeitsatmosphäre bedanken. Ein besonderer Dank für anregende Diskussionen und motivierende Kaffeepausen gilt Grieta Himpel, Ellen Kuhl, Ralf Denzer, Gunnar Possart, Andreas Menzel, Swantje Bargmann und Sigrid Leyendecker.

Meiner Familie danke ich für ihre Unterstützung während meiner ganzen Ausbildung. Besonders herzlich danke ich meinem Freund Christopher für seine Unterstützung und Geduld.

Einleitung

Ziel dieser Arbeit ist die Entwicklung und Analyse von neuartigen Finite Element Ansätzen zur Berücksichtigung von Diskontinuitäten. Bei numerischen Simulationen mit Hilfe der Finiten Element Methode war die Abbildung von Diskontinuitäten lange Zeit durch die zu Grunde liegende Vernetzung eingeschränkt. Unter dem Begriff Diskontinuitäten werden im Rahmen dieser Arbeit starke und schwache Diskontinuitäten zusammengefasst. Starke Diskontinuitäten bezeichnen Sprünge im Verschiebungsfeld, also das Auftreten von Rissen. Der Begriff schwache Diskontinuität bedeutet, dass ein Sprung im Gradienten des Verschiebungsfeldes also in den Verzerrungen auftritt. Dieses ist zum Beispiel der Fall bei unterschiedlichen Materialien, Einschlüssen oder Löchern innerhalb einer Struktur.

Im Rahmen der klassischen Finiten Element Methode können solche Diskontinuitäten nur entlang von Elementgrenzen berücksichtigt werden. Das führt offensichtlich zu netzabhängigen Lösungen oder erfordert eine ständige Neuvernetzung der Struktur. Um diese Einschränkungen der Finiten Element Methode aufzuheben, werden in der vorliegenden Arbeit diskontinuierliche Finite Element Ansätze entwickelt. Diese werden sowohl zur Modellierung und Simulation von Versagensvorgängen und Rissfortschritt, als auch zur netzunabhängigen Simulation von Materialgrenzen und Einschlüssen herangezogen.

Die maximal aufnehmbare Belastung einer Struktur ist durch das Entstehen von Versagenszonen begrenzt, die in spröden Materialien durch das Auftreten von Rissen gekennzeichnet sind. Der Versagensvorgang geht mit einer Entfestigung des Materials durch Schädigung und Bildung von Mikrorissen einher. Sobald eine kritische Belastung überschritten wird, nimmt die aufnehmbare Last bei weiterer Deformation ab, bis die Struktur letztendlich versagt. Zur Beschreibung von Versagensvorgängen sind in der Vergangenheit kontinuierliche und diskontinuierliche numerische Methoden untersucht worden. In den kontinuierlichen Ansätzen wird das Verschiebungsfeld als kontinuierlich angesehen und entfestigendes Materialverhalten, welches den Versagensvorgang einleitet, wird mit Hilfe spezieller konstitutiver Gesetze beschrieben. Dieses Verfahren hat den Vorteil, dass numerische Analysen in einem kontinuierlichen Rahmen möglich sind. Allerdings ist bekannt, dass Regularisierungen der Kontinuumsformulierung (z. B. nicht-lokale oder gradientenerweiterte Ansätze) nötig sind, um eine Netzabhängigkeit numerischer Lösungen beim Übergang zu lokalisiertem Versagen zu vermeiden. Betrachtet man die Ausdehnung der Versagenszone und den Versagensvorgang bis hin zu diskreten Rissen, so liegt es nahe, diskontinuierliche Ansätze zu verwenden. Durch die Einführung einer Diskonti-

nuität im Verschiebungsfeld wird eine realistischere Beschreibung des postkritischen Verhaltens ermöglicht. Die konstitutive Beschreibung inelastischen Materialverhaltens wird durch die Einführung von Traktions-Separations-Beziehungen entlang der Diskontinuität ermöglicht.

Die numerische Umsetzung des diskontinuierlichen Modells erfolgt in zwei Schritten. Zunächst wird ein Ansatz zur Beschreibung von Versagensvorgängen entwickelt, bei dem die Diskontinuitäten auf die Elementgrenzen beschränkt sind. Wenn die Versagensgeometrie a priori bekannt ist, können Interface Elemente entlang dieser Versagenszone eingesetzt werden. Im vorkritischen Bereich wird die Kontinuität des Verschiebungsfeldes mit Hilfe der diskontinuierlichen Galerkin Methode erzwungen, im postkritischen Bereich beschreibt ein phänomenologisches Traktions-Verschiebungs-Gesetz das entfestigende Materialverhalten.

Bei der Simulation von sich ausbreitenden Diskontinuitäten ist im Allgemeinen allerdings die Versagenszone nicht a priori bekannt. Aus diesem Grund wird eine Methode mit diskontinuierlichen Elementansätzen entwickelt, die das Auftreten von Diskontinuitäten innerhalb der Elemente ermöglicht. Dabei werden in den diskontinuierlichen Elementen zusätzliche Freiheitsgrade an den schon bestehenden Knoten eingeführt. Das führt sozusagen zu einer Verdoppelung des Elements und ermöglicht somit die Approximation von zwei unabhängigen Feldern. Bei der Integration der Gleichungen wird jeweils nur ein Teil des Elements berücksichtigt. Dies erfolgt über die Formulierung diskontinuierlicher Ansatzfunktionen, die identisch mit den normalen Ansatzfunktionen sind, allerdings jeweils auf einer Seite der Diskontinuität den Wert Null annehmen. Um die Ausbreitung des Risses zu beschreiben, werden ein Versagenskriterium und eine Methode zur Bestimmung der Rissrichtung benötigt. Dazu wird ein Hauptspannungskriterium herangezogen. Wird die Festigkeit des Materials überschritten, so wird die Diskontinuität verlängert. Zur Richtungsbestimmung wird ein gewichtetes Mittel der Spannungen im Bereich der Risspitze gebildet.

Der beschriebene Ansatz wird für geometrisch lineare und nichtlineare Problemstellungen spezifiziert. Die Erweiterung für den geometrisch nichtlinearen Rahmen bringt die Berücksichtigung unterschiedlicher kinematischer Beziehungen mit sich. Die Definition der Diskontinuitätsfläche ist innerhalb der geometrisch nichtlinearen Theorie in der verformten Konfiguration nicht mehr eindeutig. Zur Formulierung von Traktions-Verschiebungs-Beziehungen muss aus diesem Grund eine fiktive Diskontinuitätsfläche eingeführt werden. Des Weiteren muss die Änderung des räumlichen Normalenvektors auf diese Diskontinuitätsfläche bei der Formulierung von Traktions-Verschiebungs-Beziehungen und deren Linearisierung berücksichtigt werden.

Die numerische Umsetzung dieses Ansatzes erfolgt für zwei und drei dimensionale Problemstellungen. Dabei erfordert die Einführung neuer Freiheitsgrade, die geometrische Beschreibung des Risses und die Integration der diskontinuierlichen Elemente besondere

Methoden. Die Einführung neuer Freiheitsgrade erfolgt am Ende eines Lastschritts, falls das Versagenskriterium überschritten wird. Die Beschreibung der Rissgeometrie erfolgt durch die Identifizierung der Schnittpunkte der Elementkanten mit der Diskontinuitätsfläche. Diese werden auch zur Integration der diskontinuierlichen Elemente herangezogen.

Die Leistungsfähigkeit der entwickelten Methode wird mit Hilfe von zwei und drei dimensional Beispielen verdeutlicht. Dabei wird insbesondere die Unabhängigkeit der Resultate von der räumlichen Diskretisierung gezeigt.

Die diskontinuierlichen Elemente werden außerdem zur netzunabhängigen Simulation von schwachen Diskontinuitäten verwendet. Wie bereits erwähnt werden damit Sprünge im Verzerrungsfeld bezeichnet. Werden Strukturen, die aus verschiedenen Materialien zusammengesetzt sind oder Einschlüsse aufweisen, betrachtet, so ist das Verschiebungsfeld kontinuierlich, das Verzerrungsfeld weist allerdings Sprünge entlang der Materialgrenzen auf. Im Rahmen der Finite Element Methode werden diese schwachen Diskontinuitäten normalerweise durch die Vernetzung berücksichtigt. Werden allerdings Strukturen mit vielen Einschlüssen oder komplizierten Geometriebedingungen betrachtet, so kann es von Vorteil sein, wenn diese nicht explizit vernetzt werden müssen. Dies gilt ebenfalls für sich bewegende Interfaces, z. B. bei Phasentransformationen.

Da die diskontinuierlichen Elemente sowohl Sprünge in den Verschiebungen als auch in den Verzerrungen zulassen, aber nur Letzteres erwünscht ist, wird zusätzlich eine Methode benötigt, die die Kontinuität des Verschiebungsfeldes sicherstellt. Dazu wird die diskontinuierliche Galerkin Methode angewandt. Durch zusätzliche Terme in der schwachen Formulierung wird ähnlich einer konsistenten Penalty-Methode der Sprung im Verschiebungsfeld zu Null erzwungen. Innerhalb der diskontinuierlichen Elemente sind allerdings die Verzerrungen auf beiden Seiten der Diskontinuität unabhängig voneinander, so dass die schwache Diskontinuität abgebildet werden kann. Die diskontinuierliche Galerkin Methode wird auf die geometrisch nichtlineare Theorie erweitert.

Die Geometrie der Interfaces wird mit Hilfe von Level Set Funktionen beschrieben. Dabei wird die Kontur des Interfaces durch die Nullstellen einer Funktion, die eine Dimension höher ist, dargestellt. Im Rahmen der Finiten Element Diskretisierung wird durch die diskrete Level Set Funktion ermöglicht, die diskontinuierlichen Elemente zu identifizieren. Die Leistungsfähigkeit des beschriebenen Ansatzes wird mittels numerischer Beispiele verifiziert. Dabei werden im Rahmen der geometrisch linearen Theorie numerische Konvergenzstudien im Vergleich mit analytischen Lösungen durchgeführt. Die Ergebnisse zeigen, dass mit der bereitgestellten Methode die netzunabhängige Simulation von schwachen Diskontinuitäten ermöglicht wird.

Contents

| | |
|---|-----------|
| 1. Introduction | 1 |
| 2. A hybrid dG/interface method | 5 |
| 2.1. Motivation | 5 |
| 2.2. Kinematics | 7 |
| 2.3. Governing equations | 7 |
| 2.3.1. Strong form of the boundary value problem | 8 |
| 2.3.2. Discontinuous Galerkin method | 8 |
| 2.3.3. Interface approach | 10 |
| 2.3.4. Hybrid dG/interface approach | 11 |
| 2.4. Discretization and linearization | 11 |
| 2.4.1. Spatial discretization | 12 |
| 2.4.2. Discrete weak form | 12 |
| 2.4.3. Penalty parameter | 14 |
| 2.5. Implementation | 14 |
| 2.6. Numerical examples | 16 |
| 2.6.1. Mode I failure | 16 |
| 2.6.2. Mixed mode failure | 16 |
| 2.7. Summary | 17 |
| 3. Mesh-independent modeling of strong discontinuities | 19 |
| 3.1. Motivation | 19 |
| 3.2. Kinematics | 22 |
| 3.2.1. Continuous kinematics | 22 |
| 3.2.2. Strong discontinuity kinematics | 23 |
| 3.3. Variational formulation | 24 |
| 3.3.1. Principle of stationary potential energy | 24 |
| 3.3.2. Governing equations | 25 |
| 3.4. Constitutive equations | 25 |
| 3.4.1. Continuous constitutive law | 25 |
| 3.4.2. Cohesive crack concept | 26 |
| 3.5. Discretization and linearization | 28 |
| 3.5.1. Formulation of a discontinuous element | 28 |

| | | |
|-----------|--|-----------|
| 3.5.2. | Discrete weak formulation | 30 |
| 3.5.3. | Linearized discrete weak formulation | 31 |
| 3.6. | Implementation | 32 |
| 3.6.1. | Propagation of the discontinuity | 32 |
| 3.6.2. | Additional nodes | 33 |
| 3.6.3. | Integration scheme | 34 |
| 3.7. | Numerical examples | 35 |
| 3.7.1. | Mode I failure | 35 |
| 3.7.2. | Three-point bending beam | 37 |
| 3.8. | Summary | 39 |
| 4. | Mesh-independent modeling of weak discontinuities | 41 |
| 4.1. | Motivation | 41 |
| 4.2. | Kinematics | 43 |
| 4.3. | Variational formulation | 43 |
| 4.3.1. | Principle of stationary potential energy | 44 |
| 4.4. | Constitutive equation | 45 |
| 4.5. | Discretization | 46 |
| 4.5.1. | Discontinuous elements | 46 |
| 4.5.2. | Discrete weak formulation | 47 |
| 4.6. | Implementation | 47 |
| 4.6.1. | Geometric description of the interface | 47 |
| 4.6.2. | Additional nodes | 48 |
| 4.7. | Numerical examples | 49 |
| 4.7.1. | Bimaterial bar | 49 |
| 4.7.2. | Circular plate with inclusion | 51 |
| 4.8. | Summary | 53 |
| 5. | Mesh-independent modeling of strong discontinuities at finite strains | 55 |
| 5.1. | Motivation | 55 |
| 5.2. | Kinematics | 57 |
| 5.2.1. | Continuous kinematics | 57 |
| 5.2.2. | Strong discontinuity kinematics | 59 |
| 5.2.3. | Definition of the fictitious discontinuity surface | 61 |
| 5.3. | Variational formulation | 63 |
| 5.3.1. | Strong form of the boundary value problem | 63 |
| 5.3.2. | Weak formulation in material configuration | 63 |
| 5.3.3. | Weak formulation in spatial configuration | 64 |
| 5.3.4. | Linearization | 65 |
| 5.4. | Constitutive equations | 68 |

| | |
|---|------------|
| 5.4.1. Hyperelasticity | 68 |
| 5.4.2. Cohesive constitutive law | 70 |
| 5.5. Discretization and linearization | 74 |
| 5.5.1. Formulation of a discontinuous element | 74 |
| 5.5.2. Discrete weak formulation | 74 |
| 5.5.3. Linearized discrete weak formulation | 76 |
| 5.6. Implementation | 77 |
| 5.6.1. Splitting of elements | 78 |
| 5.6.2. Numerical integration | 78 |
| 5.6.3. Crack propagation and crack path representation | 80 |
| 5.6.4. Algorithmic implementation | 81 |
| 5.7. Numerical examples | 82 |
| 5.7.1. Two dimensional crack propagation | 83 |
| 5.7.2. Three dimensional crack propagation | 86 |
| 5.8. Summary | 90 |
| 6. Mesh-independent modeling of weak discontinuities at finite strains | 91 |
| 6.1. Motivation | 91 |
| 6.2. Kinematics | 92 |
| 6.3. Variational formulation | 93 |
| 6.3.1. Principle of stationary potential energy | 93 |
| 6.3.2. Linearization | 95 |
| 6.4. Constitutive equation | 95 |
| 6.5. Discretization and linearization | 96 |
| 6.5.1. Discrete weak formulation | 97 |
| 6.5.2. Linearized discrete weak formulation | 98 |
| 6.6. Implementation | 98 |
| 6.7. Numerical examples | 99 |
| 6.7.1. Bimaterial bar | 100 |
| 6.7.2. Plate with inclusion | 102 |
| 6.8. Summary | 103 |
| 7. Conclusions | 105 |
| A. Miscellaneous | 107 |
| A.1. Notation | 107 |
| A.2. Derivatives | 108 |
| A.3. Jump and average terms | 108 |

| | |
|--|------------|
| B. Numerical study of the dG method for linear elasticity | 109 |
| B.1. DG method for linear elasticity | 109 |
| B.2. Numerical example | 109 |
| C. Application of the Material Force Method | 113 |
| C.1. Motivation | 113 |
| C.2. Material Force Method | 114 |
| C.3. Numerical example | 116 |
| . Bibliography | 118 |

1. Introduction

Discontinuities can appear in different fields of mechanics. Some examples where discontinuities arise are more obvious such as the formation of cracks. Other sources of discontinuities are less apparent such as interfaces between different materials. Furthermore continuous fields with steep gradients can also be considered as discontinuous fields. This work aims at the inclusion of arbitrary discontinuities within the finite element method. Although the finite element method is the most sophisticated numerical tool in modern engineering, the inclusion of discontinuities is still a challenging task. Traditionally within the framework of FE methods discontinuities are modeled explicitly by the construction of the mesh. Thus, when a fixed mesh is used, the position of the discontinuity is prescribed by the location of interelement boundaries and not by the physical situation. The simulation of crack growth requires a frequent adaption of the mesh and that can be a difficult and computationally expensive task. Thus a more flexible numerical approach is needed which leads to the mesh-independent representation of the discontinuity.

A challenging field where the accurate description of discontinuities is of vital importance is the modeling of failure in engineering materials. The load capacity of a structure is limited by the material strength. If the load limit is exceeded failure zones arise and increase. Representative examples of failure mechanisms are cracks in brittle materials or shear bands in metals or soils. Failure processes are often accompanied by a strain softening material behavior (decreasing load carrying capacity with increasing strain at a material point). It is known that the inclusion of strain softening material behavior within a continuum description requires regularization techniques to preserve the well-posedness of the governing equations. One possibility is the consideration of non-local or gradient terms in the constitutive equations but these approaches require a sufficiently fine discretization in the localization zone, which leads to a high numerical effort. If the extent of the failure zone and the failure process to the point of the development of discrete cracks is considered, it seems reasonable to include strong discontinuities. In the framework of fracture mechanics the inclusion of displacement jumps is intuitively comprehensible. However, the modeling of localized failure processes demands the consideration of inelastic material behavior. Cohesive zone models represent an approach which is especially suited for the incorporation within the finite element framework. It is supposed that cohesive tractions are transmitted between the discontinuity surfaces. These traction are constitutively prescribed by a phenomenological traction separation law and thus allow for the modeling of different inelastic mechanisms, like micro-crack evolution, initiation of voids, plastic flow or crack bridging. The incorporation of a displacement discontinuity

in combination with a cohesive traction separation relation leads to a sound model to describe failure processes and crack propagation.

Another area where the existence of discontinuities is not as obvious is the occurrence of material interfaces, inclusions or holes. The accurate modeling of such internal interfaces is important to predict the mechanical behaviour of components. The present discontinuity is of different nature: the displacement field is continuous but there is a jump in the strains, which is denoted by the expression weak discontinuity. Usually in FE methods material interfaces are taken into account by the mesh construction. But if structures exhibit multiple inclusions of complex geometry it can be advantageous if the interface does not have to be meshed. And when we look at problems where the interface moves with time, e. g. phase transformation, the mesh-independent modeling of the weak discontinuities naturally holds major advantages.

The greatest challenge in the modeling of discontinuities is their incorporation into numerical methods. The focus of the present work is the development, analysis and application of a finite element approach to model mesh-independent discontinuities. The method shall be robust and flexible to be applicable to both strong and weak discontinuities.

The present work is divided into seven chapters. The individual chapters, with the exception of the introduction in the present chapter and the conclusion in chapter 7, describe different approaches for the numerical treatment of strong or weak discontinuities in the framework of the finite element method. Each chapter is self-contained. Thus in each chapter the underlying kinematics, the balance equations, the constitutive equations and the numerical evaluation of the derived set of equations are defined. Consequently numerical examples are presented at the end of each chapter.

In the following chapter a hybrid discontinuous Galerkin/ interface method for the simulation of failure processes is introduced. The approach offers the possibility to simulate failure along well-defined surfaces, which occurs for example in the case of light-weight composite materials. Since the failure surface is known a priori, the use of interface elements, which are placed along the failure surface, represents the most natural choice. In contrast to usual interface methods the continuity of the solution in the precritical regime is here ensured in a weak sense by a discontinuous Galerkin method. In the post-failure state the behavior of the interface is constitutively determined, depending on the displacement jump.

In chapter 3 the restriction that the failure surface is known in advance is abolished. Thus a framework for the mesh-independent modeling of cohesive cracks is introduced. The emphasis of the chapter is on the formulation of discontinuous elements which allow for a discontinuity in the element. Additional degrees of freedom are placed at the existing nodes and a discontinuous set of basis functions is adopted to permit the simulation

of propagating cracks without remeshing. The inelastic fracture process is described by means of cohesive zone models. The numerical implementation of the novel finite element concept is described in detail and numerical examples demonstrate the ability of the approach to simulate mesh-independent discontinuities.

Chapter 4 combines particular parts of the previous chapters to an approach for the mesh-independent modeling of weak discontinuities. Weak discontinuities are present in the case of material interfaces or holes and inclusions. To simulate the resulting jump in the strains the discontinuous elements and the discontinuous Galerkin method are adopted. The discontinuous elements allow for arbitrary discontinuities and the discontinuous Galerkin method ensures the continuity of the displacement field in a weak sense. Thus only weak discontinuities remain.

In the following two chapters the approaches, introduced in the chapters 3 and 4 are extended to the geometrically nonlinear setting. Therefore the introduction of the nonlinear kinematics is a main part. Considering strong discontinuities the extension to nonlinear kinematics implies additional difficulties, concerning the definition of the discontinuity surface and the formulation and linearization of cohesive traction separation laws. In addition to the introduction of the geometrically nonlinear equations the approach is extended to three dimensional problems. The handling of the complex geometry of three dimensional crack modeling is specified and significant examples present the performance of the approach.

For the handling of weak discontinuities in chapter 6 the discontinuous Galerkin method is extended to finite strains. The same discontinuous elements as in the previous chapters are used. The continuous and discrete equations are specified and again the applicability of the concept in the geometrically nonlinear setting is demonstrated by numerical examples.

In the conclusions in chapter 7 the acquired results are summarized and complemented by suggestions about possible future work.

2. A hybrid dG/interface method

In the present chapter the computational modeling of failure along well-defined surfaces, which occur for example in the case of light-weight composite materials, is discussed. The chapter is mainly based on reference [80].

A hybrid method will be introduced which makes use of the discontinuous Galerkin method in combination with a finite element interface approach. Since it is assumed that the failure zone is known in advance interface elements can be placed along the known failure surface. The discontinuous Galerkin method is applied in the prefailure regime to avoid the unphysical use of penalty terms and instead to enforce the continuity of the solution along the interface weakly. Once a particular failure criterion is fulfilled, the behavior of the interface is determined constitutively, depending on the displacement jump. The applicability of the proposed method is illustrated by means of two computational model problems.

2.1. Motivation

The application of light-weight composite materials has become increasingly popular in recent years. The load carrying capacity of such composite structures is typically characterized through the failure of the weakest link, i.e. through the debonding of the adhesive layer in between two components or through the failure of the boundary layer very close to the adhesive. The accurate description of the delamination process can thus be considered the most essential ingredient in the design of composite structures. In [52] the failure process in fibre metal laminates is analyzed, in [108] computational strategies for composites are developed and in [1] an approach for the simulation of the delamination process in laminated composites is introduced.

When failure takes place along well-defined failure surfaces, the use of interface elements represents the most natural choice. In the case of pasted structures, for example, interfaces are placed in the adhesive layer. As soon as a particular failure criterion is met, the behavior of the interface is determined constitutively through a traction separation law whereby the interface traction is typically introduced as a nonlinear function of the displacement jump. The characterization of the postfailure regime is thus straightforward and well-accepted in the related literature. For example in [69] and [84] the localization of elastoplastic solids is simulated by means of interface elements. The numerical integration of interface elements is studied in detail in [109]. Furthermore interface elements with independent traction separation laws are applied for cohesive crack propagation in [137], [23]

and [101].

However, the classical treatment of the prefailure regime is rather ad hoc and somewhat inconsistent. Since the displacement field is double-valued at the interface, two finite element nodes have to be introduced at one material point. Traditionally, prior to failure, these two nodes are held together artificially with the help of a penalty method, whereby the choice of an appropriate penalty parameter is rather questionable.

The present chapter aims at deriving a consistent interface formulation by refraining from the use of penalty methods in the prefailure regime. Rather, we suggest the weak enforcement of continuity at the interface by making use of Nitsche's method [95], which can be seen as the origin of the discontinuous Galerkin methods. Nitsche introduced a method to enforce the Dirichlet boundary conditions in a weak sense. Later Douglas and Dupont [33], Arnold [6] and Wheeler [133] extended Nitsche's approach to the weak enforcement of the continuity of the solution at the interior boundaries. These methods are known as the interior penalty methods. In the last years the discontinuous Galerkin methods were extended and applied to various problems, see [26] for an overview and [7] for a unified analysis of different discontinuous Galerkin approaches for elliptic problems. Only recently the discontinuous Galerkin method gained an increased interest in the structural mechanics community through the work of Engel et al. [36], where a continuous/discontinuous approach was developed to solve fourth-order differential equations, e. g. problems concerning beams and plates and strain gradient elasticity. Based on this idea in [129] and [88] a dG method for strain gradient damage was proposed. Furthermore in [50] a discontinuous Galerkin method for incompressible elasticity was developed and in [49] a dG method for the plate equation is presented. In the chapters 4 and 6 the discontinuous Galerkin method is also adopted for the mesh-independent modeling of weak discontinuities. This weak enforcement of continuity, which has also been applied successfully in combination with domain decomposition techniques, see e. g. Becker, Hansbo and Stenberg [13], represents a consistent strategy to tie together pairs of finite element nodes at the interface prior to failure. Like in classical discontinuous Galerkin methods, the jump in the displacements is enforced to vanish in an integral sense. Double-valued fields are thus treated consistently in the present approach and the use of otherwise unphysical penalty parameters is only necessary to stabilize the method.

This chapter is organized as follows: Firstly we will review the kinematic relations of a geometrically linear solid, which exhibits a strong discontinuity surface. Then the governing equations are defined, the weak formulation of the discontinuous Galerkin method is formulated for linear elasticity and afterwards the weak formulation of the interface approach is derived. Based on the previous results the hybrid method is formulated. Some aspects of the spatial discretization and the implementation are highlighted. Finally two numerical examples are presented to demonstrate the applicability of the proposed hybrid method.

2.2. Kinematics

Let \mathcal{B} denote a linear elastic body with placements denoted by \mathbf{x} . The boundary $\partial\mathcal{B}$ with the outward unit normal vector \mathbf{n}_e is subdivided into the disjoint parts $\partial\mathcal{B} = \partial\mathcal{B}_u \cup \partial\mathcal{B}_t$ with $\partial\mathcal{B}_t \cap \partial\mathcal{B}_u = \emptyset$, where either Neumann or Dirichlet boundary conditions are prescribed. Since we assume that the potential failure zone is known we introduce an

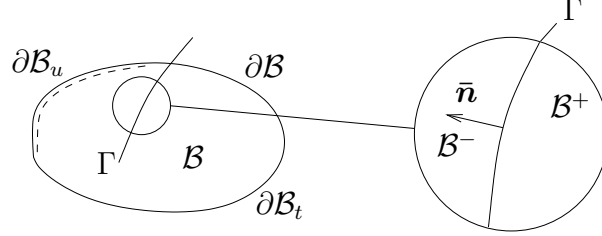


Figure 2.1.: \mathcal{B} crossed by an internal boundary Γ

internal surface Γ along this zone. The two resulting parts of the body are denoted by \mathcal{B}^+ and \mathcal{B}^- . We associate a unit normal vector $\bar{\mathbf{n}}$ and a tangential vector $\bar{\mathbf{m}}$ to Γ , compare figure 2.1. Thereby $\bar{\mathbf{n}}$ points from \mathcal{B}^- to \mathcal{B}^+ , thus $\bar{\mathbf{n}} = -\bar{\mathbf{n}}^+ = \bar{\mathbf{n}}^-$ and the associated tangential vector is denoted with $\bar{\mathbf{m}}$. The unknown displacement field \mathbf{u} is described separately in both parts of the body

$$\mathbf{u}(\mathbf{x}) = \begin{cases} \mathbf{u}^+(\mathbf{x}) & \text{in } \mathcal{B}^+ \\ \mathbf{u}^-(\mathbf{x}) & \text{in } \mathcal{B}^- \end{cases} \quad (2.2.1)$$

Consequently the symmetric strain tensor is also specified separately for \mathcal{B}^+ and \mathcal{B}^- as the symmetric part of the gradient of the displacement field

$$\boldsymbol{\epsilon} = \begin{cases} \boldsymbol{\epsilon}^+ = \frac{1}{2} [\nabla_{\mathbf{x}} \mathbf{u}^+ + \nabla_{\mathbf{x}}^t \mathbf{u}^+] \\ \boldsymbol{\epsilon}^- = \frac{1}{2} [\nabla_{\mathbf{x}} \mathbf{u}^- + \nabla_{\mathbf{x}}^t \mathbf{u}^-] \end{cases} \quad (2.2.2)$$

To treat the discontinuities we introduce a jump term term and an average term

$$\llbracket \mathbf{u} \rrbracket := \mathbf{u}_{|\Gamma}^+ - \mathbf{u}_{|\Gamma}^- \quad \{ \mathbf{u} \} := \frac{1}{2} [\mathbf{u}_{|\Gamma}^+ + \mathbf{u}_{|\Gamma}^-] \quad (2.2.3)$$

which are calculated by means of values of the field variable $\mathbf{u}_{|\Gamma}$ evaluated at the internal boundary Γ .

2.3. Governing equations

In the following the governing equations to describe a geometrically linear solid are reviewed. The equation of equilibrium combined with the boundary conditions leads to the

strong form of the boundary value problem. Due to the internal interface we need to define further interfacial conditions for the pre- and the postcritical regime. Based on the governing equations the weak formulations of the discontinuous Galerkin method, of the interface approach and of the hybrid approach are derived in the following.

2.3.1. Strong form of the boundary value problem

The equation of equilibrium and the boundary conditions are given by

$$\begin{aligned} -\operatorname{div} \boldsymbol{\sigma} &= \mathbf{b} && \text{in } \mathcal{B} \\ \mathbf{u} &= \mathbf{u}^p && \text{on } \partial\mathcal{B}_u \\ \boldsymbol{\sigma} \cdot \mathbf{n}_e &= \mathbf{t}^p && \text{on } \partial\mathcal{B}_t. \end{aligned} \tag{2.3.1}$$

Hereby $\boldsymbol{\sigma}$ denotes the symmetric Cauchy stress tensor. We consider linear elasticity and therefore the constitutive law, describing the stress strain relation is given by

$$\boldsymbol{\sigma} = \mathbf{C} : \boldsymbol{\epsilon}, \tag{2.3.2}$$

with \mathbf{C} being the fourth order constitutive tensor, depending on the material parameters, e.g. the Lamé parameters λ and μ . Furthermore \mathbf{b} denotes the body force, \mathbf{t}^p is the prescribed traction vector on the Neumann boundary and \mathbf{u}^p is the prescribed displacement on the Dirichlet boundary.

Additionally we need to define interfacial conditions at the internal boundary Γ . In the prefailure regime continuity of the displacement field and of the tractions is required, thus

$$[[\mathbf{u}]] = \mathbf{0} \quad \text{and} \quad [[\boldsymbol{\sigma}]] \cdot \bar{\mathbf{n}} = \mathbf{0} \quad \text{on} \quad \Gamma. \tag{2.3.3}$$

In the postfailure regime a jump in the displacement field can occur and the interfacial tractions are constitutively prescribed, depending on the size of the displacement jump. Therefore traction continuity is automatically ensured and the interfacial conditions are specified as

$$[[\mathbf{u}]] \neq \mathbf{0}, \quad \text{and} \quad \boldsymbol{\sigma}^+ \cdot \bar{\mathbf{n}} = \boldsymbol{\sigma}^- \cdot \bar{\mathbf{n}} = \bar{\mathbf{t}}([[\mathbf{u}]]) \quad \text{on} \quad \Gamma. \tag{2.3.4}$$

Starting from the strong form of the boundary value problem the weak formulations of the discontinuous Galerkin method, the interface approach and the resulting hybrid method are derived.

2.3.2. Discontinuous Galerkin method

In this section the modeling of the prefailure state with the discontinuous Galerkin method is described. In the prefailure regime the jump in the displacement field along Γ shall vanish. Therefore we apply the discontinuous Galerkin method to enforce the continuity

of the displacement field in a weak sense. In different analyses and applications of discontinuous Galerkin methods in elasticity, the dG terms are applied along all interelement boundaries. For example in [106] and [71] error estimates for different dG approaches in elasticity are considered. Locking-free dG approaches were introduced by Hansbo and Larson in [50] and by Wihler in [134]. A dG method to handle viscoelasticity can be found in [105]. In contrast to the mentioned methods in the present approach the additional dG terms are only used along the internal interface. The two continuous parts of the body are handled by a continuous Galerkin method.

In a similar way a Nitsche type discontinuous Galerkin method was applied as a mortaring method by Stenberg in [122] and as a domain decomposition method by Heinrich et al. in [54] and [53] and by Becker et al. in [13]. Different interface problems were addressed by Hansbo and co-workers in [46], [48] and [47].

To define the discontinuous Galerkin method we introduce the average tractions along Γ according to the definition of the average term (2.2.3) as,

$$\{\boldsymbol{\sigma}\} \cdot \bar{\mathbf{n}} := \frac{1}{2} [\boldsymbol{\sigma}|_{\Gamma^+} + \boldsymbol{\sigma}|_{\Gamma^-}] \cdot \bar{\mathbf{n}}. \quad (2.3.5)$$

To obtain the weak formulation of the boundary value problem, we multiply the strong form of the boundary value problem (2.3.1) with a test function $\delta \mathbf{u}$ and integrate by parts over \mathcal{B}^+ and \mathcal{B}^-

$$\begin{aligned} & \int_{\mathcal{B}^+ \cup \mathcal{B}^-} \delta \boldsymbol{\varepsilon} : \boldsymbol{\sigma}(\mathbf{u}) dV - \int_{\Gamma^+} \delta \mathbf{u}^+ \cdot \boldsymbol{\sigma}(\mathbf{u}^+) \cdot \bar{\mathbf{n}}^+ dA - \int_{\Gamma^-} \delta \mathbf{u}^- \cdot \boldsymbol{\sigma}(\mathbf{u}^-) \cdot \bar{\mathbf{n}}^- dA \\ &= \int_{\mathcal{B}^+ \cup \mathcal{B}^-} \delta \mathbf{u} \cdot \mathbf{b} dV + \int_{\partial \mathcal{B}_t} \delta \mathbf{u} \cdot \mathbf{t}^p dA, \end{aligned} \quad (2.3.6)$$

whereby the two sides of the internal interface Γ are considered separately. We recall the definition of the normal vector $\bar{\mathbf{n}}$ and obtain that

$$- \int_{\Gamma^+} \delta \mathbf{u}^+ \cdot \boldsymbol{\sigma}(\mathbf{u}^+) \cdot \bar{\mathbf{n}}^+ dA - \int_{\Gamma^-} \delta \mathbf{u}^- \cdot \boldsymbol{\sigma}(\mathbf{u}^-) \cdot \bar{\mathbf{n}}^- dA = \int_{\Gamma} \llbracket \delta \mathbf{u} \cdot \boldsymbol{\sigma}(\mathbf{u}) \rrbracket \cdot \bar{\mathbf{n}} dA. \quad (2.3.7)$$

With the following identity, which allows for the separation of the jump term of a product

$$\llbracket \delta \mathbf{u} \cdot \boldsymbol{\sigma} \rrbracket = \llbracket \delta \mathbf{u} \rrbracket \cdot \{\boldsymbol{\sigma}\} + \{\delta \mathbf{u}\} \cdot \llbracket \boldsymbol{\sigma} \rrbracket, \quad (2.3.8)$$

and provided that $\boldsymbol{\sigma} \cdot \bar{\mathbf{n}}$ is continuous over Γ , which means that $\llbracket \boldsymbol{\sigma} \rrbracket \cdot \bar{\mathbf{n}} = \mathbf{0}$, compare equation (2.3.3), we obtain

$$\int_{\mathcal{B}^+ \cup \mathcal{B}^-} \delta \boldsymbol{\varepsilon} : \boldsymbol{\sigma}(\mathbf{u}) dV + \int_{\Gamma} \llbracket \delta \mathbf{u} \rrbracket \cdot \{\boldsymbol{\sigma}(\mathbf{u})\} \cdot \bar{\mathbf{n}} dA = \int_{\mathcal{B}^+ \cup \mathcal{B}^-} \delta \mathbf{u} \cdot \mathbf{b} dV + \int_{\partial \mathcal{B}_t} \delta \mathbf{u} \cdot \mathbf{t}^p dA. \quad (2.3.9)$$

Since the resulting equation is neither symmetric nor stable so far, the term $\int_{\Gamma} \bar{\mathbf{n}} \cdot \{\delta \boldsymbol{\sigma}\} \cdot \llbracket \mathbf{u} \rrbracket dA$ is added to symmetrize the method. And furthermore, in terms of

Nitsche's method a penalty term $\int_{\Gamma} \theta \llbracket \delta \mathbf{u} \rrbracket \cdot \llbracket \mathbf{u} \rrbracket dA$, with θ being a penalty factor, depending on the mesh size h and the material parameters, is added to obtain a stabilized symmetric method.

$$\begin{aligned} & \int_{\mathcal{B}^+ \cup \mathcal{B}^-} \delta \boldsymbol{\epsilon} : \boldsymbol{\sigma} dV + \int_{\Gamma} \left[\llbracket \delta \mathbf{u} \rrbracket \cdot \{\boldsymbol{\sigma}\} \cdot \bar{\mathbf{n}} + \bar{\mathbf{n}} \cdot \{\delta \boldsymbol{\sigma}\} \cdot \llbracket \mathbf{u} \rrbracket \right] dA \\ & + \int_{\Gamma} \theta \llbracket \delta \mathbf{u} \rrbracket \cdot \llbracket \mathbf{u} \rrbracket dA = \int_{\mathcal{B}^+ \cup \mathcal{B}^-} \delta \mathbf{u} \cdot \mathbf{b} dV + \int_{\partial \mathcal{B}_i} \delta \mathbf{u} \cdot \mathbf{t}^p dA. \end{aligned} \quad (2.3.10)$$

Since nonstandard terms were added to the weak form, the consistency with the original equations has to be examined. As we consider a continuous displacement field \mathbf{u} , the jump in the displacements $\llbracket \mathbf{u} \rrbracket$ is equal zero along Γ . The additionally added terms, which do not automatically arise from the variational derivation, vanish and thus the resulting equation is consistent with equations (2.3.1) and (2.3.3). The formulation (2.3.10) assures the weak enforcement of the continuity of the solution along Γ , which is required in the precritical state.

2.3.3. Interface approach

A finite element interface formulation is applied to model the postcritical state, after a failure criterion has been met. The interface formulation accounts for strong discontinuities in the displacement field along the discontinuity surface Γ . The postcritical material behavior, namely the development of the discontinuities in the displacements, is governed by a constitutive traction separation law, which is defined independently of the constitutive behavior of the bulk.

Interface approaches were successfully applied to different problems, concerning crack propagation or localization and failure processes. In [137] crack growth in brittle solids was modeled, in [23] interface elements were used for the simulation of impact and damage, Ortiz et al. considered geometrically nonlinear crack growth in [101]. Due to the geometry of a localized failure zone, which is in one direction significantly thinner than in the other directions, interface approaches are also applied for the description of localization. In [70] the localization in metallic and granular materials is considered, in [84] an interface approach with an independent traction separation law was applied to localization in elastoplastic solids and in [69] an interface approach for capturing plastic localization was derived, which was in [119] extended to large strains.

In the same manner as before we consider an internal interface, but now the additional interface contribution does not depend on the stresses within the two parts of the body, but on constitutively prescribed tractions.

To develop the weak formulation of the interface approach, we start with the strong form of the boundary problem with the appropriate interface conditions (2.3.4). Recall that jumps of field quantities (\bullet) across Γ are denoted by $\llbracket (\bullet) \rrbracket = (\bullet)^+ - (\bullet)^-$. We then con-

clude that the test function or virtual displacement function $\delta \mathbf{u}$ exhibits a discontinuity $[[\delta \mathbf{u}]]$ along Γ . Taking into account that $\bar{\mathbf{t}}$ is continuous along Γ , compare equation (2.3.4), we obtain the weak formulation of the interface approach with an additional contribution due to the tractions along the interface

$$\int_{\mathcal{B}^+ \cup \mathcal{B}^-} \delta \epsilon : \boldsymbol{\sigma}(\mathbf{u}) dV + \int_{\Gamma} [[\delta \mathbf{u}]] \cdot \bar{\mathbf{t}}([[\mathbf{u}]]) dA = \int_{\mathcal{B}^+ \cup \mathcal{B}^-} \delta \mathbf{u} \cdot \mathbf{b} dV + \int_{\partial \mathcal{B}_t} \delta \mathbf{u} \cdot \mathbf{t}^p dA. \quad (2.3.11)$$

The relation of the traction vector $\bar{\mathbf{t}}$ and the jump of the displacements $[[\mathbf{u}]]$ describes the failure behavior of the interface. Here the constitutive law of the interface is chosen independently of the constitutive setting of the surrounding domain. An exponential softening of the material is assumed in the postcritical state and can be formulated as

$$\bar{t}_n([[\mathbf{u} \cdot \bar{\mathbf{n}}]]) = t_n \exp(-c [[\mathbf{u} \cdot \bar{\mathbf{n}}]]) \quad (2.3.12)$$

$$\bar{t}_m([[\mathbf{u} \cdot \bar{\mathbf{m}}]]) = t_m \exp(-c [[\mathbf{u} \cdot \bar{\mathbf{m}}]]),$$

whereby c affects the gradient of the curve. The normal and tangential components \bar{t}_n and \bar{t}_m are considered separately, whereby $\bar{\mathbf{t}} = \bar{t}_n \bar{\mathbf{n}} + \bar{t}_m \bar{\mathbf{m}}$.

2.3.4. Hybrid dG/interface approach

Based on the approaches introduced in the last two subsections, we are now able to formulate the hybrid method. The basic idea of the hybrid method is, to combine the discontinuous Galerkin method with the interface approach in a way, that the discontinuous Galerkin method assures the weak enforcement of the continuity of the solution along Γ in the prefailure regime and that the interface approach controls the jump in the displacements in the postcritical state. Therefore we combine the weak formulations (2.3.10) and (2.3.11) with a switching factor α and obtain the weak formulation of the hybrid method

$$\begin{aligned} & \int_{\mathcal{B}^+ \cup \mathcal{B}^-} \delta \epsilon : \boldsymbol{\sigma}(\mathbf{u}) dV + \int_{\Gamma} [1 - \alpha] \left[[[\delta \mathbf{u}]] \cdot \{ \boldsymbol{\sigma}(\mathbf{u}) \} \cdot \bar{\mathbf{n}} + \bar{\mathbf{n}} \cdot \{ \boldsymbol{\sigma}(\delta \mathbf{u}) \} \cdot [[\mathbf{u}]]] dA \\ & + \int_{\Gamma} [[\delta \mathbf{u}]] \cdot \left[[1 - \alpha] \theta [[\mathbf{u}]] + \alpha \bar{\mathbf{t}}([[\mathbf{u}]]) \right] dA = \int_{\mathcal{B}^+ \cup \mathcal{B}^-} \delta \mathbf{u} \cdot \mathbf{b} dV + \int_{\partial \mathcal{B}_t} \delta \mathbf{u} \cdot \mathbf{t}^p dA. \end{aligned} \quad (2.3.13)$$

Thereby the factor α controls the switch from the discontinuous Galerkin method to the interface approach. We set $\alpha = 0$ in the precritical state and once a certain failure criterion is met, $\alpha = 1$ and remains constant thereafter.

2.4. Discretization and linearization

The weak formulation is solved by means of the finite element method. For literature on the finite element method we refer to the textbooks of Bathe [12], Hughes [57] and

Zienkiewicz [139], [140]. The spatial discretization of the underlying problem is characterized by the consideration of the internal interface. Since we generally allow for strong discontinuities in the displacement field, which are enforced to vanish in the precritical state by the dG terms, the displacement field has to be double-valued along the interface.

2.4.1. Spatial discretization

The weak form associated with the domains \mathcal{B}^+ and \mathcal{B}^- is discretized with standard isoparametric elements. The geometry \mathbf{x} is expanded elementwise by shape functions N^k

$$\mathcal{B} = \bigcup_e^{n_{el}} \mathcal{B}_e \quad \mathbf{x}|_{\mathcal{B}_e} = \sum_{i=1}^{n_{en}} N^i \mathbf{x}_i \quad (2.4.1)$$

and in terms of the isoparametric concept, the displacement field \mathbf{u} and its variation $\delta\mathbf{u}$ are expanded by the same shape functions

$$\mathbf{u}|_{\mathcal{B}_e} = \sum_{i=1}^{n_{en}} N^i \mathbf{u}_i \quad \delta\mathbf{u}|_{\mathcal{B}_e} = \sum_{i=1}^{n_{en}} N^i \delta\mathbf{u}_i. \quad (2.4.2)$$

Based on the above discretizations the corresponding gradients $\boldsymbol{\epsilon}$ and $\delta\boldsymbol{\epsilon}$ take the format

$$\boldsymbol{\epsilon}|_{\mathcal{B}_e} = \sum_{i=1}^{n_{en}} [\mathbf{u}_i \otimes \nabla N^i]^s \quad \delta\boldsymbol{\epsilon}|_{\mathcal{B}_e} = \sum_{i=1}^{n_{en}} [\delta\mathbf{u}_i \otimes \nabla N^i]^s. \quad (2.4.3)$$

We denote two elements, which border on Γ with \mathcal{B}_e^+ and \mathcal{B}_e^- . $N^i|_{\Gamma_e}$ indicates the set of shape functions N^i evaluated at the relevant element boundary. The discretization of the corresponding jump and average terms reads

$$\begin{aligned} \llbracket \mathbf{u} \rrbracket|_{\Gamma_e} &= \sum_{i=1}^{n_{en}^+} N^i|_{\Gamma_e} \mathbf{u}_i^+ - \sum_{i=1}^{n_{en}^-} N^i|_{\Gamma_e} \mathbf{u}_i^- = \sum_{p=1}^{n_{en}^+ + n_{en}^-} J^p \mathbf{u}_p \\ \{ \mathbf{u} \}|_{\Gamma_e} &= \frac{1}{2} \left[\sum_{i=1}^{n_{en}^+} N^i|_{\Gamma_e} \mathbf{u}_i^+ + \sum_{i=1}^{n_{en}^-} N^i|_{\Gamma_e} \mathbf{u}_i^- \right] = \sum_{p=1}^{n_{en}^+ + n_{en}^-} A^p \mathbf{u}_p. \end{aligned} \quad (2.4.4)$$

It is apparent that the nodes along the interface Γ are doubled. Therefore the values \mathbf{u}_i^+ and \mathbf{u}_i^- belong to different, independent nodes, which are just situated at the same place. The introduced terms J and A comprise the shape functions evaluated at Γ_e of the two elements and either the associated sign to obtain the jump term or the factor 0.5 to get the average value.

2.4.2. Discrete weak form

The weak formulation is discretized by means of the introduced approximations of the primary variable and the test function. In the precritical state, when the failure criterion has not been met, the discontinuous Galerkin method renders a linear system of equations,

which can be solved directly. Since the geometry of the problem changes, once the failure criterion has been met, and due to the nonlinear constitutive law of the interface approach a nonlinear system of equations is generated. It is solved iteratively by a Newton-Raphson scheme. The discretized weak formulation of the hybrid method, namely the discrete version of equation (2.3.13), reads

$$\mathbf{R}_I = \mathbf{R}_I^{int} + \mathbf{R}_I^{dis} - \mathbf{R}_I^{ext}, \quad (2.4.5)$$

whereby \mathbf{R}_I^{int} , \mathbf{R}_I^{dis} and \mathbf{R}_I^{ext} denote the internal forces, the additional internal forces due to Nitsche's method along the interface and the external forces, respectively. They can be expressed by the assembly of their element contributions

$$\begin{aligned} \mathbf{R}_I^{int} &= \mathbf{A}_{e=1}^{n_{el}} \int \nabla N^i \cdot \boldsymbol{\sigma} dV \\ \mathbf{R}_I^{dis} &= \mathbf{A}_{e=1}^{n_{el}} \int_{\Gamma_e} [1 - \alpha_e] \left[J^i \{ \boldsymbol{\sigma}(\mathbf{u}) \} \cdot \bar{\mathbf{n}} + \nabla A^i \cdot \bar{\mathbf{n}} \cdot \mathbf{C} \cdot [\mathbf{u}] \right] dA \\ &\quad + \int_{\Gamma_e} J^i \left[[1 - \alpha_e] \theta [\mathbf{u}] + \alpha_e \bar{\mathbf{t}}([\mathbf{u}]) \right] dA \\ \mathbf{R}_I^{ext} &= \mathbf{A}_{e=1}^{n_{el}} \int_{\mathcal{B}_e^{+,-}} N^i \mathbf{b} dV + \int_{\partial \mathcal{B}_e} N^i \mathbf{t}^p dA. \end{aligned} \quad (2.4.6)$$

Herein the operator $\mathbf{A}_{e=1}^{n_{el}}$ denotes the assembly of all element contributions at the element nodes $i = 1, n_{en}$ to the overall residual at the global node points $I = 1, n_{np}$. The switching factor α_e is calculated elementwise by means of the failure criterion. Therefore parts of the interface can be in the postfailure regime while others are in the prefailure state. But since α_e is defined elementwise, it comprises the constraint, that the interface connection between two adjacent elements can not fail partly but just for the whole element at the same time.

To solve the resulting system of equations by means of the Newton-Raphson scheme a consistent linearization of (2.4.5) is accomplished

$$\mathbf{R}_I^{k+1} = \mathbf{R}_I^k + d\mathbf{R}_I = \mathbf{0} \quad \text{and} \quad d\mathbf{R}_I = \sum_{J=1}^{n_{np}} \mathbf{K}_{IJ} \cdot \mathbf{u}_J, \quad (2.4.7)$$

whereby $d\mathbf{R}_I$ denotes the iterative residual of the iteration $k + 1$, which is derived as the sum over all node points n_{np} . The iteration matrix is given as the derivative of the residual

$$\mathbf{K}_{IJ} = \frac{\partial \mathbf{R}_I}{\partial \mathbf{u}_J} = \mathbf{K}_{IJ}^{int} + \mathbf{K}_{IJ}^{dis} \quad (2.4.8)$$

and can be composed of its element contributions

$$\begin{aligned}
 \mathbf{K}_{IJ}^{int} &= \mathbf{A} \int_{e=1}^{n_{el}} \nabla N^i \cdot \mathbf{C} \cdot \nabla N^j dV \\
 \mathbf{K}_{IJ}^{dis} &= \mathbf{A} \int_{e=1}^{n_{el}} [1 - \alpha_e] \left[J^i \mathbf{C} \cdot \bar{\mathbf{n}} \cdot \nabla A^j + \nabla A^i \cdot \bar{\mathbf{n}} \cdot \mathbf{C} J^j \right] dA \\
 &\quad + \int_{\Gamma_e} J^i \left[[1 - \alpha_e] \theta J^j + \alpha_e \mathbf{T} J^j \right] dA.
 \end{aligned} \tag{2.4.9}$$

Thereby \mathbf{T} represents the tangent stiffness of the traction separation law at the discontinuity, which is calculated as the derivative of the traction vector (2.3.12) with respect to the jump term as

$$\mathbf{T} = \frac{\partial \bar{\mathbf{t}}}{\partial [\mathbf{u}]} = -t_n c \exp(-c [\mathbf{u} \cdot \bar{\mathbf{n}}]) \bar{\mathbf{n}} \otimes \bar{\mathbf{n}} - t_m c \exp(-c [\mathbf{u} \cdot \bar{\mathbf{m}}]) \bar{\mathbf{m}} \otimes \bar{\mathbf{m}}. \tag{2.4.10}$$

It is obvious that the tangent stiffness matrix is symmetric as long as the tangent stiffness of the traction \mathbf{T} retains its symmetry, which is the case for the chosen traction separation law.

2.4.3. Penalty parameter

The application of Nitsche's method in the precritical regime requires the definition of the penalty parameter θ . As already stated before the penalty parameter has to be sufficiently large so that the method is stable, in that it can guarantee that the resulting stiffness matrix is positive definite. It can be shown, that for linear elasticity the penalty parameter depends on the element size and the material parameters, see for example [50], [54] and [41]. Therefore we introduce the penalty parameter as

$$\theta = \frac{\vartheta}{h} [\lambda + \mu]. \tag{2.4.11}$$

Now the scalar factor ϑ does not depend on the material parameters or the element size. In appendix B a numerical study of the influence of the penalty parameter on the solution is accomplished. Thereby the dG method is applied along all interelement boundaries.

Analytical derivations of the sufficient size of the penalty parameter can for example be found in [50] and [41]. In [54] an explicit calculation of the minimum penalty factor is carried out, which is possible if linear elements are used, such that the stresses are elementwise constant.

2.5. Implementation

The decisive factor for the change from the dG method to the interface approach is given by the failure criterion. The switching factor α_e is set from 0 to 1 for a particular interface,

if the traction vector of the discontinuity surface Γ meets the following failure criterion:

$$\{\boldsymbol{\sigma}\} : [\bar{\mathbf{n}} \otimes \bar{\mathbf{n}}] + \beta |\{\boldsymbol{\sigma}\} : [\bar{\mathbf{n}} \otimes \bar{\mathbf{m}}]| - t^{crit} \leq 0 \quad \rightarrow \quad \alpha = 0, \quad (2.5.1)$$

whereby β assigns different weights to the normal tractions and the absolute value of the tangential components of the traction. To ensure a continuous transition from the discontinuous Galerkin method to the interface approach, the values, which are reached for $\{\boldsymbol{\sigma}(\mathbf{u})\} : [\bar{\mathbf{n}} \otimes \bar{\mathbf{n}}]$ and $\{\boldsymbol{\sigma}(\mathbf{u})\} : [\bar{\mathbf{n}} \otimes \bar{\mathbf{m}}]$ in the moment of failure provide the normal and tangential components of the traction vector $\bar{\mathbf{t}}$ for $[[\mathbf{u}]] = \mathbf{0}$, namely t_n and t_m .

The method is implemented using bilinear quadrilateral elements. Both the dG method

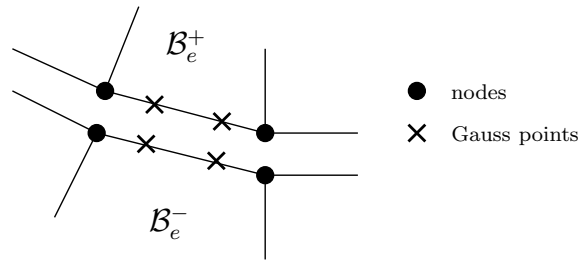


Figure 2.2.: Integration of the boundary contributions

| |
|--|
| loop over load steps |
| global Newton iteration |
| loop over all elements |
| determine element residua \mathbf{R}_e^{int} and their derivatives \mathbf{K}_e^{int} |
| loop over all element boundaries $\Gamma_e = \partial\mathcal{B}_e \cup \Gamma$ which belong to the interface |
| determine interface residua \mathbf{R}_e^{dis} and their derivatives \mathbf{K}_e^{dis} |
| assemble global residual \mathbf{R} and tangent stiffness matrix \mathbf{K} |
| calculate $\boldsymbol{\sigma}$ and the interfacial tractions $\{\boldsymbol{\sigma}\} \cdot \bar{\mathbf{n}}$ |
| check failure criterion |
| determine state of equilibrium |

Table 2.1.: Algorithmic implementation of the hybrid approach

and the interface approach include additional interfacial contributions. To evaluate these terms numerically two further Gauss points are introduced at each element boundary, which belongs to Γ , compare figure 2.2.

Since the algorithmic implementation requires the nonstandard integration over certain element boundaries, the basic procedure of the approach is highlighted in table 2.1.

2.6. Numerical examples

In the following two numerical examples are presented, which demonstrate the performance of the introduced hybrid method. Firstly a mode I problem is considered, to check the transition from the discontinuous Galerkin method to the interface approach. In the second example mixed mode failure is simulated.

2.6.1. Mode I failure

In this example the hybrid approach is applied to a purely mode I problem, to study the influence of different discretizations and to check the transition from the discontinuous Galerkin method to the interface approach. The geometry and the loading conditions of the model problem are pictured in figure 2.3a, the potential failure zone is introduced in the middle of the bar and the bar is loaded on both sides by displacement control. It is shown in figure 2.3b that the load displacement curve is independent of the discretization and that the transition from the discontinuous Galerkin method to the interface approach is smooth. Furthermore the effect of the choice of the factor c on the softening behavior is shown. The larger the coefficient c , the more brittle is the material response. Figure 2.3c displays the deformation of the structure at the different time steps A-D, as indicated in figure 2.3b. Since there is a constant stress state in the structure the interface fails completely once the tensile strength is reached. Then the cohesive tractions resist the opening of the interface.

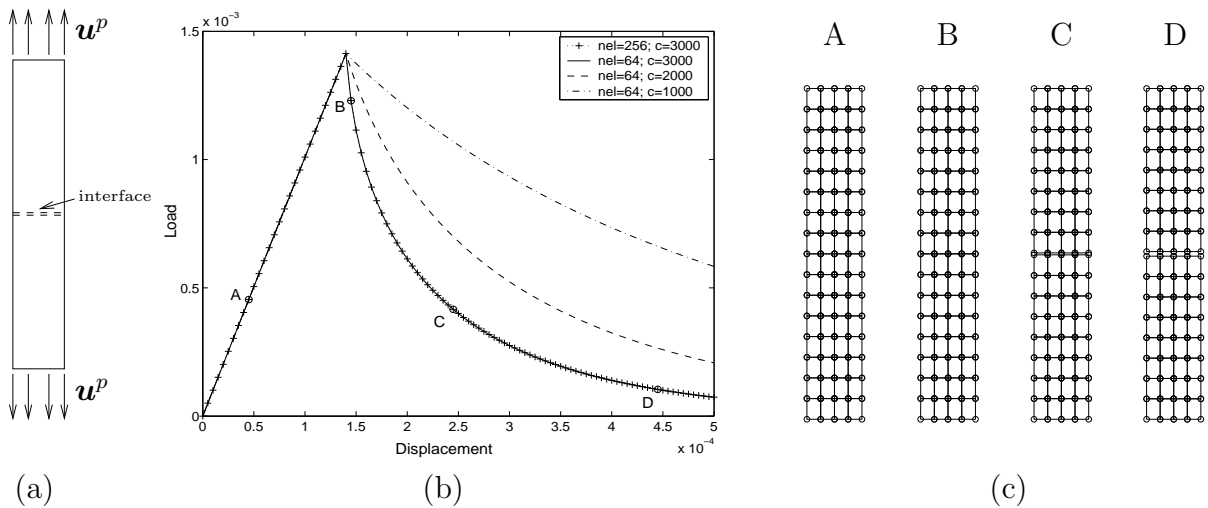


Figure 2.3.: Mode I - geometry, load displacement relation and deformation of the structure

2.6.2. Mixed mode failure

The second example is concerned with mixed mode failure. Figure 2.4 depicts the geometry of the structure, the loading conditions and the resulting load displacement

relation. The load displacement curve is not as smooth as in the first example, since the failure criterion is not met at the same time for all element boundaries Γ_e , but successively. The deformation of the structure and the relaxation of the two continuous parts are shown in figure 2.4 as well as the lateral sliding as a consequence of the development of the discontinuity in the displacement field. In this example an additional penalty term, which enforces that $[[\mathbf{u} \cdot \bar{\mathbf{n}}]] \geq 0$, is added to the weak formulation of the hybrid form (2.3.13), to prevent the penetration of the two parts of the structure after the failure of the interface.

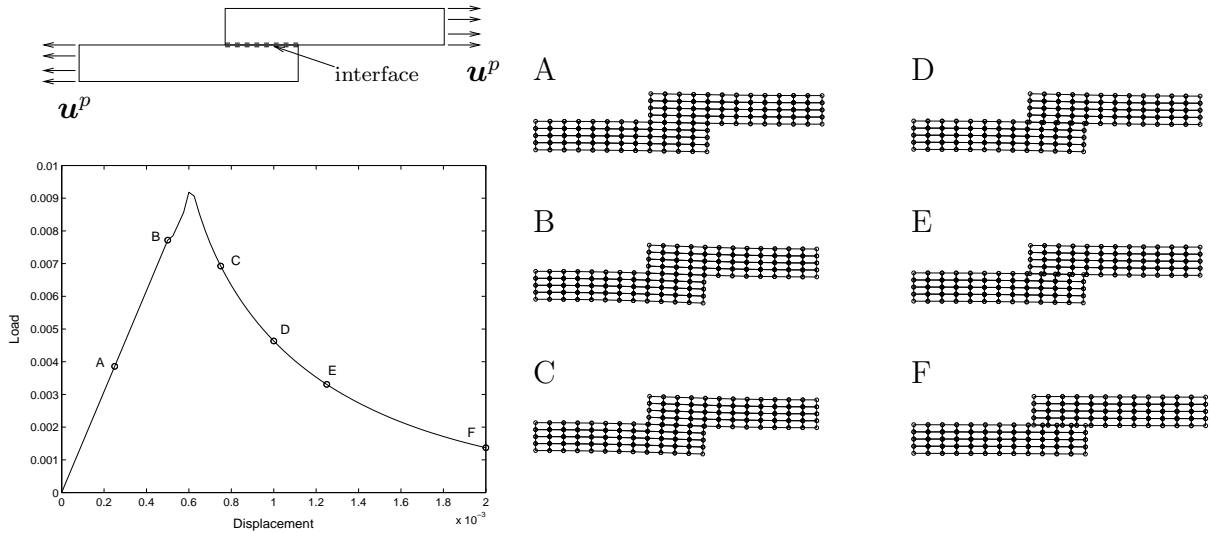


Figure 2.4.: Mixed mode - geometry, load displacement relation and deformation of the structure

2.7. Summary

A consistent hybrid formulation for the computational modeling of failure along a known interface has been proposed. Prior to failure the discontinuous Galerkin method is applied to enforce the continuity of the solution weakly and to refrain from the use of unphysical penalty parameters. As soon as the failure criterion is met, a switch from the discontinuous Galerkin method to the interface approach takes place. The material behavior in the postcritical regime is described by a constitutive traction separation law, which is chosen independently of the constitutive setting of the surrounding domain. By means of two numerical examples concerning mode I and mixed mode failure the applicability of the hybrid method was shown. It was shown that the global load displacement answer is independent of the discretization. The transition from the prefailure to the postfailure regime was checked as well as the resulting deformation and the expected results were achieved.

3. Mesh-independent modeling of strong discontinuities

This chapter is concerned with the computational modeling of cohesive cracks. In contrast to the previous chapter, the discontinuity is not limited to interelement boundaries, but is allowed to propagate freely through the elements. Therefore the approach is not limited to failure processes with known failure zones. In the elements, which are intersected by the discontinuity, additional displacement degrees of freedom are introduced at the existing nodes. The formulation of these discontinuous elements allows for the simulation of crack propagation without remeshing. Details on the numerical implementation are given, concerning the failure criterion, the determination of the direction of the discontinuity and the integration scheme. Finally numerical examples show the performance of the method. The formulation is restricted to geometrically linear problems.

3.1. Motivation

In the present chapter a method for the modeling of cohesive cracks is described, which was introduced in reference [81]. The discontinuity is supposed to propagate independently of the mesh structure. Therefore elements with an internal discontinuity are formulated. The construction of these elements follows the approach, recently proposed by Hansbo and Hansbo in [46] and [47]. To model inelastic material behavior, a discrete damage type model is applied, formulated in terms of displacements and tractions at the discontinuity surface. This procedure is similar to the one in the previous chapter beside the fact that the interface is situated within certain elements and not along element boundaries. The discontinuities are introduced when a failure criterion is met, such that the discrete constitutive model characterizes the inelastic behavior only and the continuum represents the elastic response. Since the discontinuity is not introduced until failure occurs the continuity of the solution is directly satisfied in the prefailure regime. In contrast to the approach in chapter 2 no additional effort has to be made to ensure continuity prior to failure.

The modeling techniques for the simulation of failure processes can generally be divided into continuous and discrete methods, compare [20]. Within the continuous approach the the body is considered as a continuum and the displacement field is continuous throughout the body. The failure process is described by means of continuum damage formulations, which connects continuum stresses with continuum strains. The observation of discrete

cracks leads to the development of discrete failure models. Thereby a discrete failure surface is introduced in the body and the formulation allows for the development of strong discontinuities, namely jumps in the displacement field. To describe the inelastic failure process a discrete traction separation relation is introduced at the failure surface. Thereby the tractions are constitutively prescribed, controlled by the jump in the displacement field, and prevent the opening of the discontinuity. It is assumed that the crack surfaces are able to transmit these tractions. With an increasing opening of the crack surfaces the tractions eventually vanish. The so-called cohesive traction separation law can be chosen independently of the surrounding material response. Different inelastic processes prior to failure can be summarized in a phenomenological cohesive law. The cohesive zone models trace back to the work of Dugdale and Barenblatt. Dugdale introduced in [34] a cohesive zone model for ductile materials, whereby Barenblatt's model [10] is suited for cracks in brittle materials. During the last years cohesive zone models were frequently used in the finite element simulation of failure processes and crack propagation, an overview is given in section 3.4.2.

The numerical implementation of the cohesive zone models requires special finite elements, which comprise the traction separation law. In some approaches interface elements are utilized, as in the approach in the previous chapter. An interface element has zero width and is placed between the continuum elements along a predefined discontinuity surface. The interface elements behave like a nonlinear (softening) spring when the structure is loaded. It is obvious that the formulation with interface elements implies one constraint. The failure geometry has to be known in advance, either due to the structure of the material (delamination in composites) or due to experimental evidence. To overcome this problem Xu and Needleman [137] introduced a formulation with interface elements between all continuum elements. And Camacho and Ortiz [23] introduced an adaptive method to simulate brittle fracture. Nevertheless the direction of the crack is not entirely free, or a permanent remeshing of the structure has to be accomplished.

Due to these drawbacks different numerical approaches have been considered over the last years, which allow for the modeling of strong discontinuities which can run arbitrarily through finite elements. Mainly two formulations can be distinguished: elements with embedded discontinuities and the extended finite element method, based on the partition of unity method, [9].

In the approach with embedded discontinuities strain or displacement discontinuities are inserted by means of additional degrees of freedom on the element level. This permits the discontinuity to have arbitrary orientation, but the discontinuity is incompatible over element boundaries. The additional degrees of freedom can be eliminated at the element level. The class of methods seems to go back to the work of Ortiz et al. [100] and Belytschko et al. [16], where a discontinuity in the strain field was used for the modeling of localization. Formulations which contain jumps in the displacement field were intro-

duced by Klisinski et al. in [64] and Lofti et al. in [75]. The variational framework for the consideration of enhanced strain or displacement fields was established by Simo and co-workers in [115], [112] and [113]. Simo, Oliver and Armero analyzed in [114] the connection between the continuous stress strain dependency and the discrete traction separation relation and presented a one dimensional finite element for the simulation of strong discontinuities. Further extensions and application of the method can be found for different problems and by different authors. In [96] Oliver provides a summary of the theoretical and numerical aspects of the method. Jirasek applied the embedded discontinuity elements for the modeling of damage and crack closure effects in [61] and [62]. In the thesis of Wells [128] an extension to three dimensions can be found and Mosler et al. studied the method using a rotating crack concept [90]. An extension of the concept to beams was recently proposed in [35]. An overview and a classification of the different approaches is given in [60], whereby it is distinguished between the statically optimal symmetric approach, the kinematically optimal symmetric approach and the statically and kinematically optimal nonsymmetric approach.

The extended finite element method, which is conceptually most similar to the present one, traces back to Belytschko et al., see references [14] and [87], where it was applied to linear elastic fracture problems. The method is based on the partition of unity concept, compare [79]. The essential idea of the method is to add enrichment functions to the approximation, which contain a discontinuous displacement field. Since the additional degrees of freedom, which are required to represent the enrichment functions, are global, the discontinuity is continuous over element boundaries but the additional degrees of freedom can not be condensed out at the element level. A detailed description of the XFEM can be found in [31]. The method was extended by Sukumar et al. to handle three dimensional cracks [125] and by Daux et al. to include intersecting and branching cracks [27]. Wells and Sluys [130], Moës and Belytschko [85] and Zi and Belytschko [138] applied the partition of unity method to the modeling of cohesive cracks. In [30], [17] and [123] the XFEM was used to model crack growth with friction, arbitrary discontinuities and crack growth by means of level sets. In [132] and [116] the XFEM was used within a strain softening material. The modeling of fracture in Mindlin-Reissner plates was considered in [29], in [15] dynamic crack growth was analyzed and recently the XFEM was extended to the modeling of crack propagation in shells [3]. An overview over the different possibilities of the XFEM can be found in [63].

Another approach with additional global degrees of freedom was introduced by Bolzon and Corigliano in [18] and extended by Löblein in [74].

The present approach allows also for arbitrary discontinuities within the elements. The special characteristic of the present approach lies in the formulation of the elements with an internal discontinuities, which is based on the idea of Hansbo and Hansbo, [46] and [47]. In contrast to the present method, in [46] and [47] the discontinuous elements were applied

in an extended Nitsche's method [95]. That allows for the simulation of weak as well as strong discontinuities within the elements, but the formulation was restricted to linear traction separation laws.

The displacement field of an intersected element is a discontinuous function, which exhibits a jump along the discontinuity, but is continuous on both sides of this discontinuity. Therefore the displacement field can as well be considered as two independent continuous functions, with the displacement jump being the difference of the two function values at both sides of the discontinuity. Additional displacement degrees of freedom are introduced at the existing nodes and two independent copies of the standard basis functions are used, to permit the approximation of the two continuous functions. One set of basis functions is put to zero on one side of the discontinuity while it takes its usual values on the other side and vice versa. This allows for the formulation of elements with internal discontinuities, using only displacement degrees of freedom and the standard basis functions. In contrast to the extended finite element method the enrichment is strictly local and no additional transition elements are required.

In the next chapter the kinematic relations for a domain crossed by a discontinuity are described. Afterwards the governing equations are given and the variational formulation of the problem is derived. The constitutive equations are specified in section 3.4, whereby the cohesive crack concept is described in detail. The following section deals with the discretization of the variational formulation and especially with the construction of the discontinuous element. Furthermore the linearized discrete weak form is specified. Then some details about the implementation are given and finally the performance of the method is pointed out by means of numerical examples.

3.2. Kinematics

To develop a numerical method for solving problems that include displacement discontinuities we need to define the kinematics that describe a displacement jump across a surface. To introduce the notation we shortly review the kinematics of a continuous body in a geometrically linear setting and specify the strong discontinuity kinematics afterwards.

3.2.1. Continuous kinematics

We consider a body \mathcal{B} with the boundary $\partial\mathcal{B}$ and with placements denoted by \mathbf{x} . The boundary $\partial\mathcal{B}$ with the external normal vector \mathbf{n}_e is subdivided into the disjoint parts $\partial\mathcal{B} = \partial\mathcal{B}_u \cup \partial\mathcal{B}_t$ with $\partial\mathcal{B}_t \cap \partial\mathcal{B}_u = \emptyset$, where either Neumann or Dirichlet boundary conditions are prescribed. The unknown continuous displacement field is denoted by \mathbf{u} . The symmetric strain tensor is specified as the symmetric part of the gradient of the

displacement field with respect to \boldsymbol{x}

$$\boldsymbol{\epsilon} = \frac{1}{2}[\nabla \boldsymbol{x} \boldsymbol{u} + \nabla^t \boldsymbol{x} \boldsymbol{u}] = \nabla^s \boldsymbol{x} \boldsymbol{u}, \quad (3.2.1)$$

whereby the superscript s denotes the symmetric part of the differential operator.

3.2.2. Strong discontinuity kinematics

Now we consider a body \mathcal{B} which is divided by a discontinuity surface Γ into the parts \mathcal{B}^+ and \mathcal{B}^- . Consequently the position vectors of the points in \mathcal{B}^+ and \mathcal{B}^- are denoted with \boldsymbol{x}^+ and \boldsymbol{x}^- . The displacement field \boldsymbol{u} is continuous in both parts of the body, but discontinuous along the discontinuity surface. Therefore we can write the displacement field as

$$\boldsymbol{u}(\boldsymbol{x}) = \begin{cases} \boldsymbol{u}^+(\boldsymbol{x}) & \text{in } \mathcal{B}^+ \\ \boldsymbol{u}^-(\boldsymbol{x}) & \text{in } \mathcal{B}^- \end{cases} \quad (3.2.2)$$

The jump in the displacement field is calculated as the difference of the two continuous functions, evaluated on Γ

$$\llbracket \boldsymbol{u} \rrbracket = \boldsymbol{u}_{|\Gamma}^+ - \boldsymbol{u}_{|\Gamma}^-, \quad (3.2.3)$$

whereby $\boldsymbol{u}_{|\Gamma}^{\pm}$ denote the boundary values of \boldsymbol{u}^{\pm} . The unit normal vector $\bar{\boldsymbol{n}}$ associated

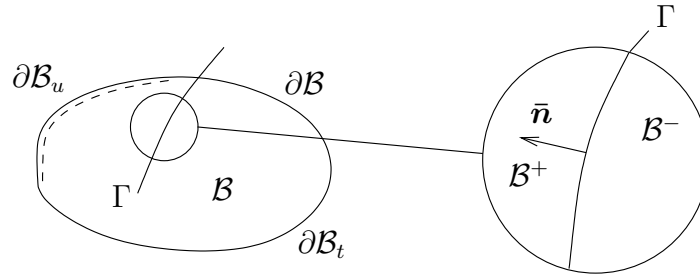


Figure 3.1.: \mathcal{B} crossed by a discontinuity Γ

with Γ points from \mathcal{B}^- to \mathcal{B}^+ , see figure 3.1. Therefore the jump can be separated into a normal and tangential part with respect to Γ

$$\llbracket \boldsymbol{u}_n \rrbracket = \llbracket u_n \rrbracket \bar{\boldsymbol{n}} \quad \text{with} \quad \llbracket u_n \rrbracket = \llbracket \boldsymbol{u} \rrbracket \cdot \bar{\boldsymbol{n}} \quad (3.2.4)$$

$$\llbracket \boldsymbol{u}_m \rrbracket = \llbracket \boldsymbol{u} \rrbracket - \llbracket \boldsymbol{u}_n \rrbracket.$$

The strain tensor in the bulk is found by taking the derivative of the displacement field. Since the displacement field is defined by two independent continuous functions, the strain tensor is as well defined separately for both parts of the body

$$\boldsymbol{\epsilon}(\boldsymbol{x}) = \begin{cases} \boldsymbol{\epsilon}^+(\boldsymbol{x}) = \nabla^s \boldsymbol{u}^+(\boldsymbol{x}) & \text{in } \mathcal{B}^+ \\ \boldsymbol{\epsilon}^-(\boldsymbol{x}) = \nabla^s \boldsymbol{u}^-(\boldsymbol{x}) & \text{in } \mathcal{B}^- \end{cases} \quad (3.2.5)$$

Note that the strain tensor is not defined along Γ .

3.3. Variational formulation

In this chapter the variational formulation of the relevant field equations is derived. The variational principle belongs to the fundamental principles in mathematics and mechanics, and the variational approach can be considered as the basis for the development of most of the discretization methods, e. g. the finite element method. The weak formulation will be derived from the principle of stationary potential energy.

3.3.1. Principle of stationary potential energy

To utilize the principle of stationary potential energy we require the existence of a functional Π . The total potential energy is usually given as the sum of the internal and external potential energy. If we consider strong discontinuities by means of the cohesive crack concept, we have to take into account an additional cohesive energy contribution along the interface. This cohesive energy distribution defines the energy which is dissipated when crack propagation takes place. The cohesive energy can be seen as a material parameter, which is taken into account by the cohesive constitutive law. To obtain the variational formulation of the problem, we start with the definition of the total potential energy

$$\Pi(\mathbf{u}) = \Pi^{int} + \Pi^{coh} + \Pi^{ext}. \quad (3.3.1)$$

To simplify matters we assume that no body forces are acting and therefore the external energy depends solely on the Neumann tractions. Then the above equation can be specified as

$$\Pi(\mathbf{u}) = \int_{\mathcal{B}^+ \cup \mathcal{B}^-} \Psi(\boldsymbol{\epsilon}(\mathbf{u})) dV + \int_{\Gamma} \bar{\Psi}([\![\mathbf{u}]\!]]) dA - \int_{\mathcal{B}_t} \mathbf{u} \cdot \mathbf{t}^p dA. \quad (3.3.2)$$

Thereby $\Psi(\boldsymbol{\epsilon})$ denotes the strain energy function per unit volume and is specified for linear elastic material behavior in section 3.4.1. The internal energy describes the energy which is stored in the body due to an elastic deformation. In analogy to the usual internal energy distribution, the cohesive energy is constituted by the cohesive energy density $\bar{\Psi}([\![\mathbf{u}]\!]])$, which is given for certain cohesive constitutive laws in section 3.4.2. The last term of the equation represents the external energy, \mathbf{t}^p are the prescribed tractions at the Neumann boundary $\partial\mathcal{B}_t$.

The stationary position of the total potential energy is obtained by requiring its variation with respect to the displacement field \mathbf{u} to vanish. This leads to the following variational formulation

$$\delta\Pi(\mathbf{u}, \delta\mathbf{u}) = \int_{\mathcal{B}^+ \cup \mathcal{B}^-} \delta\boldsymbol{\epsilon} : \boldsymbol{\sigma} dV + \int_{\Gamma} [\![\delta\mathbf{u}]\!] \cdot \bar{\mathbf{t}} dA - \int_{\mathcal{B}_t} \delta\mathbf{u} \cdot \mathbf{t}^p dA \doteq 0, \quad (3.3.3)$$

whereby $\boldsymbol{\sigma}$ is the Cauchy stress, which is derived from the strain energy function by $\boldsymbol{\sigma} := \partial\Psi(\boldsymbol{\epsilon})/\partial\boldsymbol{\epsilon}$. Analogously the cohesive traction vector $\bar{\boldsymbol{t}}$ is defined as the derivative of the cohesive energy density with respect to the jump term $\bar{\boldsymbol{t}} := \partial\bar{\Psi}([\boldsymbol{u}])/\partial[\boldsymbol{u}]$. Both terms have to be specified for a particular energy density. Equation (3.3.3) constitutes the variational formulation of the considered problem.

3.3.2. Governing equations

Since the stationary condition of the potential energy yields the principle of virtual work for a configuration in static equilibrium [56], we can specify the underlying strong form of the boundary value problem. The Euler equation is given by Cauchy's first equation of motion

$$-\operatorname{div}\boldsymbol{\sigma} = \mathbf{0} \quad \text{in} \quad \mathcal{B}^+ \cup \mathcal{B}^-. \quad (3.3.4)$$

The boundary conditions define the displacements at the Dirichlet boundary and the tractions at the Neumann boundary.

$$\boldsymbol{\sigma} \cdot \boldsymbol{n}_e = \boldsymbol{t}^p \quad \text{on} \quad \partial\mathcal{B}_t \quad \text{and} \quad \boldsymbol{u} = \boldsymbol{u}^p \quad \text{on} \quad \partial\mathcal{B}_u \quad (3.3.5)$$

The interfacial contribution in the potential energy leads to an additional traction equilibrium condition at the internal boundary.

$$\boldsymbol{\sigma}^+ \cdot \bar{\boldsymbol{n}} = \boldsymbol{\sigma}^- \cdot \bar{\boldsymbol{n}} = \bar{\boldsymbol{t}} \quad \text{on} \quad \Gamma. \quad (3.3.6)$$

Thereby the traction vector $\bar{\boldsymbol{t}}$ is constitutively prescribed by the cohesive traction separation law.

3.4. Constitutive equations

In the following section the constitutive laws, which determine the material response, are specified. In general the constitutive equation defines the stress state at any point \boldsymbol{x} , depending on other field variables, e. g. the strain.

In the present approach we consider strong discontinuities by means of the cohesive crack concept. Therefore we need to introduce two constitutive equations, one for the material behavior of the bulk, defined by the strain energy density Ψ , and one for the cohesive tractions at the internal boundary, specified by the cohesive energy density $\bar{\Psi}$.

3.4.1. Continuous constitutive law

The material behavior of the bulk is assumed to be linear elastic. The linear dependence of the stress $\boldsymbol{\sigma}$ on the strain $\boldsymbol{\epsilon}$ can be expressed by means of the so called elasticity tensor \mathbf{C} . The associated strain energy function is given as

$$\Psi(\boldsymbol{\epsilon}) = \frac{1}{2} \boldsymbol{\epsilon} : \mathbf{C} : \boldsymbol{\epsilon} \quad (3.4.1)$$

and the stress strain relation follows as

$$\boldsymbol{\sigma} = \frac{\partial \Psi(\boldsymbol{\epsilon})}{\partial \boldsymbol{\epsilon}} = \mathbf{C} : \boldsymbol{\epsilon}. \quad (3.4.2)$$

Since we consider only isotropic material behavior the elasticity tensor \mathbf{C} depends on two material parameters, for example the Young's modulus E and the Poisson's ratio ν .

3.4.2. Cohesive crack concept

The concept of cohesive zone models goes back to the pioneering work of Dugdale [34] and Barrenblatt [10]. Cohesive zone models are extensively used in computational mechanics to simulate fracture and failure processes. In the framework of cohesive zone models the crack tip is not considered to be infinitely sharp, as in linear elastic fracture mechanics, but the existence of a fracture process zone in front of the crack tip is assumed. In this process zone small-scale yielding, micro-cracking, void initiation and other inelastic processes take place. Following the cohesive crack concept, these degrading mechanisms are lumped into a discrete line or plane. Cohesive tractions, which prevent the separation between the incipient material surfaces, are transmitted along this plane, see figure 3.2. These cohesive tractions are constitutively prescribed by a traction separation law, depending on the opening displacement. Under monotonic loading the tractions eventually reduce to zero when a critical opening is attained. Within the constitutive traction separation law the different dissipative processes are combined into a phenomenological approach. Therefore the fracture process is seen as a gradual phenomenon.

Since the implementation of cohesive zone models in the context of finite element methods is relatively easy, they evolved as a preferred method to analyze fracture problems. Different traction separation laws, linear, bilinear or exponential, have been introduced to simulate ductile or brittle fracture, see e. g. [55], [91], [99], [92], [127], [23], [72]. Irreversible cohesive laws were for example introduced in [23], [101] and in [94] for fatigue crack growth. An irreversible uncoupled cohesive model for delamination analysis was proposed in [1], whereby the tangential and normal tractions are derived by independent constitutive relations. Cohesive zone models under dynamic conditions were used in [137] and [23] and critically surveyed with respect to crack branching in [39].

There is a common belief that cohesive zone laws can be described by two independent parameters [93], which may be the tensile strength f_t and the work of separation G_f , which is the work that is needed to create a unit surface of a fully developed (traction-free) crack. In the case of brittle material the shape of the traction separation relation is quite important [21]. Two stylized traction separation relations for the one dimensional case are plotted in figure 3.3, describing more ductile and more brittle failure, respectively.

There are different numerical approaches, to include the cohesive law in finite element analyses, as introduced in section 3.1. The most important difference between them,

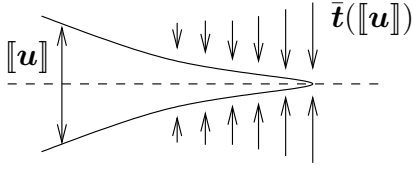


Figure 3.2.: Tractions transmitted in the cohesive zone

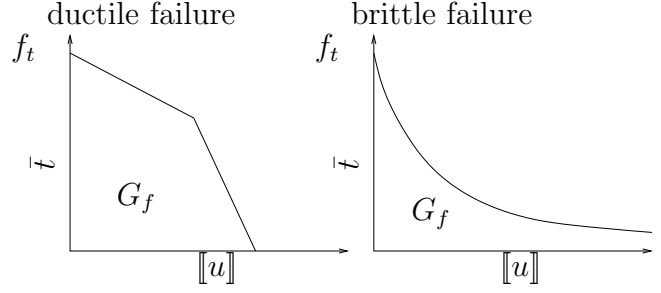


Figure 3.3.: Traction separation relations

concerning the formulation of the cohesive law, is, if the cohesive zones or elements are introduced a priori or adaptively depending on a failure criterion. If the crack path is known in advance, either from experimental evidence or due to the material structure (delamination), cohesive or interface elements can be introduced along the potential crack path. The applied cohesive laws have the characteristic that with an increasing interfacial separation the tractions across the interface reach a maximum, then decrease and eventually vanish, permitting a complete decohesion. Therefore the cohesive elements model an initially elastic behavior and an opening of the adjacent surfaces is possible when the critical load is not reached. Conversely Camacho and Ortiz [23] and Pandolfi et al. [103] introduced an initially rigid cohesive law, whereby the displacement jump is fixed at zero until a critical stress is reached. Initially rigid cohesive laws are naturally connected with adaptivity, since the cohesive zone is adaptively activated, depending on a failure criterion, see e. g. [104]. This kind of cohesive laws is well suited for the introduction within discontinuous elements, see for example [130], [81] or [43].

The cohesive constitutive law, which is formulated here, is valid for quasi-brittle materials. The material behavior in the direction normal to the discontinuity surface shall be different from that one in tangential direction, to distinguish between sliding and separation. To specify the traction separation law we start with the definition of the cohesive potential energy $\bar{\Psi}$, which depends only on the normal and tangential jump in the displacement field

$$\bar{\Psi} = \bar{\Psi}(\llbracket \mathbf{u} \rrbracket) = \bar{\Psi}(\llbracket u_n \rrbracket, \llbracket \mathbf{u}_m \rrbracket). \quad (3.4.3)$$

In normal direction exponential softening is assumed and in tangential direction a constant shear stiffness is adopted. The cohesive potential is specified as

$$\bar{\Psi}(\llbracket u_n \rrbracket, \llbracket \mathbf{u}_m \rrbracket) = G_f [1 - \exp(-\frac{f_t}{G_f} \llbracket u_n \rrbracket)] + \frac{1}{2} d \llbracket \mathbf{u}_m \rrbracket \cdot \llbracket \mathbf{u}_m \rrbracket, \quad (3.4.4)$$

thereby the material parameters are the fracture energy G_f , the tensile strength f_t and the shear stiffness d . The derivative of the cohesive potential with respect to the jump leads to the definition of the cohesive traction vector

$$\bar{\mathbf{t}} = \frac{\partial \bar{\Psi}}{\partial \llbracket \mathbf{u} \rrbracket} = f_t \exp(-\frac{f_t}{G_f} \llbracket u_n \rrbracket) \bar{\mathbf{n}} + d \llbracket \mathbf{u}_m \rrbracket. \quad (3.4.5)$$

This discrete constitutive formulation is chosen due to its simplicity with respect to the implementation, the introduction of more general constitutive law is straightforward. Since the chosen cohesive traction separation law is nonlinear its linearization will be needed, which is derived as the derivative of $\bar{\mathbf{t}}$ with respect to $[[\mathbf{u}]]$

$$\mathbf{T} = \frac{\partial \bar{\mathbf{t}}}{\partial [[\mathbf{u}]]} = -\frac{f_t^2}{G_f} \exp\left(-\frac{f_t}{G_f} [[u_n]]\right) \mathbf{n} \otimes \mathbf{n} + d[\mathbf{I} - \bar{\mathbf{n}} \otimes \bar{\mathbf{n}}]. \quad (3.4.6)$$

Due to the constant shear stiffness, which does not depend on the normal part of the jump, the stiffness matrix retains its symmetry.

3.5. Discretization and linearization

The variational formulation which was derived in section 3.3.1 is discretized by means of the finite element method. Discontinuous elements are constructed to allow for strong discontinuities, which are independent of the mesh structure. The resulting nonlinear discrete weak form is consistently linearized to be solved by a Newton-Raphson scheme.

3.5.1. Formulation of a discontinuous element

To construct an element \mathcal{B}_d with an internal discontinuity we consider that \mathcal{B}_d is divided by Γ_d into $\mathcal{B}_d^+ := \mathcal{B}^+ \cap \mathcal{B}_d$ and $\mathcal{B}_d^- := \mathcal{B}^- \cap \mathcal{B}_d$. The displacement field \mathbf{u} is continuous for both parts of the element, but exhibits a discontinuity along Γ_d . In analogy to (3.2.2) we can describe the displacement field of the element \mathcal{B}_d by

$$\mathbf{u}(\mathbf{x}) = \begin{cases} \mathbf{u}_d^+(\mathbf{x}) & \text{in } \mathcal{B}_d^+ \\ \mathbf{u}_d^-(\mathbf{x}) & \text{in } \mathcal{B}_d^-. \end{cases} \quad (3.5.1)$$

To approximate one of the continuous displacement fields \mathbf{u}_d^+ or \mathbf{u}_d^- , we need the usual number of degrees of freedom, depending on the desired polynomial degree. Even though \mathbf{u}_d^+ is only defined in \mathcal{B}_d^+ it can as well be approximated by the nodal values at all nodes of the element and the standard basis functions. The same applies to \mathbf{u}_d^- which has, due to the discontinuous characteristic, no relation to \mathbf{u}_d^+ . To ensure the independent approximation of both continuous parts of the displacement field, we need to introduce new degrees of freedom at the existing nodes. Furthermore we apply two copies of the standard basis functions. One set is put to zero on one side of the discontinuity, while it takes its usual values on the other side, and vice versa

$$N^{+i} = \begin{cases} N^i & \text{in } \mathcal{B}_d^+ \\ 0 & \text{in } \mathcal{B}_d^-, \end{cases} \quad \text{and} \quad N^{-i} = \begin{cases} 0 & \text{in } \mathcal{B}_d^+ \\ N^i & \text{in } \mathcal{B}_d^-. \end{cases} \quad (3.5.2)$$

To clarify the procedure of the introduction of additional degrees of freedom, a one dimensional example is considered in figure 3.4. In the left part of the picture the set of

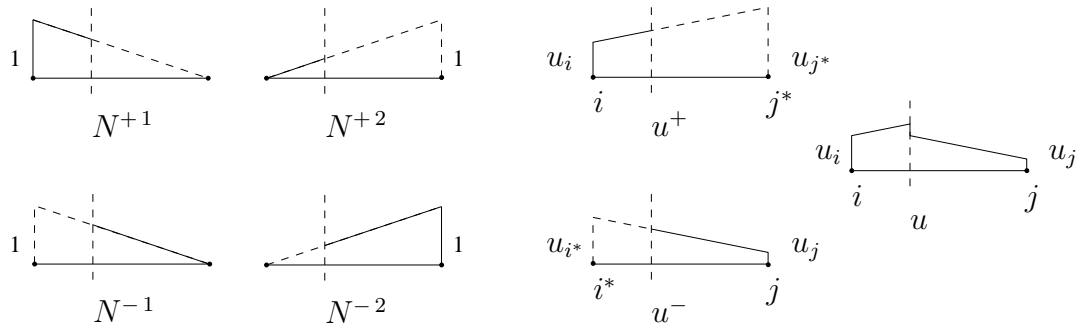


Figure 3.4.: Approximation of the discontinuous displacement field in 1D

one-dimensional basis functions is pictured, whereby the dashed lines indicate the parts which are equal to zero. In the middle of the picture an exemplary approximation of two continuous functions u^+ and u^- is given, which can be obtained by the new set of basis functions and the two additional degrees of freedom at the nodes i^* and j^* as

$$u^+ = N^{+1}u_i + N^{+2}u_{j^*} \quad u^- = N^{-1}u_{i^*} + N^{-2}u_j. \quad (3.5.3)$$

Since the basis functions are equal to zero in the element part where the particular continuous function is not defined, the discontinuous function u is obtained as the sum of u^+ and u^- . In the more general two- or three-dimensional case this approximation is given as

$$\mathbf{u}|_{\mathcal{B}_d} = \sum_{i=1}^{n_{en}^+} N^{+i} \mathbf{u}_i^+ + \sum_{i=1}^{n_{en}^-} N^{-i} \mathbf{u}_i^-. \quad (3.5.4)$$

This set of discontinuous basis functions can be easily constructed for different types of elements of higher order and dimension. Exemplarily the approximation of a discontinuous function is highlighted for two-dimensional linear triangles in figure 3.5, since these elements will mainly be used in the numerical simulations. The additional degrees of free-

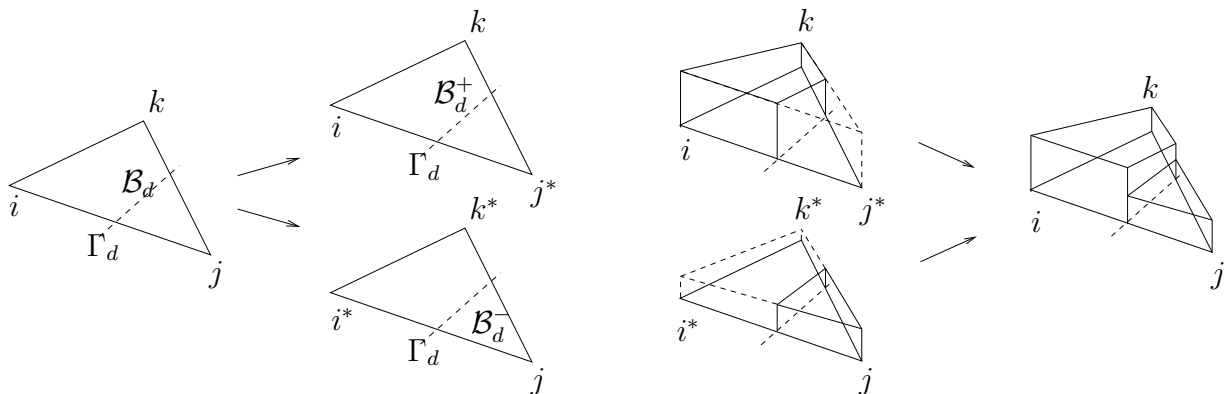


Figure 3.5.: Split of linear triangular element and approximation of the discontinuous displacement field domains are introduced at the existing nodes. Therefore the points of intersection between

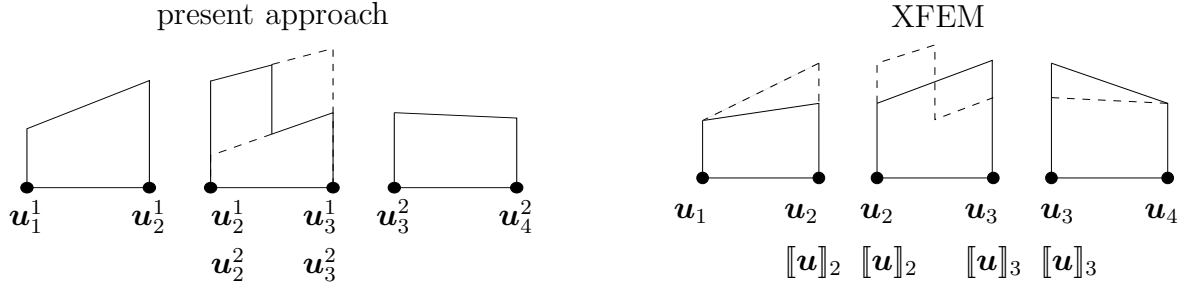


Figure 3.6.: Comparison – present approach, XFEM

the element edges and the discontinuity as well as the geometry of the element parts are not needed until the evaluation of the weak form.

Remark 3.5.1 *The difference between the discretization with the present method and the XFEM is clarified by means of a onedimensional bar which is intersected by a strong discontinuity in figure 3.6. On the left hand side of the figure the discretization with the present approach is pictured. The only element which exhibits more than the usual two degrees of freedom is the intersected element in the middle. The elements next to it are usual elements.*

In contrast to that the discretization with the XFEM which is displayed on the right hand side requires transition elements. The elements next to the intersected element possess usual and enhanced degrees of freedom and need a special treatment.

3.5.2. Discrete weak formulation

The elements which are not crossed by a discontinuity are usual isoparametric elements. The domain \mathcal{B} is discretized with n_{el} elements. The geometry \mathbf{x} is expanded elementwise by shape functions N^i in terms of the discrete nodal positions \mathbf{x}_i of the $i = 1, n_{en}$ element nodes

$$\mathcal{B} = \bigcup_e \mathcal{B}_e \quad \mathbf{x}|_{\mathcal{B}_e} = \sum_{i=1}^{n_{en}} N^i \mathbf{x}_i. \quad (3.5.5)$$

Following the isoparametric concept, the unknown displacement field \mathbf{u} is interpolated on the element level with the same shape functions in terms of the nodal displacement values \mathbf{u}_i . These shape functions are also applied to interpolate the test function $\delta\mathbf{u}$ in the spirit of the Bubnov-Galerkin technique

$$\mathbf{u}|_{\mathcal{B}_e} = \sum_{i=1}^{n_{en}} N^i \mathbf{u}_i \quad \delta\mathbf{u}|_{\mathcal{B}_e} = \sum_{i=1}^{n_{en}} N^i \delta\mathbf{u}_i. \quad (3.5.6)$$

Based on the above discretization the corresponding gradients $\nabla^s \mathbf{u}$ and $\nabla^s \delta\mathbf{u}$ take the format

$$\nabla^s \mathbf{u}|_{\mathcal{B}_e} = \sum_{i=1}^{n_{en}} (\mathbf{u}_i \otimes \nabla N^i)^s \quad \nabla^s \delta\mathbf{u}|_{\mathcal{B}_e} = \sum_{i=1}^{n_{en}} (\delta\mathbf{u}_i \otimes \nabla N^i)^s. \quad (3.5.7)$$

The approximation of the jump in the displacement field arises automatically from the approximation of the two continuous parts of the displacement field

$$\begin{aligned} \llbracket \mathbf{u} \rrbracket|_{\Gamma_e} &= \sum_{i=1}^{n_{en}^+} N^i|_{\Gamma_e} \mathbf{u}_i^+ - \sum_{i=1}^{n_{en}^-} N^i|_{\Gamma_e} \mathbf{u}_i^- = \sum_{p=1}^{n_{en}^+ + n_{en}^*} J^p \mathbf{u}_p \\ \llbracket \delta \mathbf{u} \rrbracket|_{\Gamma_e} &= \sum_{i=1}^{n_{en}^+} N^i|_{\Gamma_e} \delta \mathbf{u}_i^+ - \sum_{i=1}^{n_{en}^-} N^i|_{\Gamma_e} \delta \mathbf{u}_i^- = \sum_{p=1}^{n_{en}^+ + n_{en}^*} J^p \delta \mathbf{u}_p \end{aligned} \quad (3.5.8)$$

Thereby \mathbf{u}_i^+ and \mathbf{u}_i^- denote the displacements at the element nodes n_{en}^+ and n_{en}^- , belonging to \mathcal{B}_d^+ and \mathcal{B}_d^- , respectively. The newly introduced term J comprises the shape functions N , evaluated on Γ_e and associated with the appropriate algebraic sign, '+' for degrees of freedom belonging to \mathcal{B}_d^+ and '-' for those in \mathcal{B}_d^- . Obviously the jump is approximated with the same polynomial degree as the displacement field.

By means of the described discretization of the primary unknown, the weak formulation (3.3.3) is discretized and the discrete algorithmic balance of momentum follows as

$$\mathbf{R}_I = \mathbf{R}_I^{int} + \mathbf{R}_I^{coh} - \mathbf{R}_I^{ext} \quad (3.5.9)$$

whereby the vector-valued residual is composed of the internal forces, the cohesive forces and the external forces. The internal force consists of contributions of the elements belonging to \mathcal{B}^+ , \mathcal{B}^- and of the discontinuous elements \mathcal{B}_d

$$\begin{aligned} \mathbf{R}_I^{int} &= \mathbf{A}_{e=1}^{n_{el}} \int_{\mathcal{B}_e^{+,-}} \nabla N^i \cdot \boldsymbol{\sigma} dV + \int_{\mathcal{B}_d^+} \nabla \bar{N}^{+i} \cdot \boldsymbol{\sigma} dV + \int_{\mathcal{B}_d^-} \nabla \bar{N}^{-i} \cdot \boldsymbol{\sigma} dV \\ \mathbf{R}_I^{coh} &= \mathbf{A}_{e=1}^{n_{el}} \int_{\Gamma_e} J^i \bar{\mathbf{t}}(\llbracket \mathbf{u} \rrbracket) dA \\ \mathbf{R}_I^{ext} &= \mathbf{A}_{e=1}^{n_{el}} \int_{\partial \mathcal{B}_t} N^i \mathbf{t}^p dA. \end{aligned} \quad (3.5.10)$$

Herein the operator $\mathbf{A}_{e=1}^{n_{el}}$ denotes the assembly of all element contributions at the element nodes, including the newly introduced ones, $i = 1, n_{en} + n_{en}^*$ to the overall residual at the global node points $I = 1, n_{np} + n_{np}^*$.

3.5.3. Linearized discrete weak formulation

Equation (3.5.10) represents the governing discrete system of equations. Due to the applied constitutive law and the changing boundary conditions the system of equations becomes nonlinear and has to be solved iteratively. A Newton-Raphson scheme is applied and therefore a consistent linearization of the governing equations is performed

$$\mathbf{R}_I^{k+1} = \mathbf{R}_I^k + d\mathbf{R}_I = \mathbf{0} \quad \text{with} \quad d\mathbf{R}_I = \sum_{J=1}^{n_{np} + n_{np}^*} \mathbf{K}_{IJ} d\mathbf{u}_J, \quad (3.5.11)$$

whereby the iterative residual $d\mathbf{R}_I$ is expressed in terms of the global tangent stiffness matrix \mathbf{K}_{IL} . The tangential stiffness matrix is obtained as the partial derivative of the residual with respect to the displacements

$$\mathbf{K}_{IJ} = \frac{\partial \mathbf{R}_I}{\partial \mathbf{u}_J} = \mathbf{K}_{IJ}^{int} + \mathbf{K}_{IJ}^{coh}. \quad (3.5.12)$$

For the considered problem the tangent stiffness matrix takes the format

$$\begin{aligned} \mathbf{K}_{IJ}^{int} &= \mathbf{A} \int_{e=1}^{n_{el}} \int_{\mathcal{B}_e^{+,-}} \nabla N^i \cdot \mathbf{C} \cdot \nabla N^j dV + \int_{\mathcal{B}_d^+} \nabla \bar{N}^{+i} \cdot \mathbf{C} \cdot \nabla \bar{N}^{+j} dV \\ &\quad + \int_{\mathcal{B}_d^-} \nabla \bar{N}^{-i} \cdot \mathbf{C} \cdot \nabla \bar{N}^{-j} dV \\ \mathbf{K}_{IJ}^{coh} &= \mathbf{A} \int_{e=1}^{n_{el}} \int_{\Gamma_e} J^i \mathbf{T} J^j dA. \end{aligned} \quad (3.5.13)$$

Herein \mathbf{T} represents the tangent stiffness of the traction separation law at the discontinuity, which was specified in section 3.4.2.

Finally the iterative update of the global unknown \mathbf{u}_L

$$\mathbf{u}_J^{k+1} = \mathbf{u}_J^k + d\mathbf{u}_J \quad (3.5.14)$$

can be expressed in terms of the solution of the linearized equation (3.5.11).

3.6. Implementation

In this section details about the implementation of the method are given. In contrast to the approach introduced in the previous chapter the failure surface is not known a priori. Therefore a procedure to estimate the crack propagation direction is required. Furthermore we need to propose a failure criterion to decide if crack propagation occurs. Moreover, the integration of the intersected elements necessitates a modified and adequate integration scheme.

3.6.1. Propagation of the discontinuity

A discontinuity is introduced in an element when a certain failure criterion is met. During the calculation the principal stresses in the element ahead of the tip of the discontinuity are monitored. If the stresses exceed the tensile strength f_t of the material, a discontinuity is introduced. The discontinuity is introduced as a straight line through the element and is enforced to be geometrically continuous. To determine the right direction of the extension of the discontinuity we follow the suggestion of Wells [130]. Since the gradients of the stresses close to the tip of the discontinuity are large, non-local stresses $\tilde{\boldsymbol{\sigma}}$ are calculated

in view of finding the principal directions. The non-local stress tensor is computed as a weighted average of the stresses at the n_{gp} Gauss points within an interaction radius around the tip. A weighted Gauss function is used

$$\hat{w}(r) = \frac{1}{l\sqrt{2\pi}} \exp\left(\frac{-r^2}{[2l]^2}\right), \quad w(r) = \frac{\hat{w}(r)}{\sum_{i=1}^{n_{gp}} \hat{w}_i A_i}, \quad (3.6.1)$$

whereby r is the distance of the Gauss point to the crack tip and l determines the decline of \hat{w} with respect to r . The non-local stress tensor results from the sum of the local stresses at the Gauss points i , weighted with w_i and the associated area A_i

$$\tilde{\sigma}(\mathbf{x}) = \sum_{i=1}^{n_{gp}} \sigma_i w_i A_i. \quad (3.6.2)$$

The discontinuity is extended in the direction perpendicular to the dominant non-local principal stress direction.

In combination with the cohesive zone law this stress-based propagation criterion leads to reasonable results for the crack path. Nevertheless other crack propagation criteria can be used in combination with the proposed method. A promising alternative is given by the Material Force Method, see e. g. [117] and [28] and appendix C.

3.6.2. Additional nodes

The jump in the displacement field should be continuous over the element boundaries. Therefore the newly introduced degrees of freedom have to be global. If an additional node is introduced, it is checked, if the node has already been created by the neighboring elements. To enforce the continuity of the crack path, the discontinuity is always continued at the old crack tip. Furthermore the jump in the displacement field at the discontinuity tip must be equal to zero. To enforce this condition, no additional degrees of freedom are introduced at the nodes, which lie on the same element boundary as the tip of the discontinuity. In figure 3.7(a) the path of the discontinuity is depicted and the additional

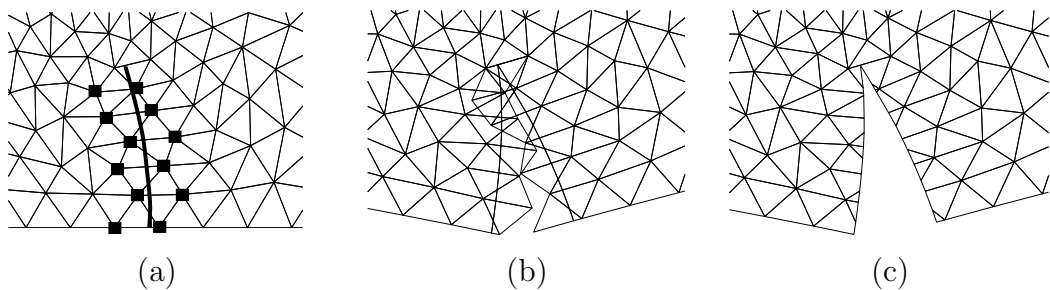


Figure 3.7.: (a) finite element mesh with additional nodes, (b) displacement approximation using doubled nodes, (c) resulting discontinuous approximation

nodes are highlighted, figure 3.7(b) displays the deformation of the structure, including

the additional fictitious nodes, and finally in figure 3.7(c) the resulting deformation of the structure is displayed.

In this formulation a discontinuity can only be introduced if a state of equilibrium is reached. An incremental displacement or force is applied to the structure and the resulting deformation is calculated. Within a post-processing step the Cauchy stresses and the non-local stresses around the tip of the discontinuity are determined. The failure criterion is checked for the crack-tip element. If the failure criterion is met the discontinuity is extended through the crack-tip element in the direction estimated by means of the non-local stresses. Due to the introduction of the new discontinuity the geometry of the structure has changed and the previously computed displacements does not represent an equilibrium state anymore. Therefore the same load step is recalculated with the elongated discontinuity. The procedure is repeated until an equilibrium state is reached and the failure criterion is not met. Then the next load increment is applied. The algorithmic implementation is summarized in figure 3.8.

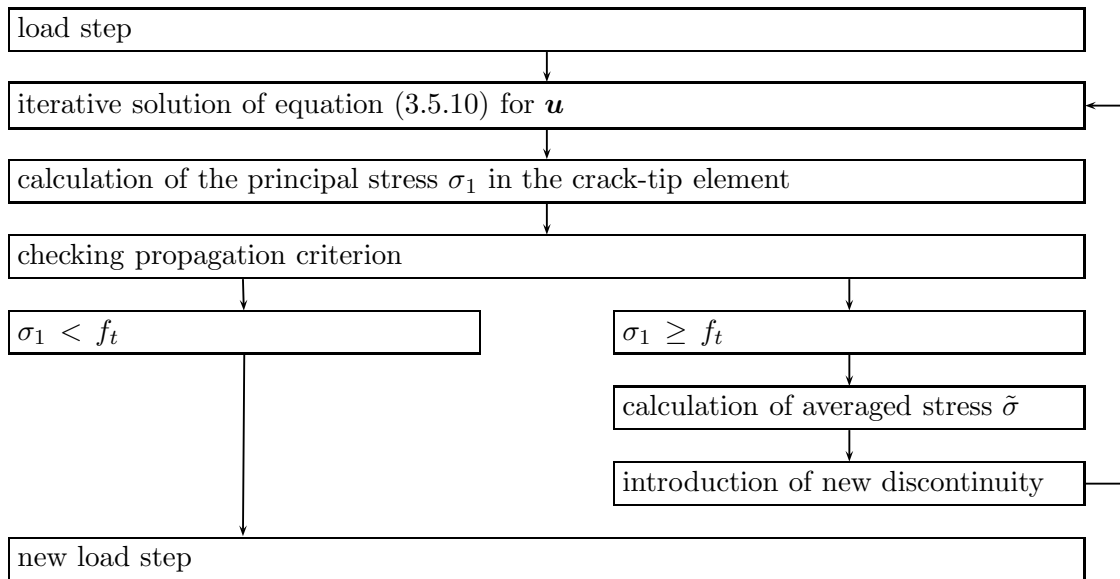


Figure 3.8.: Algorithmic implementation

3.6.3. Integration scheme

For the approximation of the displacement field of the intersected elements the usual shape functions are used. But since the geometry of the element parts varies, the initial Gauss scheme is not valid for the intersected elements. Therefore the quadrilateral part of the intersected element is subdivided into triangular parts. Within each triangular subdomain centroid Gaussian quadrature is applied. This approach is sufficient for constant strain triangles, for higher-order elements one needs to introduce more Gauss points for each

subdomain. Additionally two Gauss points are placed on the discontinuity surface to evaluate the terms depending on the tractions, see figure 3.9.

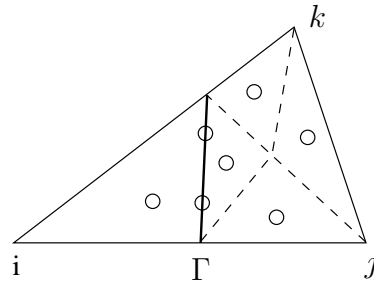


Figure 3.9.: Gauss integration points

3.7. Numerical examples

In this section three numerical examples are presented to demonstrate the applicability of the proposed method in the geometrically linear case. By means of the first example, a simple mode *I* failure problem, the influence of different discretizations and the implementation of the proposed method is checked. The second example, a three-point bending beam with a centrally initiated discontinuity, tests the method for objectivity with respect to mesh alignment and element size. Both the path of the discontinuity and the global load displacement relation are examined for two different discretizations. The third example deals with the same three-point-bending beam, but the discontinuity is initiated excentered, to demonstrate an example for a curved discontinuity. All examples are calculated using three-noded triangles.

3.7.1. Mode I failure

In the first example purely mode *I* failure is considered, to check the influence of different discretizations on the load displacement relation. A square plate is loaded by a given uniform displacement at the top edge and is fixed at the bottom edge, the geometry and the loading conditions are depicted in figure 3.10. The discontinuity is introduced on the left hand side of the plate.

The material parameters are set to: Young's modulus $E = 100 \text{ N/mm}^2$, Poisson's ratio $\nu = 0$, tensile strength $f_t = 1.0 \text{ N/mm}^2$ and fracture energy $G_f = 0.02 \text{ N/mm}$. Due to the bearings, which prevent a lateral movement of the structure, and due to the cohesive forces acting on the interface, the complete separation of the structure does not result in a singular tangent stiffness matrix. In figure 3.11 the deformation of the plate for the three chosen discretizations with 32, 72 and 128 three-noded triangles is pictured. Since the stresses are constant, the discontinuity propagates through the whole structure, when the tensile strength is exceeded. Furthermore it propagates along a straight line, as expected.

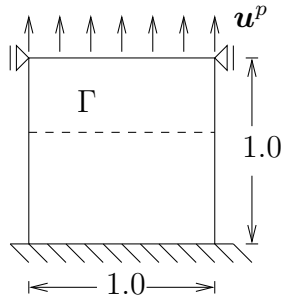


Figure 3.10.: Geometry, loading conditions

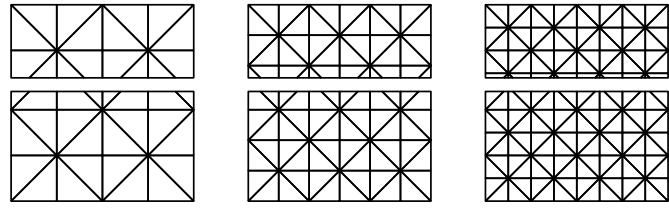


Figure 3.11.: Deformation of the structure

The load displacement relations, which are depicted in figure 3.12, confirm that the results are independent with respect to the discretization.

The example was also calculated under loading and following unloading conditions, when the prescribed displacement is equal 0.7 mm . To realize an irreversible material behavior for the loading/unloading conditions, a history variable q is introduced in the traction separation law (3.4.5). For mode I failure the normal jump seems to be a reasonable choice for the history variable. We obtain the following loading function f and a modified traction separation relation for the normal part of the traction vector

$$\begin{aligned}
 q &= \max(q, \llbracket u_n \rrbracket) & f &= \llbracket u_n \rrbracket - q \\
 t_n &= f_t \exp\left(-\frac{f_t}{G_f} q\right) & \text{if } f &= 0 \\
 t_n &= f_t \exp\left(-\frac{f_t}{G_f} q\right) \frac{\llbracket u_n \rrbracket}{q} & \text{if } f < 0.
 \end{aligned} \tag{3.7.1}$$

If unloading and reloading occurs the material answer follows a linear path. This is numerically verified in figure 3.12. The unloading leads to a damage like release of stresses and the answer during reloading follows the same path in the opposite direction.

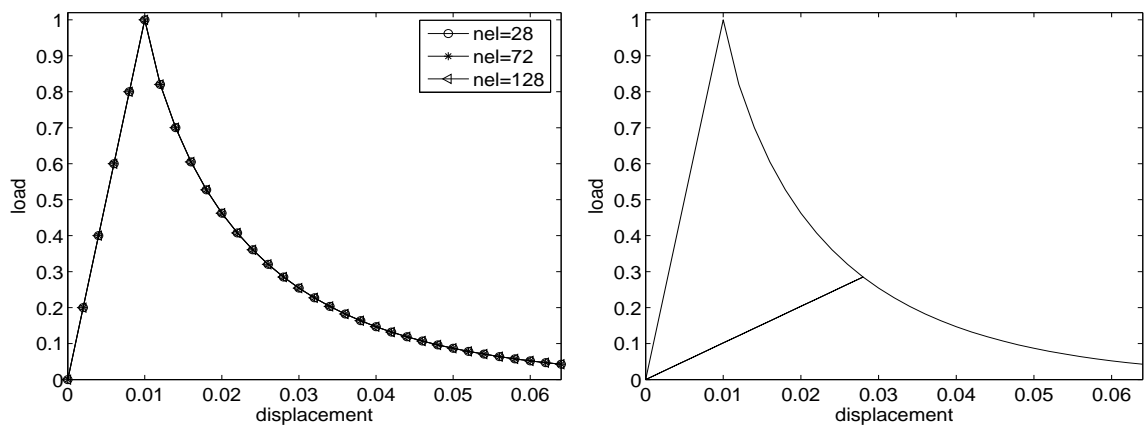


Figure 3.12.: Load displacement relation

3.7.2. Three-point bending beam

We consider a three-point bending test, whereby a simply supported beam is loaded by an imposed displacement at the center of the top edge. The following material parameters are chosen: $E = 100 \text{ N/mm}^2$, $\nu = 0$, $f_t = 0.5 \text{ N/mm}^2$ and $G_f = 0.01 \text{ N/mm}$. The crack shear stiffness d is set to zero. The parameter l from equation (3.6.1) is approximately equal to three times the average element diameter. In figure 3.13 the geometry and the loading conditions are pictured. Two different unstructured meshes with 498 and 850 elements are used for the simulation. The main goal is to examine the dependence of the alignment and the propagation of the crack with respect to the discretization. For

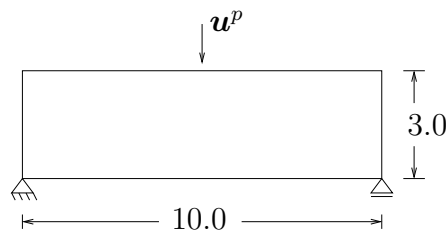


Figure 3.13.: Geometry, loading condition

the first calculation a crack is initiated at the center of the bottom edge. As expected, due to the symmetric setting, the crack propagates directly upwards independently of the mesh alignment. The load displacement relations are shown in figure 3.14. The peak load for the two different discretizations is slightly different. Due to the proposed failure criterion, which depends only on the maximum principal stress in the element ahead of the tip, the larger elements of the coarse mesh fail later. Therefore the peak load is slightly overestimated for the coarse discretization. But nevertheless the good agreement of the two load displacement curves confirms the objectivity of the method with respect to the discretization. The path of the discontinuity is pictured in figure 3.15. For both discretizations the discontinuity describes a straight line towards the top of the beam. The path of the discontinuity is entirely independent of the mesh structure and identical for both discretizations.

In the next example the ability of the method to model a curved crack is tested. Therefore a concentric crack is initiated at the bottom edge of the beam (with 0.7 mm offset). The crack is expected to propagate in a curved path towards the center at the top of the beam, compare the experimental results in [110]. In figure 3.17 the propagation of the crack for both discretizations is displayed and with both discretizations the expected curved path of the crack is well described. Even the simulation with the coarse mesh gives a good approximation of the crack path, the result can not be distinguished from the one obtained with the fine discretization.

The load displacement relations, pictured in figure 3.16, show minor differences. The peak-load is well approximated in both cases, but the curve is quite rough for the coarse

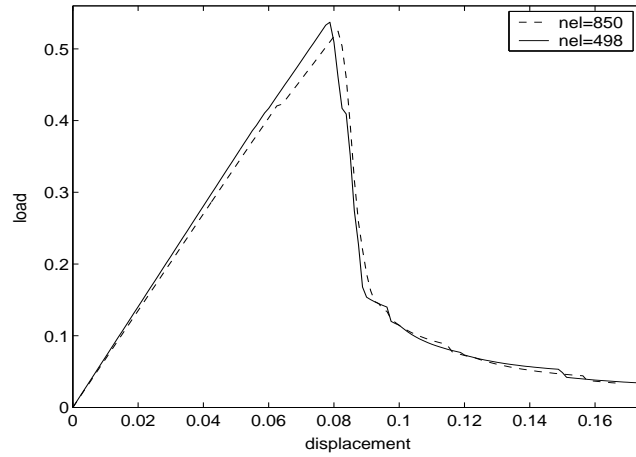


Figure 3.14.: Load displacement relation for centered crack

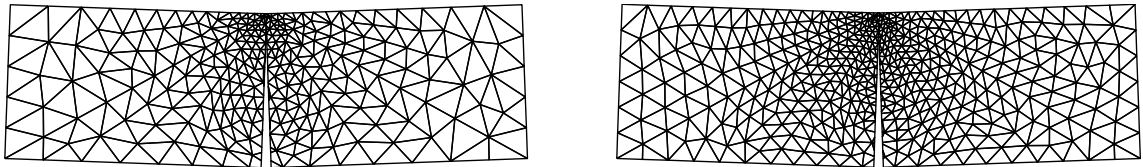


Figure 3.15.: Propagation of the centered discontinuity for both discretizations

mesh. This is due to the elementwise failure. The discontinuity can only intersect the whole element at once and therefore the load displacement relation shows the small jumps. However it is clearly that for a finer discretization these inaccuracies are smoothed out and become negligible for further mesh refinement.

Picture 3.18 shows a detail of the crack path and highlights the independence of the

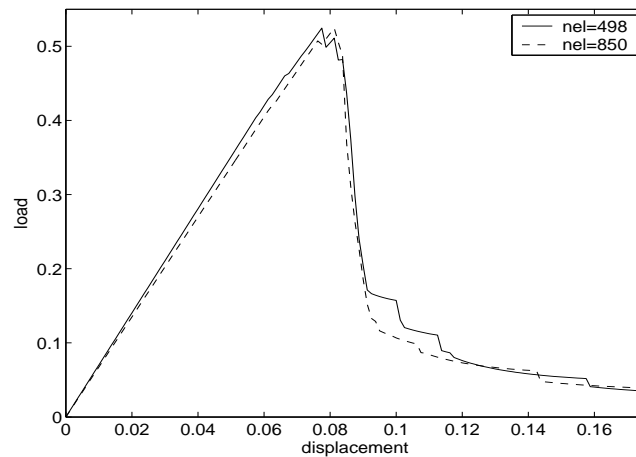


Figure 3.16.: Load displacement relation for excentered crack

crack path with respect to the mesh alignment. It is visible that the elements can be arbitrarily intersected by the discontinuity.

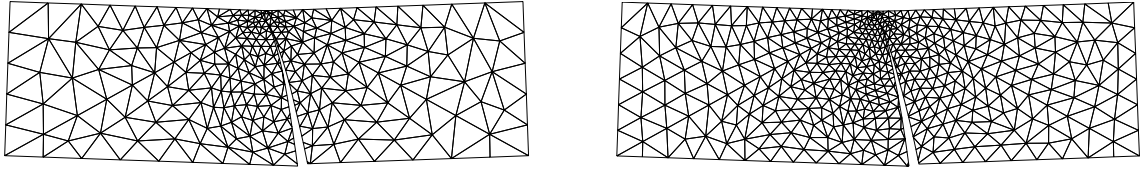


Figure 3.17.: Propagation of the excentered discontinuity for both discretizations

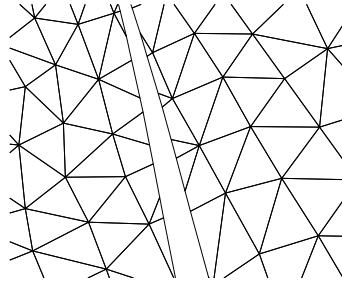


Figure 3.18.: Detail of the discontinuity path

3.8. Summary

A new finite element method was introduced for the modeling of cohesive cracks. The method allows for discontinuities propagating through the elements. The characteristic feature of the method is the construction of these elements which are intersected by the discontinuity. Additional displacement degrees of freedom are introduced at the existing nodes and only the standard basis functions are used. The manner of constructing intersected elements can be easily adapted for different elements in 2D and 3D. The method is used to model cohesive cracks, considering quasi-brittle materials. Thereby the inelastic material behavior is covered by a certain discrete constitutive law, applied at the interface. The introduction of different cohesive traction separation laws is straightforward. A simple crack propagation criterion, based on the maximum principal stresses, is applied. The presented numerical examples point out that the method allows for simulating propagating discontinuities, both, of straight and curved nature, independent of the mesh structure.

4. Mesh-independent modeling of weak discontinuities

In the present chapter a discontinuous Galerkin method, which is based on Nitsche's method [95] and was introduced in chapter 2, is applied for the modeling of weak discontinuities in linear elasticity. A weak discontinuity denotes a jump in the gradient of the displacement field, namely in the strains. These weak discontinuities are present if we consider for example structures, made of different materials or containing holes or inclusions.

Instead of meshing the internal boundaries, the discontinuous elements, proposed in chapter 3.5.1 are combined with the discontinuous Galerkin method. The discontinuous elements allow for jumps in the displacements and in the strains. The discontinuous Galerkin method is applied to enforce continuity of the displacement field in a weak sense, such that only the weak discontinuities remain. The weak discontinuities are therefore modeled independently of the element boundaries.

4.1. Motivation

In structural mechanics internal boundaries with weak discontinuities can occur due to defects, such as pores and inclusions or due to material interfaces, for example in composites. The accurate consideration of these interfaces within finite element method usually requires the meshing of the internal boundaries to obtain optimal convergence rates, see [8] and [76].

Here a different framework is introduced which allows for voids and inclusions of arbitrary geometry independent of the mesh. Therefore discontinuous elements are formulated. The continuity of the displacement field is enforced weakly by means of a discontinuous Galerkin method of Nitsche's type [95]. The method is closely connected to the approach introduced by Hansbo and Hansbo in [46] and [47] and is mainly introduced as a starting point for its extension to finite strains, which is given in chapter 6.

Material discontinuities were considered by MacKinnon et al. in [76] and by Li in [73] by basis functions which satisfy the jump conditions at the interface. In [11] problems with inhomogeneous interface conditions are considered. A different framework to model interfaces independently of the mesh is formed by the extended finite element method (XFEM), which goes back to [14]. Thereby the partition of unity concept [9] is adopted to add additional functions to the usual shape functions. The XFEM was originally developed for crack propagation problems, where the Heaviside function and near crack tip asymptotic fields are used as enrichment functions [87]. The modeling of holes and inclu-

sions by means of the XFEM and level set methods [111] is regarded by Sukumar et al. in [124]. Thereby the displacement field is enriched by additional functions containing a jump in its gradient. These enrichment functions were introduced in connection with the Element Free Galerkin method in [65]. In combination with the level set method the value of the level set function itself can be used to develop an enrichment function. In [124] holes and inclusions are modeled with the XFEM, in [17] arbitrary discontinuities are considered and in [86] the approach is adopted to handle complex microstructure geometries. The combination of the extended finite element method and level set methods was also applied for problems with moving internal interfaces. In [25] and [58] the Stefan problem is simulated, in [24] two-phase fluids are regarded and in [32] an approach to simulate the swelling of hydrogels is introduced. In this context a study of different strategies to enforce interfacial constraints is accomplished in [59].

The present approach is applied to the modeling of inclusions and material interfaces in linear elasticity. The method is based on the unfitted finite element method, introduced by Hansbo and Hansbo in [46] for stationary heat conduction problems and applied in a more general format to elasticity in [47]. The discontinuous elements, which were introduced in [46] and adopted in chapter 3 for crack propagation problems, are utilized. Due to the construction of the shape functions, these elements allow for a discontinuity in the displacement field and its gradient. When weak discontinuities are simulated the displacement field is required to be continuous. To fulfill this condition a Nitsche type discontinuous Galerkin method, which was introduced in section 2.3.2, is applied along the internal interface. By means of the discontinuous Galerkin terms the continuity of the displacement field is weakly satisfied. Nitsche introduced in [95] a consistent method to enforce inhomogeneous Dirichlet boundary conditions in a weak sense. Douglas and Dupont [33], Wheeler [133] and Arnold [6] extended this approach to the weak fulfillment of continuity at all element boundaries.

Although only static interfaces are considered in this approach the geometry of the internal boundary is described by means of level set methods [102] and [111]. Usually the level set method is applied to track moving interfaces, but nevertheless it constitutes a simple manner to describe arbitrarily formed holes and inclusions.

In the next chapter the kinematics regarding a weak discontinuity are introduced, afterwards the variational formulation, including the additional discontinuous Galerkin terms, is derived from the principle of stationary potential energy and the governing equations are constituted. The discretization and implementation is described in detail and finally numerical examples are presented and numerical convergence studies are carried out.

4.2. Kinematics

Let \mathcal{B} denote a linear elastic body with placements denoted by \boldsymbol{x} . The boundary $\partial\mathcal{B}$ with the outward unit normal vector \boldsymbol{n}_e is subdivided into the disjoint parts $\partial\mathcal{B} = \partial\mathcal{B}_u \cup \partial\mathcal{B}_t$ with $\partial\mathcal{B}_t \cap \partial\mathcal{B}_u = \emptyset$, where either Neumann or Dirichlet boundary conditions are prescribed. We assume that the body exhibits an internal discontinuity which is denoted

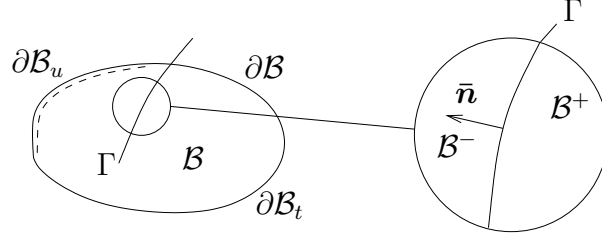


Figure 4.1.: \mathcal{B} crossed by an internal boundary Γ

with Γ and the parts of the body placed on the two sides of the internal boundary with \mathcal{B}^+ and \mathcal{B}^- . The associated normal vector $\bar{\boldsymbol{n}}$ points from \mathcal{B}^- to \mathcal{B}^+ , see figure 4.1. Since the continuity of the displacement field will be enforced by additional terms in the weak form it is possible to use the same kinematical assumption as in chapter 3 for strong discontinuities. Thus two independent unknown displacement fields are defined

$$\boldsymbol{u} = \begin{cases} \boldsymbol{u}^+ & \text{in } \mathcal{B}^+ \\ \boldsymbol{u}^- & \text{in } \mathcal{B}^- \end{cases} \quad (4.2.1)$$

and the symmetric strain tensor is introduced as

$$\boldsymbol{\epsilon} = \begin{cases} \boldsymbol{\epsilon}^+ = \nabla^s \boldsymbol{u}^+ & \text{in } \mathcal{B}^+ \\ \boldsymbol{\epsilon}^- = \nabla^s \boldsymbol{u}^- & \text{in } \mathcal{B}^- \end{cases}. \quad (4.2.2)$$

To treat the discontinuities we define a jump term and an average term

$$[[\boldsymbol{u}]] = \boldsymbol{u}^+|_{\Gamma} - \boldsymbol{u}^-|_{\Gamma} \quad \text{and} \quad \{\boldsymbol{u}\}^{\kappa} = \kappa^+ \boldsymbol{u}^+|_{\Gamma} + \kappa^- \boldsymbol{u}^-|_{\Gamma}, \quad (4.2.3)$$

whereby $\boldsymbol{u}^{\pm}|_{\Gamma}$ indicate the field values on both sides of the internal boundary. In contrast to section 2.2 the average term is introduced as a weighted average with the weighting factors κ^+ and κ^- , with $\kappa^+ + \kappa^- = 1$. The use of the weighted average value instead of the mean average and the particular size of the weighting factors is directly related to the discretization. Their determination will be discussed in section 4.5.1.

4.3. Variational formulation

In this section the variational formulation of the problem is determined from the principle of stationary potential energy. Thereby additional interfacial contributions are added to the potential which ensure the continuity of the displacement field. These additional contributions vanish if the the continuity condition is exactly fulfilled.

4.3.1. Principle of stationary potential energy

To apply the principle of stationary potential energy we propose the existence of an energy functional Π . Usually the total energy is composed of the internal energy Π^{int} and the external energy Π^{ext} . We introduce additional energy contributions Π^{dis} . The definition of the total potential energy reads

$$\Pi(\mathbf{u}) = \Pi^{int} + \Pi^{dis} + \Pi^{ext}. \quad (4.3.1)$$

The internal energy is defined in terms of the strain energy density $\Psi(\boldsymbol{\epsilon})$ and the external energy contains contributions of the body force \mathbf{b} and surface tractions \mathbf{t}^p .

$$\Pi^{int} = \int_{\mathcal{B}^+ \cup \mathcal{B}^-} \Psi(\boldsymbol{\epsilon}(\mathbf{u})) dV \quad \Pi^{ext} = - \int_{\mathcal{B}^+ \cup \mathcal{B}^-} \mathbf{u} \cdot \mathbf{b} dV - \int_{\partial \mathcal{B}_t} \mathbf{u} \cdot \mathbf{t}^p dA. \quad (4.3.2)$$

The additional term Π^{dis} is defined as

$$\Pi^{dis}(\mathbf{u}) = \int_{\Gamma} \llbracket \mathbf{u} \rrbracket \cdot \{\boldsymbol{\sigma}\} \cdot \bar{\mathbf{n}} dA + \int_{\Gamma} \frac{1}{2} \theta \llbracket \mathbf{u} \rrbracket \cdot \llbracket \mathbf{u} \rrbracket dA, \quad (4.3.3)$$

whereby $\boldsymbol{\sigma}$ denotes the Cauchy stress. It can be easily verified that this contribution vanishes if the continuity of the displacement field is satisfied, i. e. $\llbracket \mathbf{u} \rrbracket = \mathbf{0}$. The second part of Π^{dis} forms a penalty term, which is necessary to stabilize the method, compare section 2.4.3. The penalty factor θ depends on the material parameters and the discretization and will be specified in section 4.5. The total potential energy is then given as

$$\begin{aligned} \Pi(\mathbf{u}) = & \int_{\mathcal{B}^+ \cup \mathcal{B}^-} \Psi(\boldsymbol{\epsilon}(\mathbf{u})) dV + \int_{\Gamma} \llbracket \mathbf{u} \rrbracket \cdot \{\boldsymbol{\sigma}\} \cdot \bar{\mathbf{n}} dA + \int_{\Gamma} \frac{1}{2} \theta \llbracket \mathbf{u} \rrbracket \cdot \llbracket \mathbf{u} \rrbracket dA \\ & - \int_{\mathcal{B}^+ \cup \mathcal{B}^-} \mathbf{u} \cdot \mathbf{b} dV - \int_{\partial \mathcal{B}_t} \mathbf{u} \cdot \mathbf{t}^p dA. \end{aligned} \quad (4.3.4)$$

Equilibrium is obtained when the total potential energy reaches a stationary point, i. e. when its variation with respect to the displacement field vanishes. The variational formulation reads

$$\begin{aligned} \delta \Pi(\mathbf{u}, \delta \mathbf{u}) = & \int_{\mathcal{B}^+ \cup \mathcal{B}^-} \boldsymbol{\sigma} : \delta \boldsymbol{\epsilon} dV + \int_{\Gamma} [\llbracket \delta \mathbf{u} \rrbracket \cdot \{\boldsymbol{\sigma}\} \cdot \bar{\mathbf{n}} + \llbracket \mathbf{u} \rrbracket \cdot \{\delta \boldsymbol{\sigma}\} \cdot \bar{\mathbf{n}}] dA \\ & + \int_{\Gamma} \theta \llbracket \delta \mathbf{u} \rrbracket \cdot \llbracket \mathbf{u} \rrbracket dA - \int_{\mathcal{B}^+ \cup \mathcal{B}^-} \delta \mathbf{u} \cdot \mathbf{b} dV - \int_{\partial \mathcal{B}_t} \delta \mathbf{u} \cdot \mathbf{t}^p dA \doteq 0, \end{aligned} \quad (4.3.5)$$

whereby the Cauchy stress tensor is defined as the derivative of the strain energy density with respect to the strain $\boldsymbol{\sigma} = \partial \Psi / \partial \boldsymbol{\epsilon}$. To clarify the underlying interfacial conditions the term on the internal boundary Γ is analyzed. Since all the integral terms are inexistent in continuous weak formulations, they have to vanish, if the interface conditions are exactly

satisfied. The last two terms, evaluated on Γ contain the jump in the displacement field. When the continuity condition

$$[[\mathbf{u}]] = \mathbf{0} \quad \text{on} \quad \Gamma \quad (4.3.6)$$

is fulfilled these terms are equal to zero. The remaining term provides the equilibrium of the tractions along the internal interface, i. e. $\{\boldsymbol{\sigma}\} \cdot \bar{\mathbf{n}} = \boldsymbol{\sigma}^+ \cdot \bar{\mathbf{n}} = \boldsymbol{\sigma}^- \cdot \bar{\mathbf{n}}$. Then it can be shown by means of the divergence theorem and integration by parts that the weak form is consistent with the following strong form

$$\begin{aligned} -\operatorname{div} \boldsymbol{\sigma} &= \mathbf{b} & \text{in} & \quad \mathcal{B}^+ \cup \mathcal{B}^- \\ \mathbf{u} &= \mathbf{u}^p & \text{on} & \quad \mathcal{B}_u \\ \boldsymbol{\sigma} \cdot \mathbf{n}_e &= \mathbf{t}^p & \text{on} & \quad \mathcal{B}_t \\ [[\boldsymbol{\sigma}]] \cdot \bar{\mathbf{n}} &= \mathbf{0} & \text{on} & \quad \Gamma \\ [[\mathbf{u}]] &= \mathbf{0} & \text{on} & \quad \Gamma. \end{aligned} \quad (4.3.7)$$

The additional terms due to the discontinuous Galerkin method ensure the continuity of \mathbf{u} over the internal boundary in a weak sense.

4.4. Constitutive equation

We assume linear elastic behavior of the body. Therefore the strain energy function is defined as

$$\Psi(\boldsymbol{\epsilon}) = \frac{1}{2} \boldsymbol{\epsilon} : \mathbf{C} : \boldsymbol{\epsilon} \quad (4.4.1)$$

and the stress-strain relation follows as

$$\boldsymbol{\sigma} = \frac{\partial \Psi(\boldsymbol{\epsilon})}{\partial \boldsymbol{\epsilon}} = \mathbf{C} : \boldsymbol{\epsilon}. \quad (4.4.2)$$

Thereby \mathbf{C} is the elasticity tensor, which depends for isotropic material behavior only on two material parameters, e. g. the Lamé parameters λ and μ . Then the stress strain relation can be rewritten as

$$\boldsymbol{\sigma} = \lambda \operatorname{tr}(\boldsymbol{\epsilon}) \mathbf{I} + 2\mu \boldsymbol{\epsilon}. \quad (4.4.3)$$

To simplify matters we choose the same linear elastic behavior for both parts of the body, \mathcal{B}^+ and \mathcal{B}^- . In general the material behavior of the parts is independently and can be defined by different strain energy functions. However, in the present study the difference between the material behavior of the parts is restricted to varying material parameters.

4.5. Discretization

In this section the discretization of the weak formulation is described. Since the weak discontinuities shall be independent of the finite element mesh the weak formulation 4.3.5 is discretized with the discontinuous elements, which were established in chapter 3.5.1 for the modeling of crack propagation. Due to the set of discontinuous shape functions, these intersected elements allow for the approximation of two independent functions, and thus for jumps in the displacement field and the strains. In contrast to the application of these elements for crack modeling, where a displacement jump is required, the continuity of the displacement field is here enforced weakly by Nitsche's method. Consequently only the jumps in the strain field, namely the weak discontinuities, remain.

4.5.1. Discontinuous elements

The formulation of the discontinuous elements is described in detail in section 3.5. An intersected element is divided by Γ_e into the parts \mathcal{B}_d^+ and \mathcal{B}_d^- with the independent displacement fields \mathbf{u}^+ and \mathbf{u}^- . To approximate the displacement field additional degrees of freedom are introduced at the existing nodes and discontinuous shape functions are defined on the basis of the standard shape functions

$$N^{+i} = \begin{cases} N^i & \text{in } \mathcal{B}_d^+ \\ 0 & \text{in } \mathcal{B}_d^-, \end{cases} \quad \text{and} \quad N^{-i} = \begin{cases} 0 & \text{in } \mathcal{B}_d^+ \\ N^i & \text{in } \mathcal{B}_d^-. \end{cases} \quad (4.5.1)$$

The approximation of the displacement jump and average of the strains which have to be evaluated at the internal interface reads

$$\begin{aligned} \llbracket \mathbf{u} \rrbracket|_{\Gamma_e} &= \sum_{i=1}^{n_{en^+}} N^i|_{\Gamma_e} \mathbf{u}_i^+ - \sum_{i=1}^{n_{en^-}} N^i|_{\Gamma_e} \mathbf{u}_i^- = \sum_{p=1}^{n_{en^+} + n_{en^-}} J^p \mathbf{u}_p \\ \{ \mathbf{u} \}|_{\Gamma_e} &= \kappa^+ \sum_{i=1}^{n_{en^+}} N^i|_{\Gamma_e} \mathbf{u}_i^+ + \kappa^- \sum_{i=1}^{n_{en^-}} N^i|_{\Gamma_e} \mathbf{u}_i^- = \sum_{p=1}^{n_{en^+} + n_{en^-}} A^p \mathbf{u}_p. \end{aligned} \quad (4.5.2)$$

The newly introduced terms J^p and A^p comprise the shape functions evaluated at the internal boundary and the appropriate sign for the jump term or the weighting factors κ for the average value. The size of the weighting factors is defined according to [46] by the size of the two parts of the intersected element

$$\kappa^+ = \frac{|\mathcal{B}_d^+|}{|\mathcal{B}_d|} \quad \text{and} \quad \kappa^- = \frac{|\mathcal{B}_d^-|}{|\mathcal{B}_d|}. \quad (4.5.3)$$

The introduction of this weighted average term is necessary since the interface can intersect the elements arbitrarily. Therefore the geometry of the intersected elements is not fully characterized by the mesh size h . Another definition of the weighting factors is possible. In reference [47] κ is defined as

$$\kappa^+ = \begin{cases} 1 & \text{if } |\mathcal{B}_d^+| > |\mathcal{B}_d^-| \\ 0 & \text{if } |\mathcal{B}_d^+| < |\mathcal{B}_d^-|, \end{cases} \quad \text{and} \quad \kappa^- = 1 - \kappa^+. \quad (4.5.4)$$

That means that the average values in an intersected element are computed at that side of the interface where the larger part of the element resides.

In chapter 2 the Nitsche type discontinuous Galerkin method is applied along element boundaries in structured meshes. Hence the introduction of an average weighting factor is not required and the usual arithmetic mean is used.

4.5.2. Discrete weak formulation

The elements which are not intersected by the discontinuity are usual isoparametric elements, as described in section 3.5. The discretization of the weak formulation 4.3.5 leads to a linear system of equations which can be solved directly. The global load vector is simply given by

$$\mathbf{F}_I = \mathbf{A}_{e=1}^{n_{el}} \int_{\mathcal{B}^+ \cup \mathcal{B}^-} N^i \mathbf{b} dV + \int_{\partial \mathcal{B}_t} N^i \mathbf{t}^p dA. \quad (4.5.5)$$

The stiffness matrix is composed of the usual bulk contribution and the additional dG interfacial contributions

$$\begin{aligned} \mathbf{K}_{IJ} = & \mathbf{A}_{e=1}^{n_{el}} \int_{\mathcal{B}_{e,d}^{+,-}} \nabla N^i \mathbf{C} \nabla N^j dV \\ & + \int_{\Gamma_e} \left[J^i \mathbf{C} \cdot \bar{\mathbf{n}} \cdot \nabla A^j + \nabla A^i \cdot \bar{\mathbf{n}} \cdot \mathbf{C} J^j \right] dA + \int_{\Gamma_e} \theta_e J^i J^j dA \end{aligned} \quad (4.5.6)$$

The penalty factor θ_e depends on the material parameters and the mesh size h . It can be specified as $\theta_e = \vartheta (\lambda_{max} + \mu_{max})/h$, whereby ϑ is a scalar-valued constant which has to be sufficiently large to ensure stability of the method, see [46] for a stability proof. Obviously equation 4.5.6 renders a symmetric linear system of equations, which is solved for the primary unknown \mathbf{u} , which results in $\sum_{L=1}^{n_{np}} \mathbf{K}_{IJ} \mathbf{u}_J = \mathbf{F}_I$.

4.6. Implementation

In this section the implementation of the proposed method is described. Thereby the focus lies on the introduction of the additional nodes and the geometric description of the interface by means of level set methods. The numerical integration of the intersected elements and the additional boundary contributions is carried out by a special Gauss integration scheme, which is described in section 3.6.3.

4.6.1. Geometric description of the interface

Although only stationary interfaces are considered, the geometry of the internal boundaries is defined by means of level set functions [111]. The idea of the level set method is

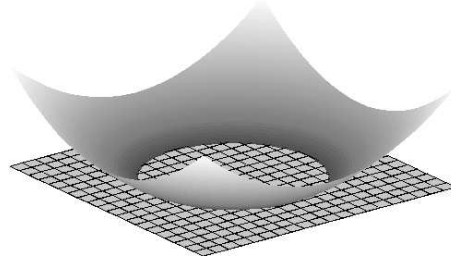


Figure 4.2.: Level set description of circular inclusion

to represent an interface as the zero level set of a function $l(\mathbf{x}, t)$, which is one dimension higher than the considered problem. A moving interface Γ in two dimensions can be described as

$$\Gamma(t) = \{\mathbf{x} \in \mathbb{R}^2 : l(\mathbf{x}, t) = 0\}. \quad (4.6.1)$$

In the here considered examples the interface is static, therefore the dependence on the time t is omitted. However, in general the time dependence of the interface can be easily included, which requires the definition of an evolution equation for the level set function to describe its motion.

To illustrate the concept of the geometry description, we exemplarily look at a circular inclusion. The level set function is given as

$$l(\mathbf{x}) = \|\mathbf{x} - \mathbf{x}^c\| - r, \quad (4.6.2)$$

whereby the center of the circle is denoted with \mathbf{x}^c and the radius with r . In figure 4.2 one can see that the zeros of the function l constitute a circular interface, the function values of the coordinates inside this circle are lower and of the external ones are larger than zero.

To determine the position of the interface in the context of finite element methods, the discrete function values of l are determined at the nodes. Therefore the elements which belong to \mathcal{B}^+ or \mathcal{B}^- can be identified by the sign of their nodal values of l . Elements which are intersected by the interface possess nodal values with different signs. If linear triangular elements are considered, the interface is described as a straight line in the element and the intersection points of the interface with the element boundaries are the zeros of the discrete level set function l .

4.6.2. Additional nodes

The formulation of the discontinuous elements requires the introduction of additional nodes. Since only static interfaces are considered the additional nodes can be introduced

prior to the calculation. To identify the elements which are intersected it is looped over all elements. If there are two nodes n_i and n_j in the connectivity of the element with $l_i l_j < 0$ the element becomes a discontinuous element. Additional degrees of freedom are introduced at the nodes of the intersected elements, which is indicated at left hand side of figure 4.3. On the right hand side the intersected elements containing the doubled nodes are depicted completely. Since the additional degrees of freedom are global, it is checked

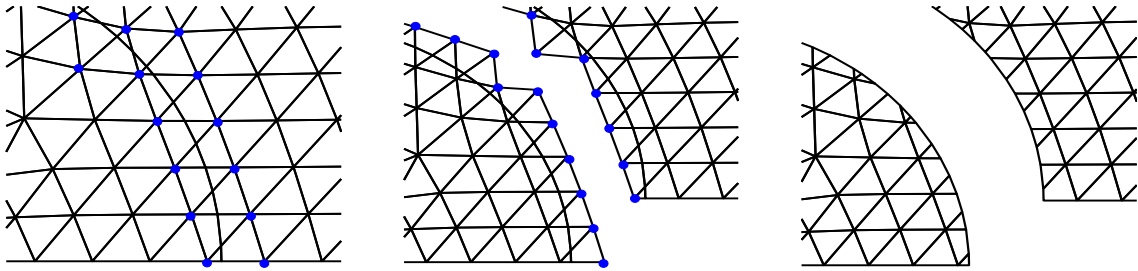


Figure 4.3.: Introduction of the additional nodes

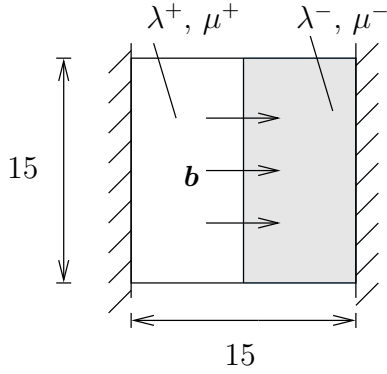
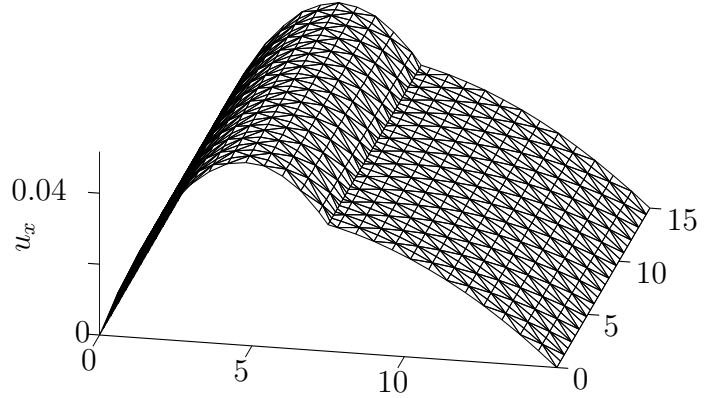
whether the node has already been doubled by another divided element. Furthermore the intersection points of the element edges and the interface are easily calculated as the zeros of the discrete level set function. The intersection points and the geometry of the element parts are stored since they do not change during the calculation.

4.7. Numerical examples

Two numerical examples are presented, which demonstrate the performance of the method. For both examples the calculation of an analytical solution is possible and therefore the numerical solution is analyzed with respect to the analytical one. For both examples the error in the displacement field and in the energy is calculated. The second example is also used to control the stress and strain contributions. Both numerical examples are calculated with a penalty parameter of $\vartheta = 5$, whereby $\theta = \vartheta/h (\lambda_{max} + \mu_{max})$.

4.7.1. Bimaterial bar

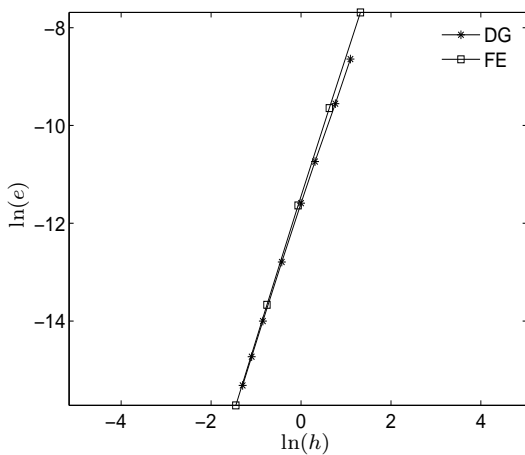
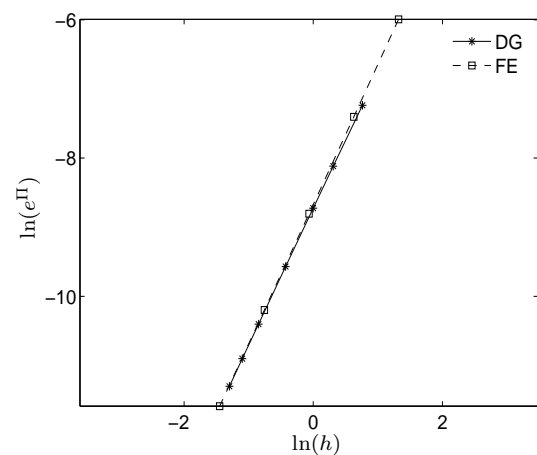
The first example, a bimaterial bar, which is fixed on both sides and loaded by a body force, is taken from [50]. The geometry and the boundary conditions are given in figure 4.4. A material interface is located in the middle of the bar, the material on the left side of the interface, in \mathcal{B}^+ , is softer than the other one. The body force is only applied in x -direction. With the material parameters $E^+ = 0.5$, $E^- = 3$ and $\nu^+ = \nu^- = 0$ a one dimensional problem is characterized, which is solved in a two dimensional setting. The


Figure 4.4.: Geometry

Figure 4.5.: Displacement in x -direction

applied body force and the resulting analytical solution of this problem are given as

$$\mathbf{b} = \begin{bmatrix} 1 \\ 0 \end{bmatrix} \quad \begin{aligned} u_x|_{\mathcal{B}^+} &= \frac{3E^+ + E^-}{4E^{+2} + 4E^+E^-} \frac{x}{15} - \frac{1}{2E^+} \left(\frac{x}{15}\right)^2 \\ u_x|_{\mathcal{B}^-} &= \frac{[E^- - E^+] + [3E^+ + E^-] \frac{x}{15}}{4E^{+2} + 4E^+E^-} - \frac{1}{2E^-} \left(\frac{x}{15}\right)^2. \end{aligned} \quad (4.7.1)$$

The deformation of the bimaterial bar is displayed in figure 4.5, whereas the deformation in x -direction is plotted on the z -axis to visualize the continuity of the solution. The jump in the material parameters leads to a jump in the gradient of the displacements as expected. The jumps within the displacement field along the internal boundary are approximately zero. The numerical solution is compared with the analytical one in order to show convergence of the method. The error in the displacements is calculated as


Figure 4.6.: Error in the displacements

Figure 4.7.: Error in the energy

$e = \|\mathbf{u}^a - \mathbf{u}\|$, whereby \mathbf{u}^a denotes the analytical solution. The error in the energy is calculated as the difference of the numerically determined energy and the analytically

calculated energy $e^\Pi = |\Pi^a - \Pi|$. The latter is for the given example $\Pi^a = 0.03001$. For comparison reasons the bimaterial bar is also calculated with a fitted finite element method. That means that the interface is taken into account such that it coincides with

| nel | e | e^Π |
|------|--------------|-----------|
| 50 | 1.764786e-04 | 1.3622e-3 |
| 98 | 7.096249e-05 | 7.1977e-4 |
| 242 | 2.168587e-05 | 2.9864e-4 |
| 450 | 9.256522e-06 | 1.6250e-4 |
| 1058 | 2.778997e-06 | 6.9919e-5 |
| 2450 | 8.319168e-07 | 3.0450e-5 |
| 4050 | 4.006681e-07 | 1.8510e-5 |
| 6050 | 2.228348e-07 | 1.2442e-5 |

Table 4.1.: Displacement error and energy error for dG method, bimaterial bar

the meshlines. The error in the displacements is shown in figure 4.6. It can be seen that quadratic convergence is achieved for the present method. The error is comparable to the one of the fitted finite element method. The energy error is presented in figure 4.7. Again quadratic convergence is achieved. The numerical values for the displacement and the energy error are summarized in table 4.1.

4.7.2. Circular plate with inclusion

As the second example a more complicated problem is calculated, for which an analytical solution exists: a circular plate with a soft circular inclusion. The example is taken from Sukumar et al. [124]. The geometry and the boundary conditions are given in figure 4.8. Due to the axisymmetric loading the whole problem is axisymmetric. We calculate only

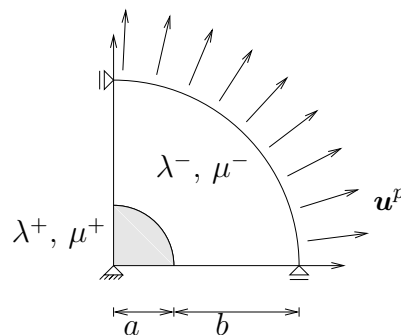


Figure 4.8.: Geometry and loading conditions

one quarter of the problem. The material parameters are constant in each part of the

structure, but exhibit a discontinuity across the internal interface Γ . They are chosen as $\lambda^+ = \mu^+ = 0.4$, $\lambda^- = 5.7692$ and $\mu^- = 3.8461$. At the outer boundary of the circular structure a displacement field is prescribed, which is given in polar coordinates $u_r = b$ and $u_\theta = 0$. Since we consider displacement and traction continuity, compare equations (4.3.6) and (4.3.7), the analytical solution can be specified as

$$\begin{aligned} u_r(r) &= \begin{cases} \left[\left[1 - \frac{b^2}{a^2} \right] \alpha + \frac{b^2}{a^2} \right] r, & 0 \leq r \leq a \\ \left[\left[1 - \frac{b^2}{r^2} \right] \alpha + \frac{b^2}{r^2} \right] r, & a \leq r \leq b \end{cases} \\ u_\theta &= 0, \end{aligned} \quad (4.7.2)$$

whereby

$$\alpha = \frac{[\lambda^+ + \mu^+ + \mu^-] b}{[\lambda^- + \mu^-] a^2 + [\lambda^+ + \mu^+] [b^2 - a^2] + \mu^- b^2}. \quad (4.7.3)$$

In our calculations $a = 3.75$ and $b = 15$. The exact potential energy can be calculated analytically by calculating the stresses and strains from the given displacement field and integrating the strain energy function over \mathcal{B}^+ and \mathcal{B}^- . The potential energy turns out to be equal to $\Pi^a = 2893.954$.

In the same manner as in the first example the convergence of the method is checked by comparison of the numerical with the analytical solution. The problem is calculated with an increasing number of elements. The error in the displacement field is calculated as well as the error in the energy. Both errors are depicted in table 4.2. In figure 4.9 the error in the displacements is plotted and figure 4.10 shows the error in the energy. The convergence results are not as accurate as in the first example, since the meshes show some irregularities. But the expected quadratic convergence behavior in the displacement error and the energy is recognizable. The deformation of the structure as well as the associated stress and strain contributions are displayed in the figure 4.11. The radial displacements u_r are plotted along the z -axis. It is visible that the jump in the displacement field is

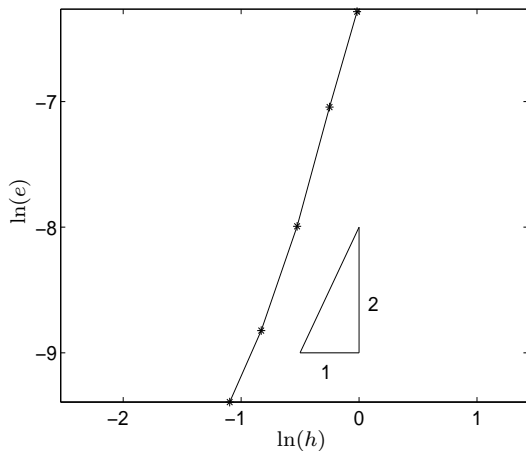


Figure 4.9.: Error in the displacements

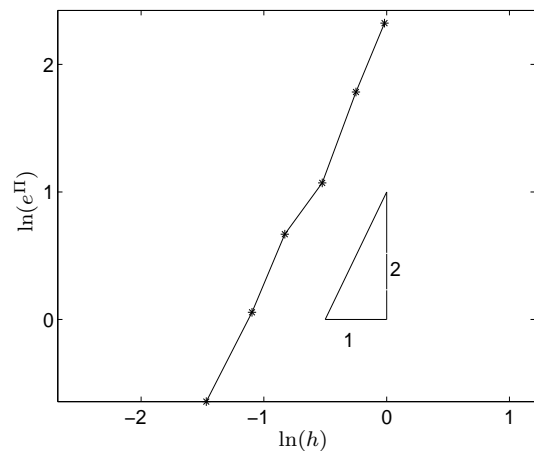


Figure 4.10.: Error in the energy

| nel | e | e^{II} |
|------|--------------|-----------------|
| 367 | 1.864142e-03 | 1.0213e+01 |
| 583 | 8.726288e-04 | 5.9514e+00 |
| 1011 | 3.377139e-04 | 2.9187e+00 |
| 1946 | 1.473069e-04 | 1.9525e+00 |
| 3171 | 8.342057e-05 | 1.0580e+00 |

Table 4.2.: Convergence of the dG approach, circular inclusion

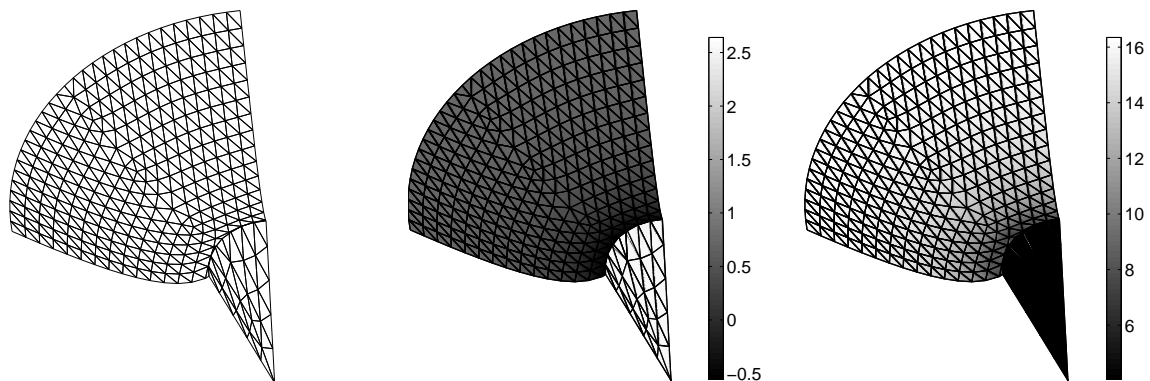


Figure 4.11.: Radial displacements, radial strain and stress contribution

approximately zero at the interface. Furthermore one can see that the gradient of the radial displacement field exhibits a jump along the internal boundary where the material parameters change. This connection becomes apparent when the radial strain contribution is considered. The jump in the radial strains along the interface is clearly visible and well captured by the discontinuous elements. The radial stresses are depicted in figure 4.11 (c). Since traction continuity is required along the internal boundary a continuous transition of the radial stresses is expected and can be verified.

4.8. Summary

In the present chapter an approach was introduced which combines the application of a Nitsche type dG method with discontinuous finite elements for the mesh independent simulation of weak discontinuities. Weak discontinuities denote a jump in the gradients of the displacement field, which occur when one considers material interfaces, holes or inclusions. The discontinuous elements allow for a jump in the displacement field and its gradient. The construction of the elements is very simple and in a uniform manner applicable for elements of different polynomial degree and dimension. The set of discontinuous shape functions offers the possibility to capture arbitrary discontinuities within the elements. The continuity of the displacement field is weakly enforced along the inter-

nal interface by Nitsche's method, which leads to additional terms along the interface. The accuracy of the technique was tested by numerical examples in two dimensional elastostatics. For two problems with known analytical solutions convergence studies were performed. The obtained convergence rates in the displacements and the energy are optimal. Furthermore the jump in the strain field is exactly captured by the discontinuous elements. The results show that the method offers a robust and accurate numerical technique for the modeling of material interfaces, voids and inclusions independent of the interelement boundaries.

5. Mesh-independent modeling of strong discontinuities at finite strains

The approach for the mesh-independent crack modeling which was developed in chapter 3 is extended to finite strains. This chapter is mainly based on reference [82]. The extension to the geometrically nonlinear setting implicates different kinematic relations. The concept of cohesive crack modeling is adopted to model inelastic failure processes. The numerical implementation is based on the discontinuous elements which were introduced in detail in the second chapter and is expanded to three dimensional applications. A consistent linearization of the method is presented, where attention is especially paid to the linearization of the cohesive traction vector. The numerical examples, in two and three dimensions show the mesh-independency of the results.

5.1. Motivation

In this chapter the approach for the modeling of cohesive cracks involving strong discontinuities is extended to large strains. The failure process is dominated by a strain softening processes, where the standard continuum description leads to physically meaningless solutions due to an ill-posedness of the underlying problem. Therefore the discrete crack approach is adopted, where the failure zone is described by means of a strong discontinuity. To include inelastic material behavior a fracture process zone is included by the introduction of a cohesive zone model. The idea of the cohesive zone models goes back to the work of Dugdale [34] for elastoplastic fracture in metals and Barenblatt [10] and Hillerborg et al. [55] for brittle fracture. In the cohesive zone theory the fracture process is seen as a gradual phenomena, whereby the inelastic processes prior to crack initiation are lumped onto a fracture process plane in front of the crack tip. The opening of the adjacent crack surfaces is resisted by cohesive tractions, whose evolution is governed by a constitutive traction separation law. Different inelastic effects like the initiation and coalescence of micro-cracks, void initiation, interlocking of grains and others can be combined in a phenomenological particularization of a traction separation law. The cohesive zone models are widely used in fracture and failure mechanics. In the geometrically nonlinear setting Ortiz and Pandolfi [101] developed an irreversible damage like cohesive zone model. In [1] a traction separation law for the delamination of laminates is introduced by Alfano and Crisfield and Gasser and Holzapfel [43] applied a transversely isotropic damage traction separation law for the modeling of dissection of biological tissues.

The introduction of strong discontinuities and cohesive zones in the framework of finite elements was treated with different methods in recent years. The main topic is the description of evolving discontinuities independent of the underlying finite element mesh. One recently developed approach is the extended Finite Element Method (XFEM), where the continuous displacement field is enriched by an additional potentially discontinuous displacement field. This allows to include strong discontinuities within finite elements. The XFEM was applied for linear elastic fracture problems in [14] and [87]. Applications of the method to the geometrically nonlinear setting can be found in the works of Wells et al. [131], Gasser and Holzapfel [43], Larsson and Fagerström [66] and Areias and Belytschko [2].

Different approaches with additional degrees of freedom on the element level can be summarized as the method with embedded discontinuities. These methods are based on the class of mixed Enhanced Assumed Strains (EAS) methods, proposed by Simo et al. [115]. Incompatible finite element methods for the modeling of failure based on this ideas have been introduced in the geometrically nonlinear regime for example by Armero and Garikipati [5], Larsson et al. [68], Oliver et al. [97], [98] and Gasser and Holzapfel [43]. In the present chapter a different approach is proposed. The method involving the discontinuous elements, which were introduced by Hansbo and Hansbo in [46] and used in chapter 3, is extended to finite strains. The elements which exhibit a discontinuity are doubled, which allows for the independent approximation of both continuous parts. Thereby only the standard basis functions are used and set to zero on one side of the discontinuity surface or on the other side. The approach shows similarities to the XFEM and leads eventually to a reparametrization of the resulting equations. But in contrast to the XFEM the enrichment at the interface is strictly local in the sense that no additional transition elements are required, compare section 3.5.1.

The introduction of the discontinuous elements allows for the simulation of propagating discontinuities, whereby the path of the discontinuity is independent of the finite element mesh. The method is implemented for two and three dimensional problems. In the following section the kinematic relations are introduced, first for the continuous case and then including a strong discontinuity. Afterwards the variational formulation is derived. The weak form is given in the material and the spatial configuration. A consistent linearization of the weak form is presented, whereby attention is paid especially to the linearization of the cohesive traction. In the next section the constitutive equations for the hyperelastic material behavior of the bulk and the damage type softening along the discontinuity surface are specified. Afterwards the discretization of the weak form is introduced and details about the integration of the discontinuous elements, the crack propagation and the algorithmic implementation are given. In the last sections numerical examples for two and three dimensional crack propagation are presented and the chapter is closed with a summary.

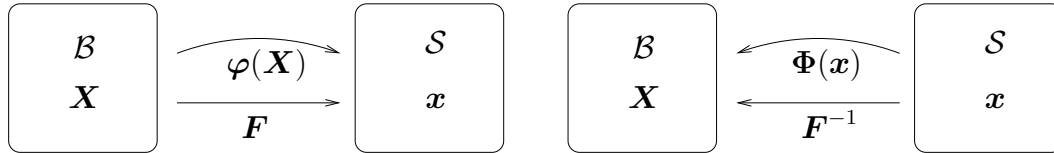


Figure 5.1.: Continuous Kinematics

5.2. Kinematics

In the following the kinematics for a continuous body in the geometrically nonlinear setting are recapitulated. Afterwards the kinematic relations are extended for a body crossed by a strong discontinuity.

5.2.1. Continuous kinematics

The basic kinematic variables which are necessary to describe the motion and deformation of a homogeneous body are introduced. In accordance with the continuum theory we consider a body as a composition of a set of particles. The placements of these particles at an initial time t_0 are specified by the position vectors \mathbf{X} and define the reference or material configuration \mathcal{B} of the body. At a certain time t the current position of the particles is described by the position vectors \mathbf{x} and defines the spatial or current configuration \mathcal{S} .

We define a nonlinear deformation map φ , which describes the motion of the body. The deformation map has to be unique, continuous and differentiable and maps the points \mathbf{X} in the material configuration to the places \mathbf{x} in the spatial configuration

$$\mathbf{x} = \varphi(\mathbf{X}, t) \quad \text{with} \quad \varphi : \mathcal{B} \rightarrow \mathcal{S}. \quad (5.2.1)$$

In the same manner the inverse motion can be introduced, which reverses the deformation map φ and thus maps the spatial to the reference configuration

$$\mathbf{X} = \Phi(\mathbf{x}, t) \quad \text{with} \quad \Phi : \mathcal{S} \rightarrow \mathcal{B}, \quad (5.2.2)$$

see figure 5.1. The deformation gradient \mathbf{F} , which is a fundamental kinematical quantity, is determined as the gradient of the deformation map with respect to the spatial coordinates

$$\mathbf{F} = \nabla_{\mathbf{X}} \varphi(\mathbf{X}, t) \quad \text{with} \quad \mathbf{F} : T\mathcal{B} \rightarrow T\mathcal{S}. \quad (5.2.3)$$

Therefore \mathbf{F} describes the linear tangent map from the material tangent space $T\mathcal{B}$ to the spatial tangent space $T\mathcal{S}$. The determinant of the deformation gradient is denoted Jacobian

$$J = \det(\mathbf{F}) > 0. \quad (5.2.4)$$

The condition $J > 0$ implies the physical meaning that the body can not penetrate itself during the deformation. To ensure the existence of the inverse deformation gradient, \mathbf{F} must not be singular, i. e. the Jacobian is not equal zero. The inverse deformation gradient is defined by means of the inverse deformation map as

$$\mathbf{F}^{-1} = \nabla_{\mathbf{x}} \Phi(\mathbf{x}, t) \quad \text{with} \quad \mathbf{F}^{-1} : TS \rightarrow TB. \quad (5.2.5)$$

The deformation gradient presents a linear tangent map of a line element in the material configuration $d\mathbf{X} \in TB$ to a line element in the spatial configuration $d\mathbf{x} \in TS$

$$d\mathbf{x} = \mathbf{F} \cdot d\mathbf{X}. \quad (5.2.6)$$

Furthermore the deformation gradient can be utilized for the transformation of area and volume elements. The transformation of area elements is described by Nanson's formula

$$d\mathbf{a} = J \mathbf{F}^{-t} \cdot d\mathbf{A} = \text{cof}(\mathbf{F}) \cdot d\mathbf{A}, \quad (5.2.7)$$

whereby the cofactor of \mathbf{F} denotes the product of the Jacobian and the transposed inverse deformation gradient. The orientation of the area elements is specified by their normals

$$d\mathbf{a} = \mathbf{n} da \quad \text{and} \quad d\mathbf{A} = \mathbf{N} dA. \quad (5.2.8)$$

An infinitesimal volume element is transformed by means of the Jacobian

$$dv = J dV. \quad (5.2.9)$$

To describe the deformation of the body typical strain measures are introduced, namely the right and left Cauchy-Green strain tensors \mathbf{C} and \mathbf{b}

$$\mathbf{C} = \mathbf{F}^t \cdot \mathbf{F} \quad \mathbf{b} = \mathbf{F} \cdot \mathbf{F}^t, \quad (5.2.10)$$

which are symmetric and positive definite. Since the deformation gradient \mathbf{F} can be decomposed into pure stretch and pure rotation, $\mathbf{F} = \mathbf{R} \cdot \mathbf{U}$ with $\mathbf{R}^t \cdot \mathbf{R} = \mathbf{I}$, it is apparent that the left and right Cauchy-Green tensors contain no rotational contributions. Hence a rigid body rotation is characterized by $\mathbf{F} = \mathbf{R}$ and $\mathbf{C} = \mathbf{I}$.

As a further strain measure the change in the squared length of a line element is defined, which leads to the specification of the Green-Lagrange strain tensor \mathbf{E} and the Euler-Almansi strain tensor \mathbf{e}

$$\mathbf{E} = \frac{1}{2} [\mathbf{F} \cdot \mathbf{F}^t - \mathbf{I}] \quad \mathbf{e} = \frac{1}{2} [\mathbf{I} - \mathbf{F}^{-t} \cdot \mathbf{F}^{-1}]. \quad (5.2.11)$$

Note that both strain measures are symmetric and vanish in the case that only rigid body motions are present, i. e. $\mathbf{E} = \mathbf{0}$ if $\mathbf{C} = \mathbf{I}$.

The introduced vector- and tensor-valued quantities are defined in the material or the

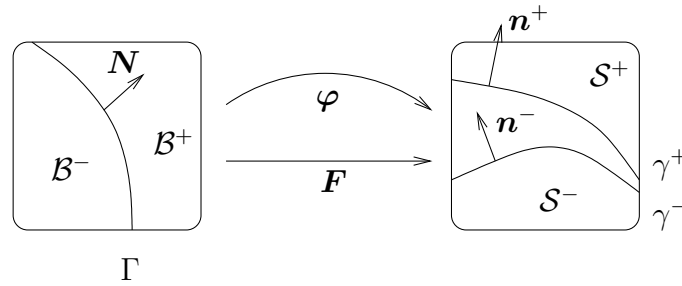


Figure 5.2.: Strong discontinuity kinematics

spatial configuration, or can be associated with both configurations, as e. g. the deformation gradient. The transformation from the material to the spatial configuration and vice versa are denoted by push-forward and pull-back operations. Thereby a multiplication of the considered quantity with \mathbf{F} , \mathbf{F}^t , \mathbf{F}^{-1} or \mathbf{F}^{-t} is accomplished, whereby the particular procedure depends on the character of this quantity. A short overview of several transformations can be found in [56], a more detailed description is given in [77].

5.2.2. Strong discontinuity kinematics

Now we refrain from the assumption that the deformation map is continuous in the whole body and instead allow for the development of a strong discontinuity along certain internal surfaces. One can imagine different situations where the usual assumption of continuity of the deformation map is not valid anymore. If we consider a body with a macroscopic crack, the opening of the crack can be described by means of a strong discontinuity, i. e. a jump in the deformation map. Due to this discontinuity it is possible that two points which are on each other in the reference configuration are mapped to different positions in the spatial configuration, when the two crack surfaces are separated. Physical phenomena which imply large strain gradients, like localization, can also be described by means of a strong discontinuity, see for example [69], [84], [119].

We assume that the body \mathcal{B} is divided by the internal discontinuity surface Γ into the referential subdomains \mathcal{B}^+ and \mathcal{B}^- , as pictured in figure 5.2. We consider now a non-linear, discontinuous deformation map φ , which carries the material configuration into the spatial one. The points \mathbf{X}^+ located in \mathcal{B}^+ are mapped to the points \mathbf{x}^+ in \mathcal{S}^+ and accordingly for the points \mathbf{X}^- . Consequently a point $\bar{\mathbf{X}}$, located on the discontinuity surface Γ in the material configuration, is mapped onto two points $\bar{\mathbf{x}}^+$ and $\bar{\mathbf{x}}^-$ in the spatial configuration, due to the discontinuous character of the deformation map. Therefore we obtain two discontinuity surfaces in the spatial configuration, denoted with γ^+ and γ^- . To characterize the discontinuity surface we introduce its normal vector in the material configuration \mathbf{N} , pointing from \mathcal{B}^- to \mathcal{B}^+ . The two different spatial normal vectors are denoted with \mathbf{n}^+ and \mathbf{n}^- and oriented as given in figure 5.2.

The deformation map is continuous in both parts of the body but discontinuous along Γ and can therefore be expressed by two independent continuous parts

$$\boldsymbol{\varphi}(\mathbf{X}) = \begin{cases} \boldsymbol{\varphi}^+(\mathbf{X}) & \text{with } \boldsymbol{\varphi}^+ : \mathcal{B}^+ \rightarrow \mathcal{S}^+ \\ \boldsymbol{\varphi}^-(\mathbf{X}) & \text{with } \boldsymbol{\varphi}^- : \mathcal{B}^- \rightarrow \mathcal{S}^-. \end{cases} \quad (5.2.12)$$

Then the jump in the deformation map can be defined as the difference of the maps at the discontinuity surface

$$[[\boldsymbol{\varphi}]] = \boldsymbol{\varphi}|_{\Gamma}^+ - \boldsymbol{\varphi}|_{\Gamma}^-. \quad (5.2.13)$$

As a consequence of the discontinuous deformation map, all related kinematic quantities, which were introduced in subsection 5.2.1, are defined separately for the two subdomains. The deformation gradient and the Jacobian are for example given as

$$\mathbf{F} = \begin{cases} \mathbf{F}^+ = \nabla_{\mathbf{X}} \boldsymbol{\varphi}^+ \\ \mathbf{F}^- = \nabla_{\mathbf{X}} \boldsymbol{\varphi}^- \end{cases} \quad \text{and} \quad J = \begin{cases} J^+ = \det(\mathbf{F}^+) \\ J^- = \det(\mathbf{F}^-) \end{cases}. \quad (5.2.14)$$

Note that in this way the deformation gradient is not defined along the discontinuity surface itself.

Remark 5.2.1 *The strong discontinuity kinematics can as well be described by means of the Heaviside function to avoid the disjoint definitions for each part of the body. The Heaviside function is defined as*

$$\mathcal{H}_{\Gamma}(\mathbf{X}) = \begin{cases} 1 & \text{in } \mathcal{B}^+ \\ \frac{1}{2} & \text{on } \Gamma \\ 0 & \text{in } \mathcal{B}^-. \end{cases} \quad (5.2.15)$$

If we want to retain the definitions of $\boldsymbol{\varphi}^+$ and $\boldsymbol{\varphi}^-$ we obtain

$$\boldsymbol{\varphi}(\mathbf{X}) = \mathcal{H}_{\Gamma}(\mathbf{X})\boldsymbol{\varphi}^+(\mathbf{X}) + [1 - \mathcal{H}_{\Gamma}(\mathbf{X})]\boldsymbol{\varphi}^-(\mathbf{X}), \quad (5.2.16)$$

The deformation gradient is then obtained as

$$\mathbf{F} = \delta_{\Gamma} \boldsymbol{\varphi}^+ \otimes \mathbf{N} + \mathcal{H}_{\Gamma} \mathbf{F}^+ - \delta_{\Gamma} \boldsymbol{\varphi}^- \otimes \mathbf{N} + [1 - \mathcal{H}_{\Gamma}] \mathbf{F}^-, \quad (5.2.17)$$

which can be summarized in a more common way as

$$\mathbf{F} = \underbrace{\mathcal{H}_{\Gamma} \mathbf{F}^+ + [1 - \mathcal{H}_{\Gamma}] \mathbf{F}^-}_{\mathbf{F}^b} + \underbrace{\delta_{\Gamma} [[\boldsymbol{\varphi}]] \otimes \mathbf{N}}_{\mathbf{F}^u}. \quad (5.2.18)$$

Thus the deformation gradient consists of a bounded part \mathbf{F}^b , defined by the deformation gradients of the continuous fields $\boldsymbol{\varphi}^+$ and $\boldsymbol{\varphi}^-$ and an unbounded part \mathbf{F}^u due to the

discontinuity. The unbounded term results from the spatial derivative of the Heaviside function. This is given in terms of the Dirac-delta function δ_Γ

$$\nabla_{\mathbf{X}} \mathcal{H}_\Gamma(\mathbf{X}) = \delta_\Gamma \mathbf{N}, \quad (5.2.19)$$

whereby δ_Γ has the properties

$$\delta_\Gamma(\mathbf{X}) = \begin{cases} \infty & \text{on } \Gamma \\ 0 & \text{else} \end{cases} \quad \text{with} \quad \int_{\mathcal{B}} \delta_\Gamma(\mathbf{X}) f(\mathbf{X}) dV = \int_\Gamma f(\mathbf{X}) dA. \quad (5.2.20)$$

5.2.3. Definition of the fictitious discontinuity surface

Due to the discontinuous deformation map φ , the unique discontinuity surface Γ in the material configuration is mapped onto the surfaces γ^+ and γ^- in the spatial configuration. In several works concerning strong discontinuities in the geometrically nonlinear setting a simplifying assumption for the jump term is made. For example in the contributions by Armero and Garikipati [5], Steinmann and Betsch [121] and Mosler [89], the jump is assumed to be spatially constant. That results in the relation $\nabla_{\mathbf{X}} \llbracket \varphi \rrbracket = \mathbf{0}$, which leads to an incompatibility. Since the jump is spatially constant the two discontinuity surfaces γ^+ and γ^- remain parallel, at least locally, and a unique normal vector to the internal surfaces is obtained.

In the present work we abolish the restriction on the jump term and allow for a spatially varying jump with $\nabla_{\mathbf{X}} \llbracket \varphi \rrbracket \neq \mathbf{0}$. However, since we assume that tractions can be transmitted along the internal discontinuity, we require a unique normal vector in order to define a traction separation relation. It seems to be a reasonable choice to follow [101]

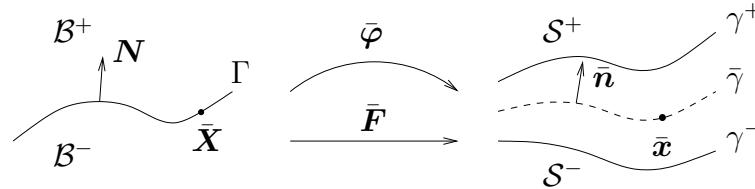


Figure 5.3.: Centered fictitious discontinuity surface in the spatial configuration

and [131] and define a centered discontinuity surface $\bar{\gamma}$, compare figure 5.3.

The averaged deformation map $\bar{\varphi}$ is introduced, which maps a point $\bar{\mathbf{X}}$, located on Γ , to the point $\bar{\mathbf{x}}$ on the center surface $\bar{\gamma}$, whereby $\bar{\mathbf{x}}$ can be identified as

$$\bar{\mathbf{x}} = \frac{1}{2} [\mathbf{x}^+ + \mathbf{x}^-]. \quad (5.2.21)$$

The associated deformation map turns out to be the average of the deformation maps φ^+ and φ^-

$$\bar{\varphi} = \frac{1}{2} [\varphi_{|\Gamma}^+ + \varphi_{|\Gamma}^-] \quad \text{with} \quad \bar{\varphi} : \Gamma \rightarrow \bar{\gamma} \quad (5.2.22)$$

and the related deformation gradient results as

$$\bar{\mathbf{F}} = \frac{1}{2}[\mathbf{F}_{|r}^+ + \mathbf{F}_{|r}^-]. \quad (5.2.23)$$

This averaged deformation gradient is only defined on the centered discontinuity surface, its determinant is denoted by $\bar{J} = \det(\bar{\mathbf{F}})$. The normal vector $\bar{\mathbf{n}}$, associated to $\bar{\gamma}$ and pointing from γ^- to γ^+ , can be calculated from Nanson's formula (5.2.7) as

$$\bar{\mathbf{n}} d\bar{a} = \bar{J} \bar{\mathbf{F}}^{-t} \cdot \mathbf{N} dA = \text{cof}(\bar{\mathbf{F}}) \cdot \mathbf{N} dA, \quad (5.2.24)$$

applying the average deformation gradient and its determinant.

Remark 5.2.2 *If we look at the definition of the bounded part of the discontinuous deformation gradient in (5.2.18) and evaluate the Heaviside function at Γ*

$$\bar{\mathbf{F}} = \frac{1}{2}\mathbf{F}^+ + [1 - \frac{1}{2}]\mathbf{F}^- = \frac{1}{2}[\mathbf{F}^+ + \mathbf{F}^-] \quad (5.2.25)$$

the average deformation gradient is also obtained.

In contrast to the above introduced centered discontinuity surface, obtained by the averaged deformation map, another definition of the discontinuity surface is imaginable. Instead of starting with the definition of the position of a point located on $\bar{\gamma}$, the fictitious discontinuity surface is directly identified via the averaged normal vectors, weighted with the incremental area measures, which leads to

$$\bar{\mathbf{n}} d\bar{a} = \frac{1}{2}[\mathbf{n}^+ da^+ + \mathbf{n}^- da^-] = \{\mathbf{n} da\}. \quad (5.2.26)$$

The particular spatial normal vectors are related to the material ones by Nanson's formula and therefore we obtain

$$\bar{\mathbf{n}} d\bar{a} = \{J \mathbf{F}^{-t}\} \cdot \mathbf{N} dA = \{\text{cof}(\mathbf{F})\} \cdot \mathbf{N} dA. \quad (5.2.27)$$

One can state that by means of this new definition an averaged discontinuity surface is introduced, whereby the averaging takes place with respect to the area and the orientation of the two spatial discontinuity surfaces.

If one compares equations (5.2.24) and (5.2.27), the approaches seem to be equivalent if the cofactor of the average deformation gradient $\bar{\mathbf{F}}$ is the same as the average of the cofactors of the deformation gradients \mathbf{F}^+ and \mathbf{F}^- . It can be shown that the two approaches indeed coincide for two dimensional problems, where the discontinuity surface reduces to a discontinuity line. But in the general three dimensional case arise differences.

However, if we consider cohesive cracks the definition of the fictitious discontinuity surface does not draw much of a difference, since the cohesive tractions are only transmitted in the process zone, where the opening of the crack surfaces is small. When the jump term increases, such that the definition of the fictitious discontinuity surface would have an influence, the tractions eventually vanish. Therefore the variation of the two approaches will be negligible. Since the first one leads to a simpler derivation of the governing equations it is used in the following.

5.3. Variational formulation

5.3.1. Strong form of the boundary value problem

We recapitulate the boundary value problem of geometrically nonlinear continuum mechanics in the strong form and formulated in the reference configuration \mathcal{B} . The boundary $\partial\mathcal{B}$ of the body \mathcal{B} with the material outward normal vector \mathbf{N}_e is divided into disjoint parts $\partial\mathcal{B} = \partial\mathcal{B}_x \cup \partial\mathcal{B}_t$ with $\partial\mathcal{B}_x \cap \partial\mathcal{B}_t = \emptyset$, where either Dirichlet or Neumann boundary conditions are prescribed. To simplify matters we assume that there are no body forces acting. The strong form of the boundary value problem is then given by the balance of linear momentum and the boundary conditions in terms of the prescribed Piola tractions \mathbf{T}^p and the prescribed deformation \mathbf{x}^p

$$\begin{aligned} -\text{Div } \mathbf{P} &= \mathbf{0} && \text{in } \mathcal{B}^+ \cup \mathcal{B}^- \\ \mathbf{x} &= \mathbf{x}^p && \text{on } \partial\mathcal{B}_x \\ \mathbf{P} \cdot \mathbf{N}_e &= \mathbf{T}^p && \text{on } \partial\mathcal{B}_t. \end{aligned} \quad (5.3.1)$$

The Piola stress tensor is denoted with \mathbf{P} . We assume that cohesive tractions, denoted with $\bar{\mathbf{T}}$ in the material configuration, are transmitted along the discontinuity surface. This leads to an additional equilibrium condition

$$\mathbf{P}^+ \cdot \mathbf{N} = \mathbf{P}^- \cdot \mathbf{N} = \bar{\mathbf{T}} \quad \text{on } \Gamma \quad (5.3.2)$$

at the internal boundary. The cohesive tractions will be constitutively prescribed.

5.3.2. Weak formulation in material configuration

As a prerequisite for a finite element formulation the nonlinear boundary value problem has to be reformulated in a weak form. Thereby an additional contribution to the virtual work expression has to be considered since the cohesive tractions are included. The balance of linear momentum is weighted with a test function $\delta\varphi$ and after integration by parts we obtain

$$\int_{\mathcal{B}^+ \cup \mathcal{B}^-} \delta\mathbf{F} : \mathbf{P} \, dV + \int_{\Gamma^+} \delta\varphi^+ \cdot \mathbf{P}^+ \cdot \mathbf{N} \, dA - \int_{\Gamma^-} \delta\varphi^- \cdot \mathbf{P}^- \cdot \mathbf{N} \, dA = \int_{\partial\mathcal{B}_t} \delta\varphi \cdot \mathbf{T}^p \, dA. \quad (5.3.3)$$

The two parts of the body are considered separately at first, which leads to the additional terms along the two sides of the discontinuity surface, Γ^+ and Γ^- . The different signs result from the definition of the normal vector \mathbf{N} , which points from \mathcal{B}^- to \mathcal{B}^+ . The boundary term can be summarized by means of a jump term

$$\int_{\Gamma^+} \delta\varphi^+ \cdot \mathbf{P}^+ \cdot \mathbf{N} \, dA - \int_{\Gamma^-} \delta\varphi^- \cdot \mathbf{P}^- \cdot \mathbf{N} \, dA = \int_{\Gamma} [\![\delta\varphi \cdot \mathbf{P}]\!] \cdot \mathbf{N} \, dA \quad (5.3.4)$$

and rewritten by the relation for the jump of a product (A.3.2) as

$$\int_{\Gamma} [[\delta\boldsymbol{\varphi} \cdot \mathbf{P}]] \cdot \mathbf{N} \, dA = \int_{\Gamma} [[\delta\boldsymbol{\varphi}]] \cdot \{\mathbf{P}\} \cdot \mathbf{N} + \{\delta\boldsymbol{\varphi}\} \cdot [[\mathbf{P}]] \cdot \mathbf{N} \, dA. \quad (5.3.5)$$

We take into account traction continuity along Γ , that means $[[\mathbf{P}]] \cdot \mathbf{N} = \mathbf{0}$, and obtain the resulting weak formulation in the reference configuration

$$\int_{\mathcal{B}^+ \cup \mathcal{B}^-} \delta \mathbf{F} : \mathbf{P} \, dV + \int_{\Gamma} [[\delta\boldsymbol{\varphi}]] \cdot \bar{\mathbf{T}} \, dA = \int_{\partial \mathcal{B}_t} \delta\boldsymbol{\varphi} \cdot \mathbf{T}^p \, dA. \quad (5.3.6)$$

Remark 5.3.1 *The variational formulation can also be obtained by the introduction of the discontinuous kinematic quantities in the standard weak formulation*

$$\int_{\mathcal{B}} \delta \mathbf{F} : \mathbf{P} \, dV = \int_{\partial \mathcal{B}_t} \delta\boldsymbol{\varphi} \cdot \mathbf{T}^p \, dA. \quad (5.3.7)$$

The variation of the discontinuous deformation gradient, expressed with the Heaviside function, is calculated from equation (5.2.18)

$$\delta \mathbf{F} = \mathcal{H}_{\Gamma} \delta \mathbf{F}^+ + [1 - \mathcal{H}_{\Gamma}] \delta \mathbf{F}^- + \delta_{\Gamma} [[\delta\boldsymbol{\varphi}]] \otimes \mathbf{N} \quad (5.3.8)$$

and inserted into the weak form 5.3.7

$$\begin{aligned} \int_{\mathcal{B}^+ \cup \mathcal{B}^-} [\mathcal{H}_{\Gamma} \delta \mathbf{F}^+ + [1 - \mathcal{H}_{\Gamma}] \delta \mathbf{F}^- + \delta_{\Gamma} [[\delta\boldsymbol{\varphi}]] \otimes \mathbf{N}] : \mathbf{P} \, dV &= \int_{\partial \mathcal{B}_t} \delta\boldsymbol{\varphi} \cdot \mathbf{T}^p \, dA \\ \Rightarrow \int_{\mathcal{B}^+ \cup \mathcal{B}^-} \delta \mathbf{F} : \mathbf{P} \, dV + \int_{\Gamma} [[\delta\boldsymbol{\varphi}]] \cdot \bar{\mathbf{T}} \, dA &= \int_{\partial \mathcal{B}_t} \delta\boldsymbol{\varphi} \cdot \mathbf{T}^p \, dA, \end{aligned} \quad (5.3.9)$$

whereby the equilibrium condition $\bar{\mathbf{T}} = \mathbf{P} \cdot \mathbf{N}$ is adopted. Naturally the same weak formulation is obtained.

5.3.3. Weak formulation in spatial configuration

To express the weak form of the governing equations in terms of the Cauchy stresses and tractions, equation (5.3.6) is pushed forward to the current configuration. To carry out the push forward of the particular terms the definition of the fictitious discontinuity surface and the associated averaged deformation quantities have to be considered.

In order to accomplish the push forward of the weak form (5.3.6) we replace the Piola stress tensor by the Cauchy stress tensor $\boldsymbol{\sigma}$ according to

$$\mathbf{P} = J \boldsymbol{\sigma} \cdot \mathbf{F}^{-t} \quad (5.3.10)$$

and apply the relation $\delta \mathbf{F} = \nabla_{\mathbf{x}} \delta\boldsymbol{\varphi} \cdot \mathbf{F}$. Since the deformation map is composed of two continuous functions this procedure can be accomplished for both parts of the body.

Introducing the spatial volume element $dv = J dV$ and the spatial cohesive traction vector $\bar{\mathbf{t}} = \bar{\mathbf{T}} dA/da$ results in the weak formulation in the spatial configuration

$$\int_{S^+ \cup S^-} \nabla_{\mathbf{x}} \delta \varphi : \boldsymbol{\sigma} dv + \int_{\bar{\gamma}} [[\delta \varphi]] \cdot \bar{\mathbf{t}} da = \int_{\partial \mathcal{S}_t} \delta \varphi \cdot \mathbf{t}^p da. \quad (5.3.11)$$

The push forward of the cohesive traction vector results from the push forward of the Cauchy stress tensor with the averaged deformation gradient and Nanson's formula

$$\bar{\mathbf{T}} dA = \mathbf{P} \cdot \mathbf{N} dA = \bar{J} \boldsymbol{\sigma} \cdot \bar{\mathbf{F}}^{-t} \cdot \mathbf{N} dA = \bar{\boldsymbol{\sigma}} \cdot \bar{\mathbf{n}} da = \bar{\mathbf{t}} da \quad (5.3.12)$$

and reveals the equilibrium condition on the discontinuity surface in the spatial configuration $\boldsymbol{\sigma} \cdot \bar{\mathbf{n}} = \bar{\mathbf{t}}$. The push forward of the prescribed tractions on the Neumann boundary is accomplished in a similar manner.

If we introduce the following expressions for the particular parts of the virtual work

$$\delta W_{int} = \int_{S^+ \cup S^-} \nabla_{\mathbf{x}} \delta \varphi : \boldsymbol{\sigma} dv, \quad \delta W_{coh} = \int_{\bar{\gamma}} [[\delta \varphi]] \cdot \bar{\mathbf{t}} da, \quad \delta W_{ext} = \int_{\partial \mathcal{S}_t} \delta \varphi \cdot \mathbf{t}^p da \quad (5.3.13)$$

we can rewrite equation (5.3.11) as

$$\delta W_{int} + \delta W_{coh} = \delta W_{ext}. \quad (5.3.14)$$

5.3.4. Linearization

In this section we consider the linearization of the weak governing equation. Thereby linearizations are denoted by a prefixed Δ and the partial derivative of \ast with respect to \bullet is denoted by $\partial(\ast)/\partial(\bullet)$. The linearization of the internal virtual work δW_{int} consists of two contributions

$$\Delta \delta W_{int} = \int_{S^+ \cup S^-} \boldsymbol{\sigma} : [\nabla_{\mathbf{x}}^t \Delta \varphi \cdot \nabla_{\mathbf{x}} \delta \varphi] dv + \int_{S^+ \cup S^-} \nabla_{\mathbf{x}} \delta \varphi : \mathbf{e} : \nabla_{\mathbf{x}} \Delta \varphi dv, \quad (5.3.15)$$

a material one due to the dependence of the stress tensor on the strain and a geometric one due the dependence of the strain on the deformation. Thereby \mathbf{e} denotes the elastic tangent moduli. In what follows we shall assume that δW_{ext} be independent of the deformation such that $\Delta \delta W_{ext} = 0$. What remains is the linearization of the additional contribution to the virtual work δW_{coh} . Therefore we follow the work of Gasser and Holzapfel [42], who derived the linearization of the cohesive traction vector for different enhanced assumed strain (EAS) approaches. The linearization of $\Delta \delta W_{coh}$ is here accomplished for traction separation laws where the traction vector depends on the jump and on the normal vector of the discontinuity surface. In this case the linearization results in three parts: a material one, due to the dependence of the traction vector on the jump in the deformation map, and two geometrical ones, due to the change of the normal vector

and the change of the area of the fictitious discontinuity surface, respectively. In case that an isotropic traction separation relation for the Cauchy traction $\bar{\mathbf{t}}$ or in the material setting for the Piola traction $\bar{\mathbf{T}}$ is applied, the linearization becomes simpler. Its discrete version is given in section 5.5.3.

In the general case the linearization of $\delta W_{coh}([\varphi], \bar{\mathbf{n}})$ reads

$$\Delta \delta W_{coh} = \int_{\bar{\gamma}} [[\delta \varphi]] \cdot \frac{\partial \bar{\mathbf{t}}}{\partial [[\varphi]]} \cdot [[\Delta \varphi]] da + \int_{\bar{\gamma}} [[\delta \varphi]] \cdot \frac{\partial \bar{\mathbf{t}}}{\partial \bar{\mathbf{n}}} \cdot \Delta \bar{\mathbf{n}} da + \int_{\bar{\gamma}} [[\delta \varphi]] \cdot \bar{\mathbf{t}} \Delta da. \quad (5.3.16)$$

The Cauchy traction $\bar{\mathbf{t}}$ depends on the jump in the deformation map $[[\varphi]]$ and when a different material behavior for the opening and sliding direction is assumed also on the change in the direction of the unit normal vector $\bar{\mathbf{n}}$. In the geometrically linear setting this additional dependence on the normal vector is not included. The derivation of $\partial \bar{\mathbf{t}} / \partial [[\varphi]]$ depends on the chosen cohesive constitutive law. We denote the derivative of the tractions with respect to the jump with \mathbf{T}_φ and the first term of equation (5.3.16) results in

$$\int_{\bar{\gamma}} [[\delta \varphi]] \cdot \frac{\partial \bar{\mathbf{t}}}{\partial [[\varphi]]} \cdot [[\Delta \varphi]] da = \int_{\bar{\gamma}} [[\delta \varphi]] \cdot \mathbf{T}_\varphi \cdot [[\Delta \varphi]] da, \quad (5.3.17)$$

The tangent operator \mathbf{T}_φ is specified for different cohesive traction separation relations in section 5.4.2.

The second term of equation (5.3.16) contains the directional derivative of the traction $\bar{\mathbf{t}}$ with respect to the unit normal vector $\bar{\mathbf{n}}$, which vanishes for the isotropic case. In the same manner as above, we introduce the general tangent operator $\mathbf{T}_n = \partial \bar{\mathbf{t}} / \partial \bar{\mathbf{n}}$. To complete the specification of the second term of equation (5.3.16), the linearization of the normal vector $\Delta \bar{\mathbf{n}}$, has to be calculated. The spatial unit normal of the fictitious discontinuity surface $\bar{\mathbf{n}}$ can be described in terms of the push forward of the reference unit normal scaled by its current length

$$\bar{\mathbf{n}} = \frac{\bar{\mathbf{n}}^*}{|\bar{\mathbf{n}}^*|} \quad \bar{\mathbf{n}}^* = \mathbf{N} \cdot \bar{\mathbf{F}}^{-1} \quad |\bar{\mathbf{n}}^*| = [\mathbf{N} \cdot \bar{\mathbf{C}}^{-1} \cdot \mathbf{N}]^{1/2}. \quad (5.3.18)$$

Firstly we will derive the directional derivative of $\bar{\mathbf{n}}$ with respect to $\bar{\mathbf{F}}^{-1}$

$$\frac{\partial \bar{\mathbf{n}}}{\partial \bar{\mathbf{F}}^{-1}} = \bar{\mathbf{n}} \cdot \bar{\mathbf{F}} \otimes \mathbf{I} - \bar{\mathbf{n}} \otimes \bar{\mathbf{n}} \cdot \bar{\mathbf{F}} \otimes \bar{\mathbf{n}} = \frac{1}{|\bar{\mathbf{n}}^*|} [\mathbf{N} \cdot \mathbf{I} \otimes \mathbf{I} - \bar{\mathbf{n}} \otimes \mathbf{N} \otimes \bar{\mathbf{n}}]. \quad (5.3.19)$$

This relation has to be completed by the linearization of the inverse deformation gradient $\partial \bar{\mathbf{F}}^{-1} / \partial \bar{\mathbf{F}} = -\bar{\mathbf{F}}^{-1} \bar{\otimes} \bar{\mathbf{F}}^{-t}$, whereby the non-standard dyadic product $\bar{\otimes}$ takes the following component-wise representation $\{\bullet \bar{\otimes} \circ\}_{ijkl} = \{\bullet\}_{ik} \otimes \{\circ\}_{jl}$, and thus

$$\frac{\partial \bar{\mathbf{n}}}{\partial \bar{\mathbf{F}}} = -\bar{\mathbf{n}} \cdot [\mathbf{I} \bar{\otimes} \bar{\mathbf{F}}^{-t}] + \bar{\mathbf{n}} \otimes \bar{\mathbf{n}} \otimes \bar{\mathbf{n}} \cdot \bar{\mathbf{F}}^{-t} =: \mathbf{G}. \quad (5.3.20)$$

Accordingly the linearization of the spatial unit normal can be expressed as

$$\Delta \bar{\mathbf{n}} = \mathbf{G} : \Delta \bar{\mathbf{F}}. \quad (5.3.21)$$

This leads to the summarized result of the linearization of the second term of equation (5.3.16)

$$\int_{\bar{\gamma}} [[\delta\boldsymbol{\varphi}] \cdot \mathbf{T}_n \cdot \Delta\bar{\mathbf{n}}] da = \int_{\bar{\gamma}} [[\delta\boldsymbol{\varphi}] \cdot \mathbf{T}_n \cdot \mathbf{G} : \Delta\bar{\mathbf{F}}] da. \quad (5.3.22)$$

To proceed with the linearization, we rewrite the third term by means of equation (5.3.16) by means of the area ratio $K = da/dA$

$$\int_{\text{ga}\bar{\mathbf{m}}\bar{\mathbf{m}}\bar{\mathbf{a}}} [[\delta\boldsymbol{\varphi}] \cdot \mathbf{t} \Delta da] = \int_{\bar{\gamma}} [[\delta\boldsymbol{\varphi}] \cdot \mathbf{t} \frac{1}{K} \Delta K] da, \quad (5.3.23)$$

whereby an expression for K can be found by applying Nanson's formula $K = \bar{J} \sqrt{\mathbf{N} \cdot \bar{\mathbf{C}}^{-1} \cdot \mathbf{N}}$. The directional derivative of K can then be calculated as

$$\Delta K = \frac{\partial K}{\partial \bar{J}} \frac{\partial \bar{J}}{\partial \bar{\mathbf{F}}} : \Delta\bar{\mathbf{F}} + \frac{\partial K}{\partial \bar{\mathbf{C}}} : \frac{\partial \bar{\mathbf{C}}}{\partial \bar{\mathbf{F}}} : \Delta\bar{\mathbf{F}}, \quad (5.3.24)$$

whereby the first part is given by

$$\frac{\partial K}{\partial \bar{J}} \frac{\partial \bar{J}}{\partial \bar{\mathbf{F}}} : \Delta\bar{\mathbf{F}} = \frac{K}{\bar{J}} \bar{J} \bar{\mathbf{F}}^{-t} : \Delta\bar{\mathbf{F}} = K \bar{\mathbf{F}}^{-t} : \Delta\bar{\mathbf{F}}. \quad (5.3.25)$$

The calculation of the second part of equation (5.3.24)

$$\frac{\partial K}{\partial \bar{\mathbf{C}}} = -\frac{\bar{J}^2}{2K} \mathbf{N} \cdot \bar{\mathbf{C}}^{-1} \otimes \bar{\mathbf{C}}^{-1} \cdot \mathbf{N} = -\frac{K}{2} \bar{\mathbf{n}} \cdot \bar{\mathbf{F}}^{-t} \otimes \bar{\mathbf{F}}^{-1} \cdot \bar{\mathbf{n}}. \quad (5.3.26)$$

in conjunction with $\frac{\partial \bar{\mathbf{C}}}{\partial \bar{\mathbf{F}}} : \Delta\bar{\mathbf{F}} = \Delta\bar{\mathbf{F}}^t \cdot \bar{\mathbf{F}} + \bar{\mathbf{F}}^t \cdot \Delta\bar{\mathbf{F}}$ results in the following expression

$$\frac{\partial K}{\partial \bar{\mathbf{F}}} : \Delta\bar{\mathbf{F}} = -K \bar{\mathbf{n}} \cdot \Delta\bar{\mathbf{F}} \cdot \bar{\mathbf{F}}^{-1} \cdot \bar{\mathbf{n}} \quad (5.3.27)$$

which finally leads, completed with the result in (5.3.25) to the linearization of K

$$\Delta K = K [\mathbf{I} - \bar{\mathbf{n}} \otimes \bar{\mathbf{n}}] \cdot \bar{\mathbf{F}}^{-t} : \Delta\bar{\mathbf{F}}. \quad (5.3.28)$$

and to the specification of the third term of equation (5.3.16)

$$\int_{\bar{\gamma}} [[\delta\boldsymbol{\varphi}] \cdot \mathbf{t} \Delta da] = \int_{\bar{\gamma}} [[\delta\boldsymbol{\varphi}] \cdot \mathbf{t} [\mathbf{I} - \bar{\mathbf{n}} \otimes \bar{\mathbf{n}}] \cdot \bar{\mathbf{F}}^{-t} : \Delta\bar{\mathbf{F}}] da. \quad (5.3.29)$$

To finish the linearization of δW_{coh} we specify the linearization of the jump in the deformation map $[[\Delta\boldsymbol{\varphi}]]$, which appears in equation (5.3.17), and the linearization of the averaged deformation gradient $\Delta\bar{\mathbf{F}}$, which can be found in (5.3.22) and (5.3.29). Therefore we recall the definitions of both terms, (5.2.13) and (5.2.23), and obtain

$$[[\Delta\boldsymbol{\varphi}]] = [\Delta\boldsymbol{\varphi}^+ - \Delta\boldsymbol{\varphi}^-] \quad (5.3.30)$$

$$\Delta\bar{\mathbf{F}} = \frac{1}{2} [\Delta\mathbf{F}^+ + \Delta\mathbf{F}^-] = \frac{1}{2} [\nabla_{\mathbf{X}} \Delta\boldsymbol{\varphi}^+ + \nabla_{\mathbf{X}} \Delta\boldsymbol{\varphi}^-],$$

which finally completes the linearization on δW_{coh} .

It is notable that the accomplished linearization is generally valid for different transversely isotrop traction separation laws, which are formulated in the Cauchy tractions. The tangent moduli \mathbf{T}_φ and \mathbf{T}_n have to be recomputed when introducing a different cohesive constitutive law.

5.4. Constitutive equations

In the following section the constitutive laws, which determine the material response, are specified. In general the constitutive equation defines the stress state at any point \mathbf{x} , depending on other field variables, e. g. the strain. In the present work the phenomenological approach is used, whereby the macroscopic behavior of a material is described without any information about the related microstructure.

We consider problems with a strong discontinuity and imply the existence of an additional cohesive traction vector at the discontinuity surface. In the literature two different procedures for the development of the traction separation relation can be found. Simo et al. [114], Armero and Garikipati [5] and Steinmann and Betsch [119], among others, derive the traction separation relation as the projection of the material behavior of the bulk material onto the discontinuity. This procedure is mainly applied for the modeling of strain localization within the plasticity or damage theory. Traction separation relations for multiplicative finite strain plasticity are derived in [5] and [121]. The projection of a continuum damage model onto the discontinuity is accomplished in [96] and [67].

In the present approach a different assumption is made. The traction separation relation is not associated to the constitutive relation for the Piola stress \mathbf{P} , that means that the material behavior of the interface is independent of the material behavior of the surrounding domain. This approach is also adopted by e. g. Miehe and Schröder [84] or Armero [4] for localization in elastoplastic solids and by Jirásek within the framework of the damage theory [61], [62]. This concept can be related to the cohesive crack concept, which is based on the work of Dugdale [34] and Barenblatt [10]. This approach does not presuppose a particular type of constitutive behavior in the bulk. Therefore it is possible to restrict all dissipative mechanisms to the traction separation law and assume elastic behavior in the bulk.

In the following two independent constitutive equations will be formulated, one for the bulk and one for the cohesive surface.

5.4.1. Hyperelasticity

The material behavior of the bulk is assumed to be hyperelastic, which is sufficient for many materials, sustaining large deformation. In the geometrically linear case the equa-

tions reduce to linear elasticity.

The existence of a free energy Ψ per unit reference volume is required, which is commonly called the strain energy function. In the case of perfectly elastic materials, which are considered here, the internal dissipation is equal to zero [126] and the definition of the Piola stress \mathbf{P} follows directly from the second law of thermodynamics as

$$\mathbf{P} = \frac{\partial \Psi(\mathbf{F})}{\partial \mathbf{F}}. \quad (5.4.1)$$

The symmetric Cauchy stress tensor can then be calculated by means of a push forward as

$$\boldsymbol{\sigma} = J^{-1} \frac{\partial \Psi(\mathbf{F})}{\partial \mathbf{F}} \cdot \mathbf{F}^t. \quad (5.4.2)$$

The strain energy function has to fulfill some physically motivated conditions. The normalization condition states that the strain energy function vanishes in the reference configuration $\Psi(\mathbf{I}) = 0$ and increases with deformation $\Psi(\mathbf{F}) \geq 0$. This leads to a stress-free reference configuration. Furthermore the growth condition implies that Ψ tends to infinity if the Jacobian comes close to zero or infinity. This has the physical interpretation that one needs infinite energy to compress or expand a body to zero or infinite volume.

We restrict ourselves to isotropic material behavior in the bulk, which means that the material response is the same for different directions of loading. Furthermore we assume that the material is compressible, therefore the volume can change during deformation and the only restriction to the Jacobian is $J > 0$ (instead of the restriction $J = 1$ in the incompressible case).

We choose a Neo-Hookean strain energy function, which is often used in the literature, e. g. [19]. The strain energy function is given by

$$\Psi = \frac{\mu}{2} [[\mathbf{F} \cdot \mathbf{F}^t] : \mathbf{I} - n^{dim}] - \mu \ln(J) + \frac{\lambda}{2} \ln^2(J), \quad (5.4.3)$$

whereby μ and λ are the Lamé parameters and n^{dim} denotes the dimension. Using equation (5.4.1), the derivative of the strain energy function with respect to the deformation gradient leads to the Piola stress

$$\mathbf{P} = [\lambda \ln(J) - \mu] \mathbf{F}^{-t} + \mu \mathbf{F}. \quad (5.4.4)$$

And the application of the push-forward operation (5.4.2)

$$\boldsymbol{\sigma} = J^{-1} [\lambda \ln(J) - \mu] \mathbf{I} + J^{-1} \mu \mathbf{b} \quad (5.4.5)$$

leads to the definition of the Cauchy stress.

5.4.2. Cohesive constitutive law

In the first part of this subsection a transversely isotropic traction separation relation for the Cauchy traction $\bar{\mathbf{t}}$ is postulated. To simplify matters the cohesive traction separation relation, which was introduced in section 3.4.2, is transferred to the geometrically nonlinear setting. In the second part of the subsection a thermomechanically consistent determination of a traction separation relation for the Piola tractions $\bar{\mathbf{T}}$ is derived.

The transversely isotropic cohesive constitutive law relates the traction vector $\bar{\mathbf{t}} = \boldsymbol{\sigma} \cdot \bar{\mathbf{n}}$ along the discontinuity surface with the jump in the deformation map $[[\boldsymbol{\varphi}]]$. We assume that softening phenomena occur along the discontinuity and that the cohesive behavior is different for opening and sliding. In the direction normal to the interface exponential softening is assumed and a constant stiffness is supposed in tangential direction. Therefore a cohesive constitutive law can be postulated as

$$\begin{aligned}\bar{\mathbf{t}}_n &= f_t \exp\left(-\frac{f_t}{G_f} [[\varphi_n]]\right) \bar{\mathbf{n}} \\ \bar{\mathbf{t}}_m &= d [[\boldsymbol{\varphi}_m]] \\ \bar{\mathbf{t}} &= \bar{\mathbf{t}}_n + \bar{\mathbf{t}}_m.\end{aligned}\tag{5.4.6}$$

The tensile strength is denoted by f_t , the fracture energy by G_f and the shear stiffness by d . The normal and tangential gaps in the deformation map can be obtained by

$$[[\boldsymbol{\varphi}_n]] = [[\varphi_n]] \bar{\mathbf{n}} \quad \text{with} \quad [[\varphi_n]] = [[\boldsymbol{\varphi}]] \cdot \bar{\mathbf{n}} \quad \text{and} \quad [[\boldsymbol{\varphi}_m]] = [[\boldsymbol{\varphi}]] - [[\varphi_n]] \bar{\mathbf{n}}.\tag{5.4.7}$$

Since this traction separation relation depends on the normal vector $\bar{\mathbf{n}}$ we need to specify the linearizations of $\bar{\mathbf{t}}$ with respect to $[[\boldsymbol{\varphi}]]$ and $\bar{\mathbf{n}}$. We can specify $\partial\bar{\mathbf{t}}/\partial[[\boldsymbol{\varphi}]]$ as

$$\frac{\partial\bar{\mathbf{t}}}{\partial[[\boldsymbol{\varphi}]]} = \frac{\partial\bar{\mathbf{t}}}{\partial[[\varphi_n]]} \cdot [\bar{\mathbf{n}} \otimes \bar{\mathbf{n}}] + \frac{\partial\bar{\mathbf{t}}}{\partial[[\boldsymbol{\varphi}_m]]} \cdot [\mathbf{I} - \bar{\mathbf{n}} \otimes \bar{\mathbf{n}}] =: \mathbf{T}_\varphi.\tag{5.4.8}$$

Considering the exponential softening law (5.4.6), the tangent moduli $\partial\bar{\mathbf{t}}/\partial[[\varphi_n]]$ and $\partial\bar{\mathbf{t}}/\partial[[\boldsymbol{\varphi}_m]]$ can be derived as

$$\frac{\partial\bar{\mathbf{t}}}{\partial[[\varphi_n]]} = -\frac{f_t^2}{G_f} \exp\left(-\frac{f_t}{G_f} [[\varphi_n]] \cdot \bar{\mathbf{n}}\right) \bar{\mathbf{n}} \otimes \bar{\mathbf{n}} \quad \text{and} \quad \frac{\partial\bar{\mathbf{t}}}{\partial[[\boldsymbol{\varphi}_m]]} = d \mathbf{I}.\tag{5.4.9}$$

To derive the linearization with respect to $\bar{\mathbf{n}}$ we decompose the derivative in a normal and a tangential attribution

$$\frac{\partial\bar{\mathbf{t}}}{\partial\bar{\mathbf{n}}} = \frac{\partial\bar{\mathbf{t}}}{\partial[[\varphi_n]]} \cdot [\bar{\mathbf{n}} \otimes [[\boldsymbol{\varphi}]] + [[[\boldsymbol{\varphi}] \cdot \bar{\mathbf{n}}] \mathbf{I}] - \frac{\partial\bar{\mathbf{t}}}{\partial[[\boldsymbol{\varphi}_m]]} \cdot [\bar{\mathbf{n}} \otimes [[\boldsymbol{\varphi}]] + [[[\boldsymbol{\varphi}] \cdot \bar{\mathbf{n}}] \mathbf{I}] =: \mathbf{T}_n.\tag{5.4.10}$$

Then we can introduce the already computed tangent moduli for the exponential softening law (5.4.9). This particular format of the cohesive constitutive law is chosen because of

its simplicity with respect to the implementation and adopted in most of the examples.

In the following a thermomechanically consistent traction separation relation is derived in terms of the Piola tractions $\bar{\mathbf{T}}$. The starting point is the definition of the deformation power of a body containing a cohesive surface. It extends the conventional deformation power identity by an additional term depending on the cohesive tractions [101]

$$\mathcal{P} = \int_{\mathcal{B}^+ \cup \mathcal{B}^-} \mathbf{P} : \dot{\mathbf{F}} dV + \int_{\Gamma} \bar{\mathbf{T}} \cdot \llbracket \dot{\boldsymbol{\varphi}} \rrbracket dA. \quad (5.4.11)$$

Obviously the Piola tractions $\bar{\mathbf{T}}$ and the jump in the deformation map $\llbracket \boldsymbol{\varphi} \rrbracket$ are work conjugated with respect to the undeformed volume. Therefore the opening displacements $\llbracket \boldsymbol{\varphi} \rrbracket$ act as a deformation measure, $\bar{\mathbf{T}}$ being the conjugated stress measure.

Remark 5.4.1 *The extended deformation power identity can also be obtained by the introduction of the material velocity gradient $\dot{\mathbf{F}}$, calculated by means of equation (5.2.18)*

$$\dot{\mathbf{F}} = \mathcal{H}_{\Gamma} \dot{\mathbf{F}}^+ + [1 - \mathcal{H}_{\Gamma}] \dot{\mathbf{F}}^- + \delta_{\Gamma} \llbracket \dot{\boldsymbol{\varphi}} \rrbracket \otimes \mathbf{N} \quad (5.4.12)$$

into the conventional deformation power identity

$$\begin{aligned} \int_{\mathcal{B}} \mathbf{P} : \dot{\mathbf{F}} dA &= \int_{\mathcal{B}^+ \cup \mathcal{B}^-} \mathbf{P} : \dot{\mathbf{F}} dV + \int_{\mathcal{B}} \delta_{\Gamma} \mathbf{P} \cdot \llbracket \dot{\boldsymbol{\varphi}} \rrbracket \otimes \mathbf{N} dV \\ &= \int_{\mathcal{B}^+ \cup \mathcal{B}^-} \mathbf{P} : \dot{\mathbf{F}} dV + \int_{\Gamma} \bar{\mathbf{T}} \cdot \llbracket \dot{\boldsymbol{\varphi}} \rrbracket dA. \end{aligned} \quad (5.4.13)$$

Expressing the deformation power in the spatial configuration, using the push forward of the Piola stress (5.4.2) and Nanson's formula (5.2.24), leads to

$$\mathcal{P} = \int_{\mathcal{B}^+ \cup \mathcal{B}^-} \boldsymbol{\sigma} : \mathbf{d} dv + \int_{\gamma} \bar{\mathbf{t}} \cdot \llbracket \dot{\boldsymbol{\varphi}} \rrbracket da, \quad (5.4.14)$$

in terms of the Cauchy stress tensor and the Cauchy traction vector. The rate of the deformation tensor \mathbf{d} denotes the symmetric part of the spatial velocity gradient $\mathbf{l} = \dot{\mathbf{F}} \cdot \mathbf{F}^{-1}$. The Cauchy traction vector $\bar{\mathbf{t}}$ and the jump in the deformation map $\llbracket \boldsymbol{\varphi} \rrbracket$ are therefore work conjugated with respect to the deformed volume. The deformation measure $\llbracket \boldsymbol{\varphi} \rrbracket$ vanishes identically if the body undergoes rigid body motions.

We consider isotropic cohesive material behavior. As a starting point we postulate the existence of a cohesive free energy density per unit undeformed area of the form

$$\bar{\Psi} = \bar{\Psi}(\llbracket \boldsymbol{\varphi} \rrbracket). \quad (5.4.15)$$

The time derivative of the cohesive potential is determined as

$$\dot{\bar{\Psi}} = \frac{\partial \bar{\Psi}}{\partial \llbracket \boldsymbol{\varphi} \rrbracket} \cdot \llbracket \dot{\boldsymbol{\varphi}} \rrbracket. \quad (5.4.16)$$

By recourse to Coleman and Noll's method and with the equations (5.4.11) and (5.4.16) the cohesive traction separation law takes the format

$$\bar{\mathbf{T}} = \frac{\partial \bar{\Psi}}{\partial \llbracket \boldsymbol{\varphi} \rrbracket}. \quad (5.4.17)$$

To specify the introduced cohesive material behavior we assume an exponential softening of the interface. The cohesive energy density is particularized as

$$\bar{\Psi}(\llbracket \boldsymbol{\varphi} \rrbracket) = \frac{\alpha}{\beta} [1 - \exp(-\beta \|\llbracket \boldsymbol{\varphi} \rrbracket\|)] \quad (5.4.18)$$

whereby α and β denote some scalar valued positive material parameters. The traction vector results from equation (5.4.17) as

$$\bar{\mathbf{T}} = \frac{\partial \bar{\Psi}}{\partial \llbracket \boldsymbol{\varphi} \rrbracket} = \alpha \exp(-\beta \|\llbracket \boldsymbol{\varphi} \rrbracket\|) \frac{\llbracket \boldsymbol{\varphi} \rrbracket}{\|\llbracket \boldsymbol{\varphi} \rrbracket\|} \quad (5.4.19)$$

whereby the traction vector has the same direction as the jump in the deformation map. The presented cohesive constitutive law is isotropic and therefore no additional dependence on the normal vector has to be regarded. The linearization of the traction vector is only composed of the tangent $\mathbf{T}_\varphi = \partial \bar{\mathbf{T}} / \partial \llbracket \boldsymbol{\varphi} \rrbracket$

$$\mathbf{T}_\varphi = -\alpha \beta \exp(-\beta \|\llbracket \boldsymbol{\varphi} \rrbracket\|) \boldsymbol{\nu} \otimes \boldsymbol{\nu} + \frac{\alpha}{\|\llbracket \boldsymbol{\varphi} \rrbracket\|} \exp(-\beta \|\llbracket \boldsymbol{\varphi} \rrbracket\|) [\mathbf{I} - \boldsymbol{\nu} \otimes \boldsymbol{\nu}], \quad (5.4.20)$$

with $\boldsymbol{\nu} = \llbracket \boldsymbol{\varphi} \rrbracket / \|\llbracket \boldsymbol{\varphi} \rrbracket\|$. In figure 5.4 the direction of the traction vector and the exponential softening is indicated. By means of the figure and equation (5.4.19) it can be verified that the material parameter α can be identified as the tensile strength and the ratio α/β as the fracture energy.

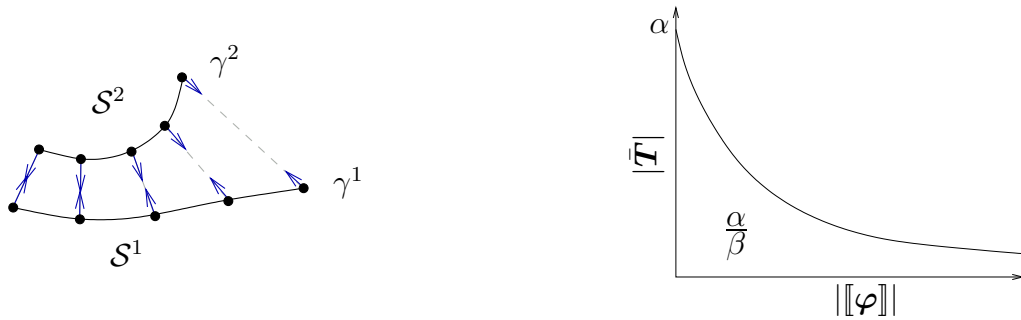


Figure 5.4.: Traction separation relation, exponential softening

Remark 5.4.2 *This cohesive constitutive law is especially useful for the adaptive introduction of cohesive zones within finite elements, since it belongs to the group of initially rigid cohesive laws. The jump is enforced to be zero until the tractions across the interface reach a critical value. The resulting infinite stiffness may lead to problems regarding the convergence behavior. This is circumvented by numerical perturbation of the initial opening displacement $\|\llbracket \boldsymbol{\varphi} \rrbracket\|$ with a small value.*

Remark 5.4.3 *In order to avoid penetration of the surfaces a penalty method is adopted. Therefore a high compressive force is applied if the normal jump $[[\boldsymbol{\varphi}]] \cdot \bar{\mathbf{n}}$ becomes negative. With this penalty constraint the isotropic formulation becomes anisotropic for $[[\boldsymbol{\varphi}]] \cdot \bar{\mathbf{n}} < 0$.*

In the previous part an isotropic traction separation relation was derived from a cohesive potential for the interface. If we refrain from the restriction of isotropic material behavior, an additional dependence of the traction vector on the normal vector $\bar{\mathbf{n}}$ to the discontinuity surface can be considered. This is an important difference between the geometrically linear and nonlinear case, since the normal vector depends on the deformation in the nonlinear setting. In several publications this transversely isotropic behavior is taken into account, e. g. in [101], [131], [43] and [82]. But due to this dependence of the traction vector on a certain direction, unsymmetric formulations are derived. This conflicts with the assumption that the traction separation law can be obtained from a cohesive potential. A variation of the normal vector at a constant jump must not entail a variation of the deformation power (5.4.11). But if we define a cohesive energy with an additional dependence on the normal vector exactly this is the case.

In the work of Steinmann and Häsner [120] material interfaces with their own free energy function are regarded. Thereby an additional dependence of the interface free energy on the surface Cauchy-Green deformation tensor is taken into account, which was also considered in [101]. The surface Cauchy-Green deformation tensor is given in terms of the surface gradient of the deformation map

$$\mathbf{C}_\Gamma = \nabla_\Gamma \bar{\boldsymbol{\varphi}}^t \cdot \nabla_\Gamma \bar{\boldsymbol{\varphi}}. \quad (5.4.21)$$

The conjugated quantity to the surface deformation is an interface stress field, which does not possess any normal parts. But the additional dependence of $\bar{\Psi}$ on \mathbf{C}_Γ does not describe the directional dependence of $\bar{\mathbf{t}}$. On the one hand, the surface Cauchy-Green deformation tensor can not describe the rotation of the normal vector, only the surface stretch, and on the other hand a stretch of the crack surfaces should not lead to a change of the cohesive tractions.

These comments lead to the conclusion that the determination of a traction separation law from a cohesive potential is restricted to isotropic formulations in the geometrically nonlinear setting. To clarify this conclusion, the Clausius-Duhem inequality for an anisotropic elastic traction separation law is derived. Let the cohesive energy depend on the jump $[[\boldsymbol{\varphi}]]$ and on the normal vector $\bar{\mathbf{n}}$

$$\bar{\Psi} = \bar{\Psi}([[\boldsymbol{\varphi}]], \bar{\mathbf{n}}). \quad (5.4.22)$$

Then the time derivative of the cohesive free energy implies contributions due to a variation of the normal vector

$$\dot{\bar{\Psi}} = \frac{\partial \bar{\Psi}}{\partial [[\boldsymbol{\varphi}]]} \cdot [[\dot{\boldsymbol{\varphi}}]] + \frac{\partial \bar{\Psi}}{\partial \bar{\mathbf{n}}} \cdot \dot{\bar{\mathbf{n}}}. \quad (5.4.23)$$

With the interface part of the deformation power identity (5.4.11) the Clausius-Duhem inequality of the interface reads

$$\bar{\mathcal{D}} = \bar{\mathbf{T}} \cdot \llbracket \dot{\boldsymbol{\varphi}} \rrbracket - \frac{\partial \bar{\Psi}}{\partial \llbracket \boldsymbol{\varphi} \rrbracket} \cdot \llbracket \dot{\boldsymbol{\varphi}} \rrbracket - \frac{\partial \bar{\Psi}}{\partial \bar{\mathbf{n}}} \cdot \dot{\bar{\mathbf{n}}} \geq 0. \quad (5.4.24)$$

For elastic material behavior, the dissipation has to be zero. With the definition of the traction separation law $\bar{\mathbf{T}} = \partial \bar{\Psi} / \partial \llbracket \boldsymbol{\varphi} \rrbracket$ and the assumption that the normal vector can change $\dot{\bar{\mathbf{n}}} \neq \mathbf{0}$, the equation can only be satisfied if $\partial \bar{\Psi} / \partial \bar{\mathbf{n}} = \mathbf{0}$. This corresponds to an isotropic material behavior.

5.5. Discretization and linearization

The variational formulation (5.3.11) is discretized by means of the finite element method. For literature for the finite element method in the geometrically nonlinear setting we refer to the textbooks of Bonet and Wood [19] and Wriggers [135].

In the present approach the discontinuity can arbitrarily intersect elements and is therefore independent of the discretization. To allow for the discontinuity within certain elements the same discontinuous elements as in chapter 3.5 are applied and the approach is extended to the three dimensional case.

5.5.1. Formulation of a discontinuous element

The formulation of the discontinuous elements is described in detail in section 3.5.1 and only the main ideas are summarized here. If an element is splitted, additional degrees of freedom are introduced at the existing nodes. It is checked if the degrees of freedom were already introduced by a former element split, then no new ones have to be introduced, but only the element connectivity has to be changed. The introduction of the new degrees of freedom leads in a way to the doubling of the splitted elements. A new set of basis function is proposed, which is zero in one part of the element and equal to the standard basis functions in the other part. The construction of the discontinuous elements is similar for different types of elements of higher order or dimension. According to the geometrically linear case the additional degrees of freedom are global. Therefore the overall number of degrees of freedom changes during the simulation of crack propagation.

5.5.2. Discrete weak formulation

For the spatial discretization of the weak formulation we resort to the isoparametric concept. The domain \mathcal{S} is divided into n_{el} elements \mathcal{S}_e . The geometry is described by means of shape functions N^i and the node point coordinates \mathbf{X}_i in the material

configuration

$$\mathcal{S} = \bigcup_e^{n_{el}} \mathcal{S}_e \quad \mathbf{X}|_{\mathcal{S}_e} = \sum_{i=1}^{n_{en}} N^i \mathbf{X}_i. \quad (5.5.1)$$

The deformation map $\boldsymbol{\varphi}$ and the test function $\delta\boldsymbol{\varphi}$ are approximated with the same shape functions

$$\boldsymbol{\varphi}|_{\mathcal{S}_e} = \sum_{i=1}^{n_{en}} N^i \boldsymbol{\varphi}_i \quad \delta\boldsymbol{\varphi}|_{\mathcal{S}_e} = \sum_{i=1}^{n_{en}} N^i \delta\boldsymbol{\varphi}_i \quad (5.5.2)$$

and the approximation of their gradients with respect to the reference coordinates results as

$$\nabla_{\mathbf{X}} \boldsymbol{\varphi}|_{\mathcal{S}_e} = \sum_{i=1}^{n_{en}} \boldsymbol{\varphi}_i \otimes \nabla_{\mathbf{X}} N^i \quad \delta\mathbf{F}|_{\mathcal{S}_e} = \sum_{i=1}^{n_{en}} \delta\boldsymbol{\varphi}_i \otimes \nabla_{\mathbf{X}} N^i. \quad (5.5.3)$$

It is emphasized that in contrast to the extended finite element method the jump is not an explicit variable and its discretization arises automatically from the independent approximation of the two deformation maps

$$\begin{aligned} \llbracket \boldsymbol{\varphi} \rrbracket|_{\Gamma} &= \sum_{i=1}^{n_{en}^+} N^i|_{\Gamma} \boldsymbol{\varphi}_i^+ - \sum_{i=1}^{n_{en}^-} N^i|_{\Gamma} \boldsymbol{\varphi}_i^- = \sum_{p=1}^{n_{en}+n_{en}^*} J^p \boldsymbol{\varphi}_p \\ \llbracket \delta\boldsymbol{\varphi} \rrbracket|_{\Gamma} &= \sum_{i=1}^{n_{en}^+} N^i|_{\Gamma} \delta\boldsymbol{\varphi}_i^+ - \sum_{i=1}^{n_{en}^-} N^i|_{\Gamma} \delta\boldsymbol{\varphi}_i^- = \sum_{p=1}^{n_{en}+n_{en}^*} J^p \delta\boldsymbol{\varphi}_p. \end{aligned} \quad (5.5.4)$$

Thereby $\boldsymbol{\varphi}_i^+$ and $\boldsymbol{\varphi}_i^-$ denote the nodal deformation map at the element nodes n_{en}^+ and n_{en}^- . The newly introduced set J comprises the shape functions, evaluated at Γ , and the corresponding algebraic sign, such that the jump terms are obtained. Furthermore the discretization of the average deformation gradient (5.2.23) will be expressed as

$$\bar{\mathbf{F}}|_{\Gamma} = \frac{1}{2} \left[\sum_{i=1}^{n_{en}^+} \boldsymbol{\varphi}_i^+ \otimes \nabla_{\mathbf{X}} N^i|_{\Gamma} + \sum_{i=1}^{n_{en}^-} \boldsymbol{\varphi}_i^- \otimes \nabla_{\mathbf{X}} N^i|_{\Gamma} \right] = \sum_{p=1}^{n_{en}+n_{en}^*} \boldsymbol{\varphi}_p \otimes \mathbf{L}^p. \quad (5.5.5)$$

The set \mathbf{L} contains the gradients of the shape function, evaluated at Γ , and the factor 0.5.

The discretization of the weak formulation leads to the discrete algorithmic balance of momentum in terms of the vector-valued residual

$$\mathbf{R}_I(\boldsymbol{\varphi}) = \mathbf{R}_I^{int} + \mathbf{R}_I^{coh} - \mathbf{R}_I^{ext} = \mathbf{0} \quad (5.5.6)$$

The discretization of the weak form in the spatial configuration (5.3.11) results in the following particular parts of \mathbf{R}_I

$$\mathbf{R}_I^{int} = \mathbf{A}_{e=1}^{n_{el}} \int_{\mathcal{S}_e \cup \mathcal{S}_d^{+,-}} \nabla_{\mathbf{x}} N^i \cdot \boldsymbol{\sigma} \, dv, \quad \mathbf{R}_I^{coh} = \mathbf{A}_{e=1}^{n_{el}} \int_{\bar{\gamma}_e} J^i \bar{\mathbf{t}}(\llbracket \boldsymbol{\varphi} \rrbracket) \, da, \quad \mathbf{R}_I^{ext} = \mathbf{A}_{e=1}^{n_{el}} \int_{\partial \mathcal{S}_e} N^i \mathbf{t}^p \, da.$$

(5.5.7)

The discretization of the weak form in the material configuration (5.3.6) results in the equivalent discrete formulation

$$\mathbf{R}_I^{int} = \mathbf{A}_{e=1}^{n_{el}} \int_{\mathcal{B}_e \cup \mathcal{B}_d^{+,-}} \nabla_{\mathbf{X}} N^i \cdot \mathbf{P} dV, \quad \mathbf{R}_I^{coh} = \mathbf{A}_{e=1}^{n_{el}} \int_{\Gamma_e} J^i \bar{\mathbf{T}}([\varphi]) dA, \quad \mathbf{R}_I^{ext} = \mathbf{A}_{e=1}^{n_{el}} \int_{\partial \mathcal{B}_{te}} N^i \mathbf{T}^p dA. \quad (5.5.8)$$

Herein the operator $\mathbf{A}_{e=1}^{n_{el}}$ denotes the assembly of all element contributions at the element nodes, including the newly introduced ones, $i = 1, n_{en} + n_{en}^*$, to the overall residual at the global node points $I = 1, n_{np} + n_{np}^*$.

5.5.3. Linearized discrete weak formulation

Equation (5.5.6) represents the governing system of equations. Due to the geometrically nonlinear setting, the nonlinear constitutive law and the changing geometry, the system of equations has to be solved iteratively. A Newton-Raphson scheme is applied and therefore the linearization of equation (5.5.6) is performed

$$\mathbf{R}_I^{k+1} = \mathbf{R}_I^k + d\mathbf{R}_I = \mathbf{0} \quad \text{with} \quad d\mathbf{R}_I = \sum_{L=1}^{n_{np} + n_{np}^*} \mathbf{K}_{IL} d\varphi_L. \quad (5.5.9)$$

The global tangent stiffness matrix \mathbf{K}_{IJ} contains parts due to the linearization of the internal virtual work and of the additional virtual work contribution due to the cohesive tractions at the internal boundary. We recall the linearized continuous equations (5.3.15) and (5.3.16), introduce the discrete quantities and obtain the tangential stiffness matrices

$$\mathbf{K}_{IJ}^{int} = \mathbf{A}_{e=1}^{n_{el}} \int_{\mathcal{S}_e \cup \mathcal{S}_d^{+,-}} \nabla_{\mathbf{x}} N^i \cdot \mathbf{e} \cdot \nabla_{\mathbf{x}} N^j dv + \int_{\mathcal{S}_e \cup \mathcal{S}_d^{+,-}} \nabla_{\mathbf{x}} N^i \cdot \boldsymbol{\sigma} \cdot \nabla_{\mathbf{x}} N^j \mathbf{I} dv \quad (5.5.10)$$

$$\mathbf{K}_{IJ}^{coh} = \mathbf{A}_{e=1}^{n_{el}} \int_{\tilde{\gamma}_e} J^i \mathbf{T}_\varphi J^j da + \int_{\tilde{\gamma}_e} J^i \mathbf{T}_n \cdot \mathbf{G} \cdot \mathbf{L}^j da + \int_{\tilde{\gamma}_e} J^i \bar{\mathbf{t}} [\mathbf{A} \cdot \mathbf{L}^j] da.$$

The tangents \mathbf{T}_φ and \mathbf{T}_n contain the directional derivative of the cohesive traction $\bar{\mathbf{t}}$ with respect to the jump $[\varphi]$ and the normal vector $\bar{\mathbf{n}}$, respectively, compare equations (5.4.8) and (5.4.10). The third-order tensor \mathbf{G} is given in equation (5.3.20), and the second-order tensor \mathbf{A} summarizes the expression, which can be found in equation (5.3.28), $\mathbf{A} = [\mathbf{I} - \bar{\mathbf{n}} \otimes \bar{\mathbf{n}}] \cdot \bar{\mathbf{F}}^{-t}$.

In \mathbf{K}^{int} the material and geometric contributions of the element stiffness matrices are given. To simplify the notation the contributions of the unsplitted and of the two parts

of the splitted elements are summarized. The general structure of their element stiffness matrices is identical, unless, if an intersected element is considered, the usual shape functions N^i have to be replaced by the discontinuous ones \bar{N}^i , which become zero in the non considered part of the element.

The first term of the additional part of the tangent stiffness matrix \mathbf{K}^{coh} can be identified as the material part of the linearization of the cohesive traction term. It is identical with the one which is obtained in the geometrically linear case, compare [81] or [130]. The last two terms contain the geometric parts of the linearization, which are constituted by the change of the normal vector and of the area of the internal boundary. Due to these geometric parts of the linearization of the cohesive traction the tangent stiffness matrix loses its symmetry.

When the isotropic traction separation relation for the Piola traction vector (5.4.19) is used, it is advantageous to formulate the tangent stiffness matrix in the material configuration. This results in the simpler format

$$\mathbf{K}_{IJ}^{int} = \mathbf{A} \int_{\mathcal{B}_e \cup \mathcal{B}_d^{+,-}} \nabla_X N^i \cdot \mathbf{A} \cdot \nabla_X N^j dV \quad (5.5.11)$$

$$\mathbf{K}_{IJ}^{coh} = \mathbf{A} \int_{\Gamma_e} J^i \mathbf{T}_\varphi J^j dA$$

whereby \mathbf{A} denotes the second derivative of the strain energy density with respect to the deformation gradient $\mathbf{A} = \partial^2 \Psi / \partial \mathbf{F}^2$. Obviously the formulation is symmetric.

5.6. Implementation

The approach in the geometrically nonlinear setting is implemented for two and three dimensional problems. The implementation in two dimensions resembles the one described in section 3.6. The consideration of three dimensional problems leads to a more complicated implementation procedure, since especially the geometry of three dimensional crack modeling is more involved. The ideas about the handling of the complex geometry data, the geometrical representation of the crack path and the crack propagation procedure are mainly adopted from Sukumar et al. [125], Gasser and Holzapfel [43] and Areias and Belytschko [2].

For simplicity the method is implemented using linear tetrahedral elements, the discontinuity surface is flat within an element and intersects always the whole element. In the following details about the implementation in three dimensions are provided. Firstly the splitting of the intersected elements will be described. In the same manner as in the two dimensional case, the integration of the discontinuous elements requires special attention.

The geometrical representation of the crack path is considered, which is more involved as in two dimensions, since the crack-tip is not longer represented by a point but by a line.

5.6.1. Splitting of elements

The split of a tetrahedral linear element can produce two different combinations of subelements, provided that the surface is flat. If the intersection plane cuts three edges of the element, such that the element interface becomes triangular, a tetrahedral part and a polyhedral part with two triangular and three quadrilateral faces are generated, which is plotted in figure 5.5. For the integration the last-mentioned part can be further subdivided into three tetrahedrons. It is also possible that the discontinuity surface intersects four edges of the element, which leads to a quadrilateral interface and is illustrated in figure 5.5. Then the resulting subelements are both polyhedrons consisting of two triangular and three quadrilateral faces.

The geometry of the splitted elements can be simply represented by the intersection points in the reference configuration. These points as well as the geometry and volume of the subelements in the reference configuration do not change throughout a simulation and have to be calculated only once, when the discontinuity is introduced, and can be stored for the following load steps.

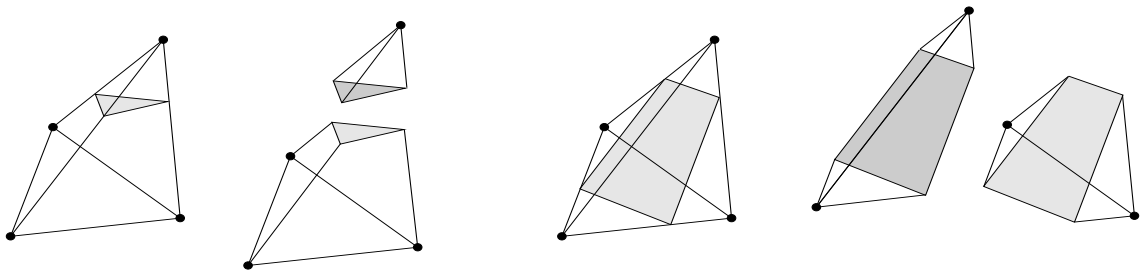


Figure 5.5.: Splitting of a tetrahedral element

5.6.2. Numerical integration

As already stated and similar to the two dimensional case a modified integration scheme is adopted for the intersected elements, since in general two different functions have to be integrated over the two particular elements parts. Depending on the splitting of the element it can be subdivided into four or six tetrahedral subdomains. This additional partitioning is applied in order to use the same central Gauss integration for each tetrahedral subdomain. The subdivision does not involve the introduction of new degrees of freedom, it is only performed to simplify the numerical integration.

When an element is intersected, firstly the coordinates of the intersection points are determined in global coordinates \mathbf{X} and in the local coordinate system $\boldsymbol{\xi}$. The coordinate

transformation from the global to the local coordinates is described by the Jacobian $\check{\mathbf{J}}$. The computation of the local coordinates of the intersection points requires a loop over the element edges, but it has to be carried out only once and only for the intersected elements. With the knowledge of the intersection points, the element is subdivided into four or six subtetrahedrons, their vertices expressed in the local coordinates of either the intersection points or the vertices of the parent tetrahedron.

Within each subdomain the coordinates of the Gauss point are calculated, which is simply done by the multiplication of the shape functions evaluated at the usual Gauss point position (which is in our case for central Gauss integration in a linear tetrahedron $\xi_{1,2,3} = 0.25$) with the vertex coordinates of the subelements. By means of an additional coordinate transformation with the Jacobian $\tilde{\mathbf{J}}$ from the local coordinates of the subelements $\boldsymbol{\eta}$,

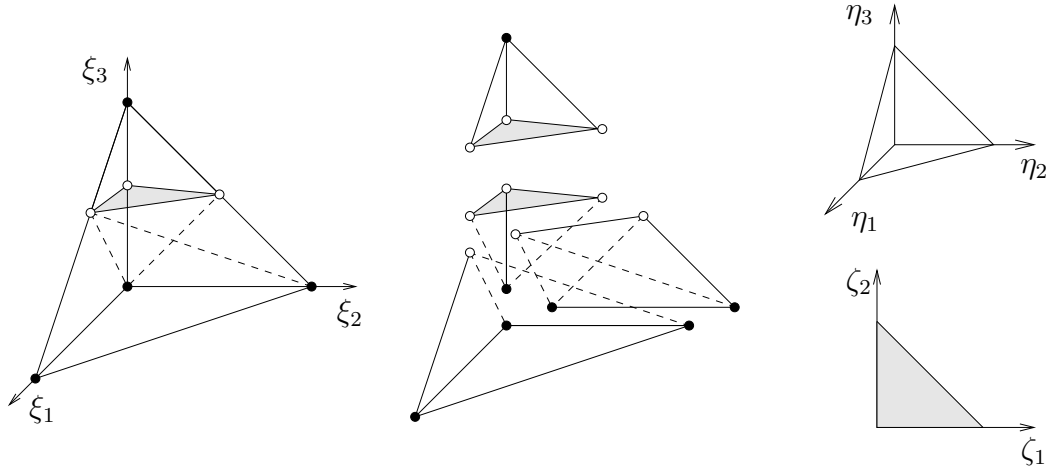


Figure 5.6.: Local coordinates of the subdivided element

which are indicated in figure 5.6, to the local coordinates of the parent tetrahedron, the integration can be accomplished over the subelements. Exemplarily the integration of a function $g(\mathbf{X})$, which exhibits a discontinuity along Γ_e , over an element \mathcal{B}_d , can be expressed as

$$\begin{aligned} \int_{\mathcal{B}_d} g(\mathbf{X}) dV &= \int_{\mathcal{B}_d^+} g^+(\mathbf{X}) dV + \int_{\mathcal{B}_d^-} g^-(\mathbf{X}) dV \\ &= \sum_{i=1}^{n_{gp}^+} g^+(\boldsymbol{\xi}_i) \det \check{\mathbf{J}}(\boldsymbol{\xi}_i) \det \tilde{\mathbf{J}}(\boldsymbol{\xi}_i) \alpha_i + \sum_{j=1}^{n_{gp}^-} g^-(\boldsymbol{\xi}_j) \det \check{\mathbf{J}}(\boldsymbol{\xi}_j) \det \tilde{\mathbf{J}}(\boldsymbol{\xi}_j) \alpha_j, \end{aligned} \quad (5.6.1)$$

whereby $n_{ng}^{+,-}$ is the number of Gauss points in each part of the splitted element, which here coincides with the number of subtetrahedrons. The Gauss point coordinates are denoted with $\boldsymbol{\xi}_i$ and the associated weighting factors with α_i .

In addition to the described volume integration the integration of the contributions due to the cohesive tractions has to be accomplished over the intersection plane. This leads

to the evaluation of a surface integral. The surface is either quadrilateral or triangular. Since we assume that the crack surface is flat and intersects the whole element, we can apply two dimensional numerical integration. An additional coordinate transformation from the global coordinates \mathbf{X} to the local ones $\boldsymbol{\zeta} \rightarrow \{\zeta_1, \zeta_2\}$ of the intersection surface is introduced. Since the dimension of $\boldsymbol{\zeta}$ is one less than the dimension of the global coordinates, the procedure is similar to the integration of an external surface loading. An incremental line element can be expressed in the local coordinates as

$$d\mathbf{X} = \hat{\mathbf{J}} \cdot d\boldsymbol{\zeta} = \begin{bmatrix} \frac{\partial X_1}{\partial \zeta_1} & \frac{\partial X_1}{\partial \zeta_2} \\ \frac{\partial X_2}{\partial \zeta_1} & \frac{\partial X_2}{\partial \zeta_2} \\ \frac{\partial X_3}{\partial \zeta_1} & \frac{\partial X_3}{\partial \zeta_2} \end{bmatrix} \cdot \begin{bmatrix} \zeta_1 \\ \zeta_2 \end{bmatrix} \quad (5.6.2)$$

whereby the Jacobian $\hat{\mathbf{J}}$ contains the partial derivatives of the global with respect to the local coordinates. Note that $\hat{\mathbf{J}}$ is not square. An incremental area element can then be calculated as the norm of the cross product of two incremental line elements

$$dA = \left\| \begin{bmatrix} \hat{J}_{11} \\ \hat{J}_{21} \\ \hat{J}_{31} \end{bmatrix} \times \begin{bmatrix} \hat{J}_{12} \\ \hat{J}_{22} \\ \hat{J}_{32} \end{bmatrix} \right\| d\zeta_1 d\zeta_2 \quad (5.6.3)$$

The surface integration can be accomplished as in usual triangular or quadrilateral two dimensional elements, whereby the vertices are represented by the points of intersection. For the integration over the triangular surfaces three Gauss points are introduced and four Gauss points are used for the integration over a quadrilateral section plane.

5.6.3. Crack propagation and crack path representation

One major constraint in the present formulation in three dimensions is that the crack geometry is restricted to planar cracks, which means that the normal vector to the crack plane is identical in each element (in the reference configuration). This is not a general limitation of the element formulation but an assumption that is made to simplify the geometrical representation of the crack surface and the crack propagation. In the special case of planar crack propagation, crack path continuity is automatically ensured in three dimensions. If non-planar crack growth is considered the crack path becomes either discontinuous as in [43], or the normal vector of the crack surface in one element has to be influenced by the neighboring ones to ensure crack path continuity [2]. The crack plane is sufficiently defined by its normal vector and one point, which is in the in section plane. But in three dimensions the crack surface composes an intersection line with the faces of the splitted element, which usually does not go with the normal vector. However, when the crack surface is plane, these additional difficulties would not exist, since the normal

vectors of two neighboring elements are equal and therefore the intersection line with the crack surface of the two elements is equal.

The direction of crack propagation is predetermined but nevertheless a failure criterion has to be defined to decide whether the crack propagates or not. A criterion of Rankine type is used. If the principal stress in the elements ahead of the crack-tip exceeds the tensile strength of the material the discontinuity is elongated.

The crack surface is represented by means of the triangular and quadrilateral intersection planes, each described by a point, lying on the surface, and the normal vector. The elements, which possess a neighboring element, that is not cracked, belong to the crack-tip elements. And in particular the faces of splitted elements, connected to unsplitted elements, constitute the set of crack-tip faces. The failure criterion is checked for all elements that border a crack-tip face. If the failure criterion is met, the set of splitted elements, of the crack-tip elements and of the crack-tip faces has to be updated. Furthermore the new degrees of freedom have to be introduced. The load step is recalculated with the modified geometry and the crack criterion is controlled for the new set of elements next to the crack-tip faces. The procedure is repeated until no further element failure is observed.

5.6.4. Algorithmic implementation

The decisive differences of the present approach to a usual finite element code, concerning the implementation, is the introduction of the discontinuous elements. This modification can be easily realized. Since the discontinuous elements consist in a way of two continuous ones with a modified integration region, the element routine has to be altered only little. The shape functions and the number of degrees of freedom for each part of the discontinuous element are as usual. The geometry of the element parts and the subdivision of the elements is stored once and then used for the evaluation of the element residual and its derivative. The implementation of the discontinuous elements further requires a routine to store the cracked elements and to decide whether the usual element routine or the 'discontinuous element' routine is called. In the considered case of cohesive cracks, an additional subroutine for the calculation of the surface tractions is required.

The implementation of the crack propagation entails additional post-processing steps, including the introduction of the new degrees of freedom and the determination of the geometry of the splitted elements. As already mentioned, the discontinuity is elongated if the elements next to the crack tip faces satisfy the failure criterion. When an element cracks, firstly the degrees of freedom are updated, in consideration of the constraint at the crack tip. Then the different sets, containing the cracked elements and the crack-tip elements, are changed. For each splitted element the intersection points and the geometry of the element parts are stored since they do not change during the simulation. To decide

which elements are connected to the crack tip faces not only the usual element connectivity has to be provided but also the face connectivity. This can be calculated once in the beginning of the simulation and is not changed. The general steps of the numerical implementation for one load step are summarized in following table.

| |
|---|
| repeat |
| global Newton iteration |
| loop over unsplitted elements \mathcal{B}_e |
| calculation of element residua \mathbf{R}_e^{int} and their derivatives \mathbf{K}_e^{int} |
| loop over splitted elements \mathcal{B}_d |
| readout intersection points and geometry |
| loop over the subdomains |
| calculation of the contributions of the subdomains to the element residua and their derivatives |
| assembly of \mathbf{R}_d^{int} and \mathbf{K}_d^{int} |
| calculation of the surface contributions \mathbf{R}_e^{coh} and \mathbf{K}_e^{coh} |
| assembly of global residual \mathbf{R} and tangent stiffness \mathbf{K} |
| solution of equilibrium equation, calculation of nodal deformation map φ |
| calculation of Cauchy stresses $\boldsymbol{\sigma}$ |
| control crack criterion for the elements next to the crack tip faces |
| if $\sigma_1 > f_t$ introduction of new degrees of freedom |
| update of the set of the cracked elements and the crack-tip faces |
| determine intersection points and geometry of splitted element |
| until crack geometry is stable, $\sigma_1 < f_t$ |

5.7. Numerical examples

In this section numerical examples are presented to demonstrate the applicability of the approach. The first two examples deal with two dimensional crack propagation. Thereby the presented method is implemented, using linear triangular elements. The primary aim

of the examples is to show the capability of the proposed strategy to simulate propagating discontinuities independently of the discretization. Therefore the computation of the two examples is carried out with varying discretizations, considering structured as well as unstructured meshes. The deformation of the structures as well as overall load displacement answers are compared for the different meshes. Another purpose of the examples is to verify the accomplished linearization of the cohesive traction. Therefore the transversely isotropic traction separation law (5.4.6) is applied. The second example is unsymmetric, which leads to rotations of the discontinuity surface.

The last two examples consider three dimensional crack propagation. The first example deals with a rectangular block under tension and is mainly used to check the implementation of the method. The example is calculated with three different discretizations. In the second example the three dimensional version of the symmetric peel test is calculated. The results for different meshes are compared to analyze the convergence of the method.

5.7.1. Two dimensional crack propagation

Symmetric peel test

In the first example a symmetric peel test is considered. A cantilever beam is loaded by prescribed displacements, the geometry and the loading conditions are depicted in figure 5.7. The discontinuity is initiated in the middle of the beam and propagates along a straight line during additional loading. The computation is carried out with two different discretizations, a structured mesh with 500 elements and an unstructured mesh with 520

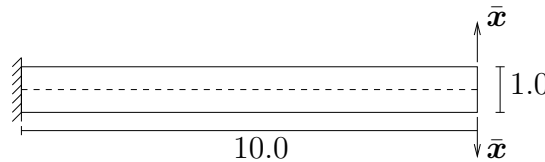


Figure 5.7.: Geometry and loading conditions, symmetric peel test

elements. The material parameters are chosen as $\lambda = 2778$, $\mu = 4167$, $f_t = 200$ and the tangential stiffness d is set to zero. The fracture energy is equal to $G_f = 100$.

Due to the symmetry of the example, the fictitious discontinuity surface, which is located in the middle of the two crack surfaces, does not change its orientation during the delamination process. Therefore this example can not be used to check the the geometric contributions of the linearization of the cohesive tractions, but to examine the influence of the different discretizations. We apply the prescribed displacement in constant increments of 0.04. After each load step the stress state in the element ahead of the crack tip is compared with the tensile strength. If the tensile strength is exceeded the discontinuity is introduced into this element. Under these modified boundary conditions (with

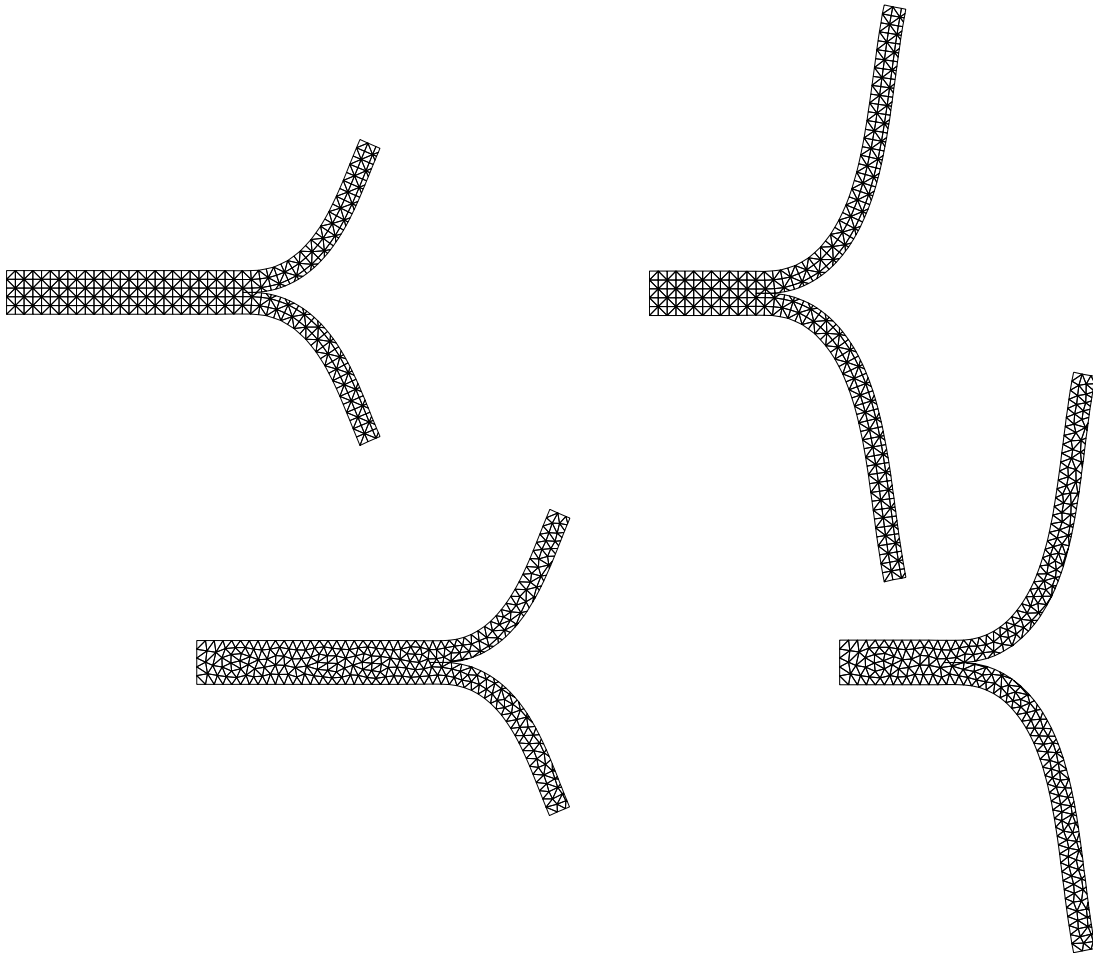


Figure 5.8.: Deformation of the structure, structured and unstructured mesh

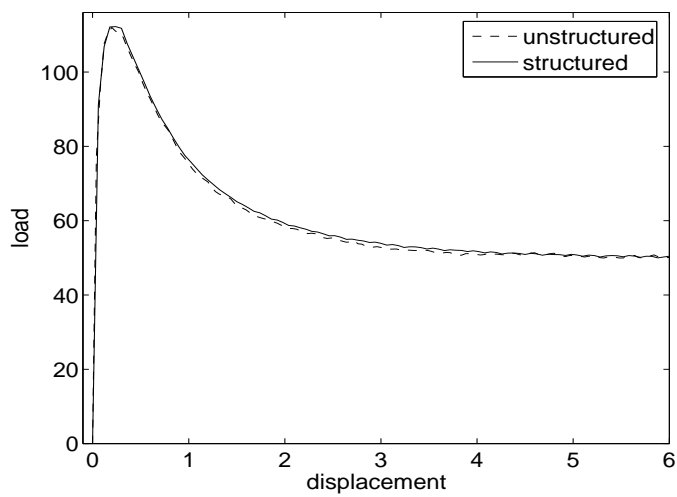


Figure 5.9.: Load displacement relation, structured and unstructured mesh

the extended discontinuity) the calculation of the present load step is repeated and the stress state in the element ahead of the crack tip is calculated again, to decide, if the discontinuity propagates further. The next displacement increment is applied, when an equilibrium state is accomplished and the stresses ahead of the discontinuity do not exceed the tensile strength. To avoid penetration of the cohesive zone, a standard penalty method with a high normal penalty stiffness is applied.

In figure 5.8 the deformation of the structure at two different load steps, calculated with the structured and the unstructured mesh is plotted. It is visible that the results are similar for both discretizations. This is confirmed by the global load displacement responses, depicted in figure 5.9. The load displacement answers are identical for the different meshes and do not show any significant oscillations, even for the comparatively low number of elements. In the beginning the load increases up to a critical value and then softening takes place. Afterwards the reaction force remains at a constant value. Due to the imposed boundary conditions a full delamination of the structure is prevented.

Nonsymmetric peel test

In the second example a nonsymmetric peel test is considered. Thereby one layer is peeled from another one, which is fixed at the bottom. The boundary conditions and the geometry are shown in figure 5.10. The material parameters are similar to the first example, but $G_f = 50$. In this example the fictitious discontinuity surface undergoes

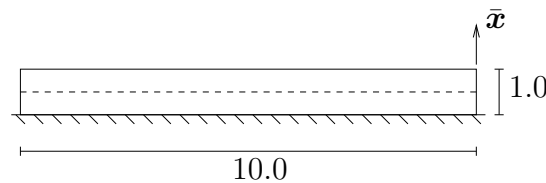


Figure 5.10.: Geometry and loading conditions, unsymmetric peel test

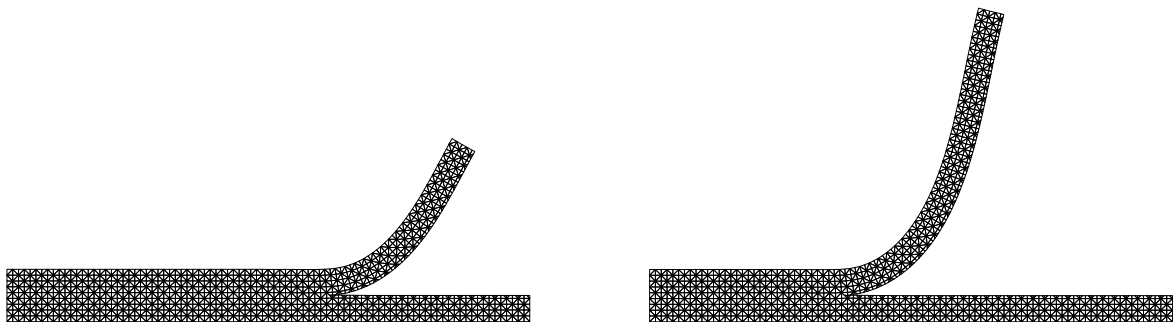


Figure 5.11.: Deformation of the structure, unsymmetric peel test, 1620 elements

large rotations and the orientation of its normal vector changes significantly during the computation. Therefore this example enables us to verify the linearization of the traction vector numerically. In order to compare the influence of different discretizations, two

different structured meshes are used, one with 1620 elements and a finer one with 3380 elements. An additional computation with an unstructured mesh was not accomplished, since the results in the first example were similar for structured and unstructured meshes with comparably many elements.

In figure 5.11 the deformation of the structure for the discretization with 1620 elements is shown. The deformation of the structure calculated with the finer discretization looks

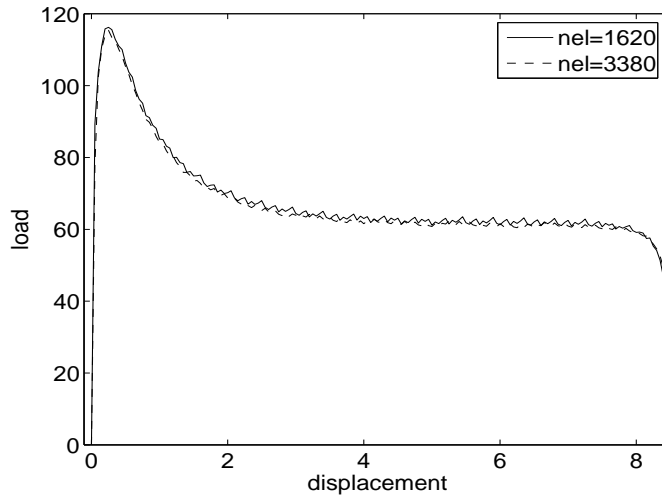


Figure 5.12.: Load displacement relation, 1620 elements and 3380 elements

alike. However, in contrast to the first example the coarser discretization reveals small oscillations in the global load displacement answer, see figure 5.12. These oscillations are smoothed out when the finer discretization is considered and can therefore be linked to the elementwise failure. As expected, the global load displacement relations show the same characteristics as in the first example: increasing load up to a critical value, softening and a constant reaction force until full delamination occurs.

During the computation the convergence behavior is monitored by means of the norm of the residual. Quadratic convergence was achieved in all loadsteps, which numerically confirms the performed linearization.

5.7.2. Three dimensional crack propagation

Rectangular block under tension

The first example in three dimensions is a simple mode *I* failure problem to check the implementation of the method and the dependence of the solution on the discretization. We consider a rectangular block under a tensile load. The block is fixed on one side and loaded by a prescribed displacement on the other side. Failure is initialized on two sides of the specimen, as indicated in figure 5.13. The material parameters are chosen as $E = 10000 \text{ N/mm}$, $\nu = 0.3$, $f_t = 200 \text{ N/mm}^2$ and $G_f = 100 \text{ N/mm}$. The block has a

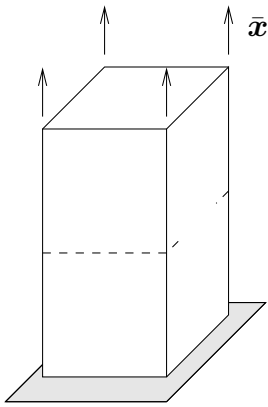


Figure 5.13.: Geometry

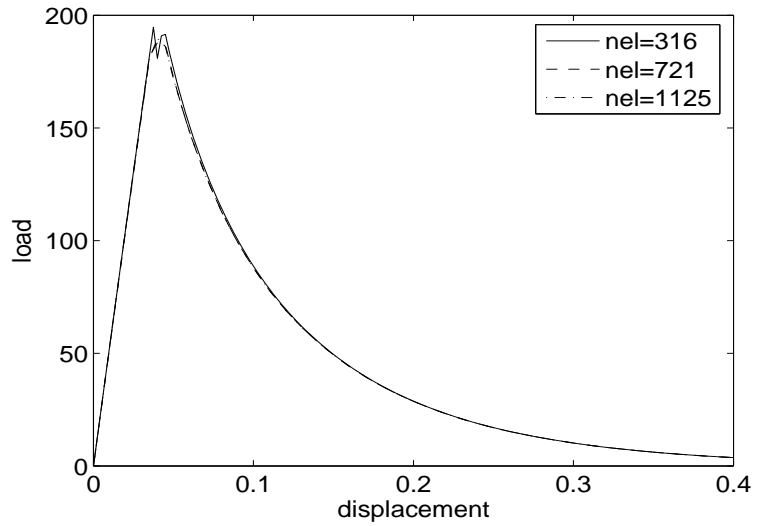


Figure 5.14.: Load displacement relations

squared base of $1\text{ mm} \times 1\text{ mm}$ and is 2 mm high.

In order to compare the results of different discretizations the computation is carried out with three different meshes, containing 316, 720 and 1125 elements. When the critical stress state is reached, the crack propagates through the specimen on a straight horizontal path. The cohesive tractions prevent the complete separation of the two parts of the block. The deformation of the block is shown for the discretization with 1125 elements in figure 5.15. The first deformation belongs to the precritical state. The applied displacement is 0.04 mm . The two other pictures show post critical deformation states at prescribed displacements of 0.2 mm and 0.4 mm .

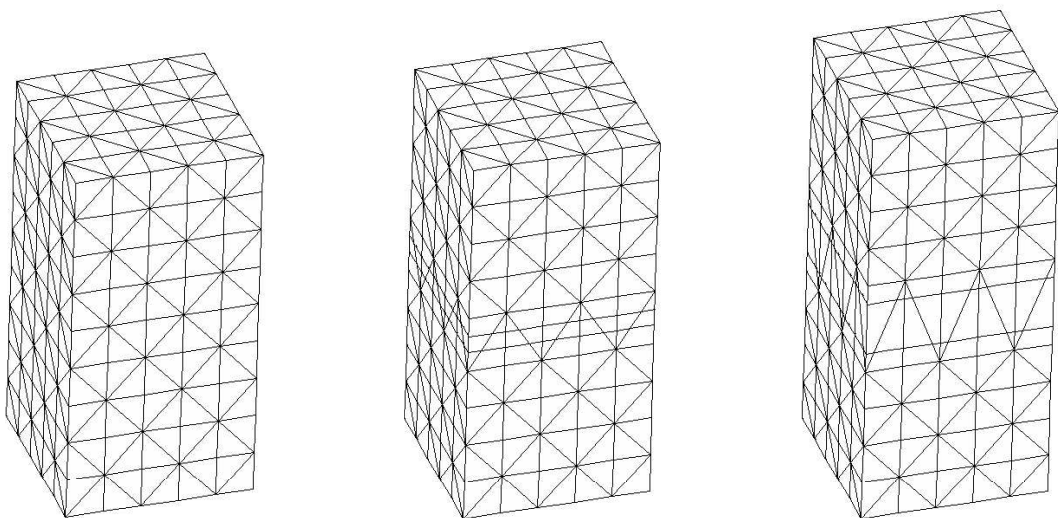


Figure 5.15.: Deformation of the block at different load steps

In figure 5.15 the separation of the two sides of the discontinuity surface is indicated by plotting the intersection planes in addition to the usual elements. It is visible that the opening increases significantly. The expected exponential unloading with an increasing opening can be verified by the load displacement diagram in figure 5.14. The resultant force on top (or bottom) of the block is plotted versus the prescribed displacement. As expected an initially elastic behavior can be observed. When the critical stress state is reached the load drops down rapidly and decreases exponentially with the opening. The global load displacement answer is given for the three different discretizations and it can be verified that the solutions are independent of the discretization. Minor differences between the answer of the coarse discretization and the two others, close to the point of maximum tensile stress, can be explained by the failure criterion. The stresses in the elements ahead of the crack tip are compared with the critical stress. If the elements are too large, the stress calculation becomes incorrect. But it can be seen that these oscillations are smoothed out even for the mesh with 712 elements. The computations for the different discretizations are in good agreement and the expected results were obtained.

Symmetric peel test

As a second example the symmetric peel test is recalculated in three dimensions. A cantilever beam is fixed on one side and a displacement is prescribed on the upper and lower edge on the other end of the beam. The crack is initialized in the middle on the right hand

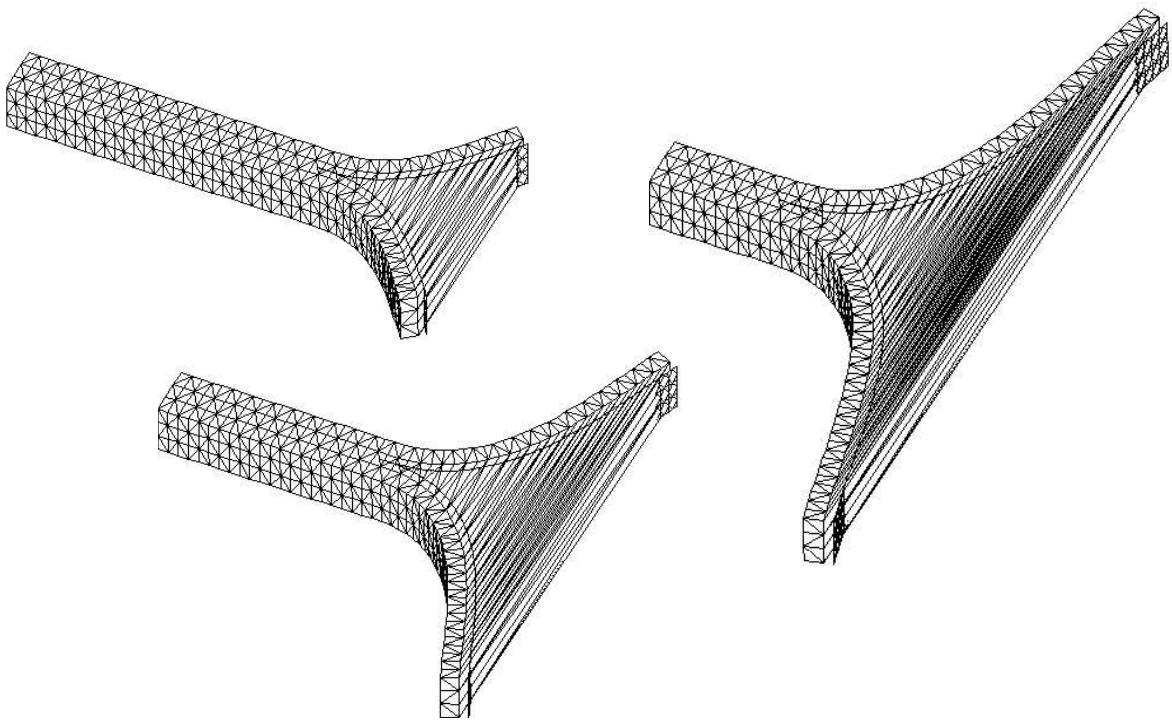


Figure 5.16.: Deformation of the structure at different load steps

side of the beam and the propagation of the crack is governed by the failure criterion and fixed to the horizontal plane. The material parameters are chosen accordingly to the two dimensional problem in order to compare the results. The geometry is chosen similar to the two dimensional example, the thickness is given as 1 mm such that a quadratic cross section is generated.

To avoid penetration of the cohesive zone an additional penalty constraint is added to the weak form. The computations are accomplished with three different meshes with 2250, 3750 and 6250 linear tetrahedral elements. The displacement is prescribed in 100 increments and the largest displacement on each side is 6 mm , therefore the largest opening displacement is 12 mm . Since the specimen is fixed on the left hand side the whole separation of the two layers is prevented. The deformation of the structure is pictured in figure 5.16 for different prescribed displacements. In addition to the element surfaces the crack surfaces are indicated to clarify that the elements, which exhibit the discontinuity, are not highly deformed but splitted into two parts. The deformation is symmetric as expected and the discontinuity propagates along the center line, but is not aligned with the element boundaries. The load displacement answers are calculated for the three different discretizations and plotted in figure 5.17. It is noticeable that the load displacement

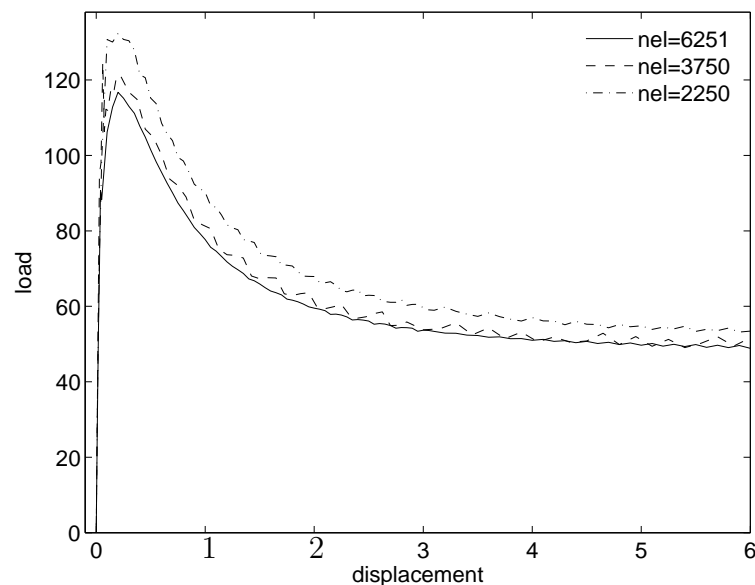


Figure 5.17.: Load displacement relation

answer for the coarse discretization is quite different, compared to the other two. The maximum reaction force is overestimated and also the post peak behavior shows minor differences. The main reason for that can be found in the failure criterion, which considers only the elements next to the crack tip. The elements are too large, to approximate the high stress gradients correctly. Therefore the somehow smeared stresses in the large elements are smaller and failure occurs later than in smaller elements. In general the

discretization with only 2250 elements is not sufficient. But the general structure of the load displacement relations are equal and comparable with the two dimensional case. We have an increasing force up to to a peak load, followed by a softening and a constant reaction force. And the results converge with a finer discretization. The load displacement answer of the finer discretization with 3750 elements shows some small oscillations, which are associated to the elementwise failure, as in the two dimensional setting. These oscillations are smoothed out in the load displacement answer for the sufficiently fine discretization with 6250 elements. The load displacement relations for the simulation with 3750 and 6250 elements are in very good agreement with the results of the two dimensional calculation.

5.8. Summary

A finite element method for the computational modeling of propagating discontinuities at finite deformations was introduced. The discontinuity can arbitrarily intersect the elements and the discontinuity path is therefore independent of the underlying finite element mesh. The characteristic feature of the method is the construction of the elements, which are intersected by the discontinuity. Additional displacement degrees of freedom are introduced at the existing nodes and only the standard basis functions are used. To model softening behavior, the cohesive crack concept is utilized. Cohesive tractions are applied at the interface, determined by a traction separation law. The weak formulation, its discretization and the consistent linearization, which is fundamental for the numerical solution, were provided. In the presented numerical examples in two and three dimensions the ability of the method to simulate propagating discontinuities independently of the mesh structure was pointed out.

6. Mesh-independent modeling of weak discontinuities at finite strains

The present chapter implies the extension of the approach which was introduced in chapter 4 to finite strains and is based on reference [83]. The approach allows for the modeling of weak discontinuities independent of the underlying finite element mesh. Therefore the same discontinuous elements as in the previous chapters are used. Along the internal interface a Nitsche type method is applied to enforce the continuity of the deformation map. Nitsche's method is extended to finite strains.

6.1. Motivation

This section extends the approach for the mesh-independent modeling of weak discontinuities, which was introduced in chapter 4, to finite strains. The term weak discontinuity describes a jump in the gradient of the deformation map, which occurs if we consider different materials within a body, inclusions or holes. Usually in the framework of finite elements weak discontinuities are taken into account by letting the element boundaries coincide with the discontinuity surface. However, if inclusions with various geometries are considered or moving internal boundaries are treated, it can be advantageous to avoid the meshing of the discontinuity surface. The present approach uses discontinuous elements and a Nitsche type method to impose the continuity of the deformation map along the internal boundary.

The discretization is carried out with the already in detail characterized discontinuous elements, compare section 3.5.1 or the references [46] and [81]. Additional global degrees of freedom are introduced and a new set of discontinuous shape functions allows for the simulation of a jump of the deformation map within the elements.

The discontinuous elements allow as well for a jump in the deformation map as in its gradient. In the same manner as in the linear case in chapter 4 a Nitsche type method [95] is introduced along the internal boundary to ensure continuity in the deformation map in a weak sense. Nitsche's method is extended for the geometrically nonlinear setting. The governing equations are determined by means of the principle of stationary potential energy and lead to a quite similar formulation as in the linear case. Nitsche's method was also applied as a mortaring method by Stenberg [122] and Heinrich [54], a domain decomposition method by Becker et al. [13] or for contact problems [136]. Another area of application is the enforcement of essential boundary conditions in the framework of

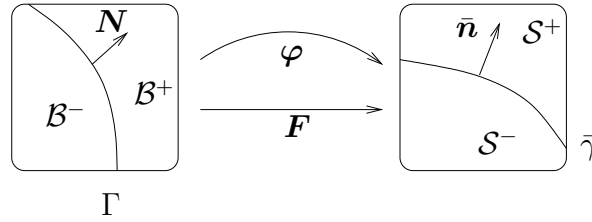


Figure 6.1.: Weak discontinuity kinematics

meshless methods, compare [44] and [40].

In the next section the nonlinear kinematics regarding a weak discontinuity are introduced. Afterwards the variational formulation is determined from the principle of stationary potential energy. Some details about the discretization and the implementation are recapitulated and finally numerical examples are presented.

6.2. Kinematics

We consider a body \mathcal{B} in the reference configuration, which is divided by a discontinuity surface Γ into the parts \mathcal{B}^+ and \mathcal{B}^- . The associated normal vector \mathbf{N} points from \mathcal{B}^- to \mathcal{B}^+ . We assume that a weak discontinuity can occur along the internal discontinuity boundary. In the present approach the continuity of the deformation map will be ensured in a weak sense, adopting additional terms in the weak formulation. Therefore we can use the same kinematical assumptions as for strong discontinuities in the previous chapter. Accordingly we have a nonlinear and noncontinuous deformation map φ , which maps the body from the reference configuration \mathcal{B} to its spatial configuration \mathcal{S} , see figure 6.1. We split the deformation map in two continuous parts, each one only defined on one side of the discontinuity surface

$$\varphi(\mathbf{X}) = \begin{cases} \varphi^+(\mathbf{X}) & : \mathcal{B}^+ \rightarrow \mathcal{S}^+ \\ \varphi^-(\mathbf{X}) & : \mathcal{B}^- \rightarrow \mathcal{S}^- \end{cases} \quad (6.2.1)$$

Since the two parts of the deformation map are independent, the gradients and the strain measures are also defined for each part of the body separately. The discontinuous deformation map reads

$$\mathbf{F} = \begin{cases} \mathbf{F}^+ = \nabla_{\mathbf{X}} \varphi^+ \\ \mathbf{F}^- = \nabla_{\mathbf{X}} \varphi^- \end{cases} \quad (6.2.2)$$

Since \mathbf{F}^+ and \mathbf{F}^- denote gradients of two independent functions, it is of course possible that they take different values at the internal interface, which leads to a weak discontinuity.

In contrast to the problem involving strong discontinuities, the two sides of the discontinuity remain on each other in the spatial configuration. Therefore it is possible to define a unique spatial normal vector $\bar{\mathbf{n}}$ to the discontinuity surface $\bar{\gamma}$. The jump in the deformation map and its weighted average value are defined as

$$\llbracket \boldsymbol{\varphi} \rrbracket := \boldsymbol{\varphi}_{|\Gamma}^+ - \boldsymbol{\varphi}_{|\Gamma}^- \quad \{\boldsymbol{\varphi}\} := \kappa^+ \boldsymbol{\varphi}_{|\Gamma}^+ + \kappa^- \boldsymbol{\varphi}_{|\Gamma}^-. \quad (6.2.3)$$

The weighted average term was already introduced in equation (4.2.3) and is defined here in the same manner.

6.3. Variational formulation

To derive the weak formulation for a problem involving discontinuities in the deformation gradient, we apply a variant of Nitsche's method [95], which is closely related to the approach in [46]. If we want to model weak discontinuities we assume that the deformation gradient can exhibit a jump along the interface, but the deformation map shall be continuous. Since our kinematic assumption of two independent deformation maps allows for jumps in both the deformation map and its gradient, we need to ensure the continuity of the deformation map. This is enforced in a weak sense by means of an extended Nitsche's method, applied along the internal interface.

6.3.1. Principle of stationary potential energy

The variational formulation of the problem is derived based on the principle of stationary potential energy, which leads to a symmetric formulation. Thereby we require the existence of an energy functional Π . The total potential energy is usually given as the sum of the internal and external potential energy. Since we want to apply a variant of Nitsche's method, we obtain an additional interfacial energy contribution, similar to the linear case. This leads to the weak fulfillment of the continuity condition, and vanishes if the continuity condition is exactly satisfied.

We start with the definition of the total potential energy

$$\Pi(\boldsymbol{\varphi}) = \int_{\mathcal{B}^+ \cup \mathcal{B}^-} \Psi(\mathbf{F}(\boldsymbol{\varphi})) dV + \bar{\Pi}(\boldsymbol{\varphi}^+, \boldsymbol{\varphi}^-) - \int_{\partial \mathcal{B}_t} \boldsymbol{\varphi} \cdot \mathbf{T}^p dA, \quad (6.3.1)$$

whereby the $\bar{\Pi}(\boldsymbol{\varphi}^+, \boldsymbol{\varphi}^-)$ denotes the additional term at the internal interface, which depends on the field values in both parts of the body. The strain energy density $\Psi(\mathbf{F}(\boldsymbol{\varphi}))$ specifies the internal energy stored in the body during an elastic deformation and the tractions \mathbf{T}^p are prescribed at the Neumann boundary.

The additional interface contribution is given by

$$\bar{\Pi}(\boldsymbol{\varphi}^+, \boldsymbol{\varphi}^-) = \int_{\Gamma} \llbracket \boldsymbol{\varphi} \rrbracket \cdot \{\mathbf{P}(\mathbf{F}(\boldsymbol{\varphi}))\} \cdot \mathbf{N} dA + \frac{1}{2} \int_{\Gamma} \theta \llbracket \boldsymbol{\varphi} \rrbracket \cdot \llbracket \boldsymbol{\varphi} \rrbracket dA, \quad (6.3.2)$$

whereby $\{\mathbf{P}\} = \kappa^+ \mathbf{P}^+ + \kappa^- \mathbf{P}^-$ denotes the weighted average of the Piola stress tensor. It can easily be verified that this additional interface term vanishes if the continuity condition is exactly fulfilled, that is $[[\boldsymbol{\varphi}]] = 0$. The second part of $\bar{\Pi}(\boldsymbol{\varphi}^+, \boldsymbol{\varphi}^-)$ can be identified as a penalty term, which is necessary to stabilize the method. Since the scalar valued penalty factor θ depends on the discretization, it will be specified later.

Remark 6.3.1 *This particular choice of the interfacial energy contribution can be motivated by the following consideration. If we look at both parts of the body separately and set up the total potential energy while taking into account the interface contributions of the Piola stresses, we obtain*

$$\Pi(\boldsymbol{\varphi}) = \int_{\mathcal{B}^+ \cup \mathcal{B}^-} \Psi(\mathbf{F}(\boldsymbol{\varphi})) dV + \int_{\Gamma} \boldsymbol{\varphi}^+ \cdot \mathbf{P}^+ \cdot \mathbf{N} dA - \int_{\Gamma} \boldsymbol{\varphi}^- \cdot \mathbf{P}^- \cdot \mathbf{N} dA - \int_{\partial \mathcal{B}_i} \boldsymbol{\varphi} \cdot \mathbf{T}^p dA. \quad (6.3.3)$$

Thereby the different signs of the two interface terms result from the direction of the normal vector \mathbf{N} , which points from \mathcal{B}^+ to \mathcal{B}^- . The definition of the jump term (6.2.3) is utilized and the relation for the jump of a product is inserted $[[ab]] = [[a]]\{b\} + \{a\}[[b]]$, which is only valid if the average term is the mean average, to rewrite the interfacial terms as

$$\int_{\Gamma} [[\boldsymbol{\varphi} \cdot \mathbf{P}]] \cdot \mathbf{N} dA = \int_{\Gamma} [[\boldsymbol{\varphi}]] \cdot \{\mathbf{P}\} \cdot \mathbf{N} + \{\boldsymbol{\varphi}\} \cdot [[\mathbf{P}]] \cdot \mathbf{N} dA. \quad (6.3.4)$$

In a last step the traction equilibrium condition at the interface is included $[[\mathbf{P}]] \cdot \mathbf{N} = \mathbf{0}$, such that the second term vanishes.

As already stated the applicability of this procedure depends on the appearance of the mean average. But since the introduction of the weighted average value follows only from aspects of the discretization, this derivation can act as a motivation.

To obtain the weak formulation we need to take the variation of the total potential energy (6.3.1), which has to become zero

$$\begin{aligned} \delta \Pi(\boldsymbol{\varphi}, \delta \boldsymbol{\varphi}) &= \int_{\mathcal{B}^+ \cup \mathcal{B}^-} \delta \mathbf{F} : \mathbf{P} dV + \int_{\Gamma} [[\delta \boldsymbol{\varphi}]] \cdot \{\mathbf{P}\} \cdot \mathbf{N} dA + \int_{\Gamma} [[\boldsymbol{\varphi}]] \cdot \{\mathbf{A} : \delta \mathbf{F}\} \cdot \mathbf{N} dA \\ &+ \int_{\Gamma} \theta [[\delta \boldsymbol{\varphi}]] \cdot [[\boldsymbol{\varphi}]] dA - \int_{\partial \mathcal{B}_i} \delta \boldsymbol{\varphi} \cdot \mathbf{T}^p dA \doteq 0, \end{aligned} \quad (6.3.5)$$

thereby the tangent operator \mathbf{A} follows as the second derivative of the strain energy density $\mathbf{A} = \partial^2 \Psi / \partial \mathbf{F}^2 = \partial \mathbf{P} / \partial \mathbf{F}$. If the average term, containing the tangent operator is summarized as $\{\mathbf{A} : \delta \mathbf{F}\} = \{\delta \mathbf{P}\}$, the resulting weak formulation looks quite similar to Nitsche's method for linear elasticity, compare equation (4.3.5) or for example [41] or [51]. Since the formulation is based on an energy functional it is symmetric.

By means of the divergence theorem and integration by parts it can be shown that the weak formulation (6.3.5) obtained from the principle of stationary potential energy is consistent with the following strong form in the material configuration

$$\begin{aligned} -\text{Div } \mathbf{P} &= \mathbf{0} && \text{in } \mathcal{B} \\ \mathbf{x} &= \mathbf{x}^p && \text{on } \partial\mathcal{B}_x \end{aligned} \quad (6.3.6)$$

$$\mathbf{P} \cdot \mathbf{N}_e = \mathbf{T}^p \quad \text{on } \partial\mathcal{B}_t,$$

which is completed by the conditions along the internal interface

$$\begin{aligned} \llbracket \mathbf{P} \rrbracket \cdot \mathbf{N} &= \mathbf{0} && \text{on } \Gamma \\ \llbracket \varphi \rrbracket &= \mathbf{0} && \text{on } \Gamma. \end{aligned} \quad (6.3.7)$$

The first interfacial condition assures traction continuity along the internal boundary and the second one enforces the continuity of the deformation map.

6.3.2. Linearization

In contrast to the geometrically linear setting the weak form renders a nonlinear equation. To solve the equation numerically the consistent linearization of the weak formulation (6.3.5) is required. Linearizations are denoted by a prefixed Δ .

$$\begin{aligned} \Delta\delta\Pi &= \int_{\mathcal{B}} \delta\mathbf{F} : \mathbf{A} : \Delta\mathbf{F} dV \\ &+ \int_{\Gamma} \llbracket \delta\varphi \rrbracket \cdot \{\mathbf{A} : \Delta\mathbf{F}\} \cdot \mathbf{N} dA + \int_{\Gamma} \llbracket \varphi \rrbracket \cdot \{\llbracket \mathbf{\Xi} : \Delta\mathbf{F} \rrbracket : \delta\mathbf{F}\} \cdot \mathbf{N} dA \\ &+ \int_{\Gamma} \llbracket \Delta\varphi \rrbracket \cdot \{\mathbf{A} : \delta\mathbf{F}\} \cdot \mathbf{N} dA + \int_{\Gamma} \theta \llbracket \Delta\varphi \rrbracket \cdot \llbracket \delta\varphi \rrbracket dA. \end{aligned} \quad (6.3.8)$$

The linearization of the variation of the internal potential energy leads to the first term which contains the tangent operator \mathbf{A} . The linearization of the interface terms leads to four different terms, whereby $\mathbf{\Xi} := \partial\mathbf{A}/\partial\mathbf{F}$ is an sixth order curvature tensor which results from the third derivative of the strain energy function with respect to the deformation map. It is specified in the next subsection 6.4.

6.4. Constitutive equation

For the sake of simplicity we introduce the same strain energy function Ψ as in section 5.4.1 for both parts of the body. We assume hyperelastic material behavior of compressible Neo-Hooke type, which can be characterized by the strain energy density

$$\Psi = \frac{\mu}{2} [(\mathbf{F} \cdot \mathbf{F}^t) : \mathbf{I} - 3] - \mu \ln(J) + \frac{\lambda}{2} \ln^2(J), \quad (6.4.1)$$

whereby μ and λ are the Lamé parameters. In general it is possible to define various constitutive laws for both parts of the body, but here we restrict the differences between the materials to the material parameters. The derivation of the strain energy function with respect to the deformation gradient leads to the definition of the Piola stress

$$\mathbf{P} = \frac{\partial \Psi}{\partial \mathbf{F}} = [\lambda \ln(J) - \mu] \mathbf{F}^{-t} + \mu \mathbf{F}. \quad (6.4.2)$$

The tangent operator \mathbf{A} , which occurs in the weak form or its linearization, respectively, can be specified as

$$\mathbf{A} = \frac{\partial^2 \Psi}{\partial \mathbf{F}^2} = \lambda \mathbf{F}^{-t} \otimes \mathbf{F}^{-t} + [\mu - \lambda \ln(J)] \mathbf{F}^{-t} \underline{\otimes} \mathbf{F}^{-1} + \mu \mathbf{I} \bar{\otimes} \mathbf{I}, \quad (6.4.3)$$

whereby non-standard dyadic products are used, which take the following componentwise representations $\{\bullet \bar{\otimes} \circ\}_{ijkl} = \{\bullet\}_{ik} \otimes \{\circ\}_{jl}$ and $\{\bullet \underline{\otimes} \circ\}_{ijkl} = \{\bullet\}_{il} \otimes \{\circ\}_{jk}$. The curvature tensor Ξ , which is required in the linearization, is given in index notation

$$\begin{aligned} [\Xi]_{ijklmn} &= -\lambda [F_{jm}^{-1} F_{ni}^{-1} F_{lk}^{-1} + F_{ji}^{-1} F_{lm}^{-1} F_{nk}^{-1} + F_{nm}^{-1} F_{li}^{-1} F_{jk}^{-1}] \\ &\quad + [\lambda \ln(J) - \mu] [F_{lm}^{-1} F_{ni}^{-1} F_{jk}^{-1} + F_{li}^{-1} F_{jm}^{-1} F_{nk}^{-1}]. \end{aligned} \quad (6.4.4)$$

6.5. Discretization and linearization

The introduced weak formulation will be solved using finite elements, which allow for a discontinuity intersecting the elements, following the approach suggested in [46] and also applied in [47], [81] and in the previous chapters. The considered elements allow for both, a jump in the deformation map and a jump in its gradient. In the case of weak discontinuities the deformation map shall be continuous, which is globally ensured by means of the additional 'Nitsche' terms in the weak form. Therefore the discretization of the weak form resembles that in the previous chapter. The elements which are crossed by the interface are doubled and hence additional global degrees of freedom are introduced. A new set of discontinuous shape functions is adopted for the discontinuous elements to capture the discontinuity. The size of the two resulting element parts defines the weighting factors $\kappa^{+, -}$, which are equal to the area ratio

$$\kappa^+ = \frac{|\mathcal{B}_d^+|}{|\mathcal{B}_d|} \quad \text{and} \quad \kappa^- = \frac{|\mathcal{B}_d^-|}{|\mathcal{B}_d|}, \quad (6.5.1)$$

compare section 4.5.1.

The reference domain is discretized with n_{el} elements and, following the isoparametric concept, the geometry and the unknown deformation map are approximated by the same shape functions. Furthermore these shape functions are also used for the approximation of the test function, according to the Bubnov-Galerkin technique

$$\mathcal{B} = \bigcup_e \mathcal{B}_e, \quad \mathbf{X}|_{\mathcal{B}_e} = \sum_{i=1}^{n_{en}} N^i \mathbf{X}_i, \quad \varphi|_{\mathcal{B}_e} = \sum_{i=1}^{n_{en}} N^i \varphi_i, \quad \delta\varphi|_{\mathcal{S}_e} = \sum_{i=1}^{n_{en}} N^i \delta\varphi_i. \quad (6.5.2)$$

The approximation of the jump term follows by inserting the above given approximation of the deformation map into the definition (6.2.3)

$$\llbracket \boldsymbol{\varphi} \rrbracket = \sum_{i=1}^{n_{en}^+} N^i|_{\Gamma} \boldsymbol{\varphi}_i^+ - \sum_{i=1}^{n_{en}^-} N^i|_{\Gamma} \boldsymbol{\varphi}_i^- = \sum_{p=1}^{n_{en}^+ + n_{en}^-} J^p \boldsymbol{\varphi}_p. \quad (6.5.3)$$

The jump term is derived at the interface within a discontinuous element and by means of the nodal values of the old and the newly introduced degrees of freedom.

6.5.1. Discrete weak formulation

By means of the described discretization of the primary unknown, the weak formulation (6.3.5) is discretized and the resulting nonlinear system of equations is solved by an iterative Newton-Raphson scheme.

The discrete algorithmic balance of momentum reads

$$\mathbf{R}_I = \mathbf{R}_I^{int} + \mathbf{R}_I^{dis} - \mathbf{R}_I^{ext} = \mathbf{0} \quad (6.5.4)$$

with the particular contributions

$$\begin{aligned} \mathbf{R}_I^{int} &= \mathbf{A}_{e=1}^{n_{el}} \int_{\mathcal{B}_e \cup \mathcal{B}_d} \nabla_X N^i \cdot \mathbf{P} dV \\ \mathbf{R}_I^{dis} &= \mathbf{A}_{e=1}^{n_{el}} \int_{\Gamma_e} J^i \{ \mathbf{P} \} \cdot \mathbf{N} dA + \int_{\Gamma_e} \left[\kappa_e^+ \nabla_X N^{i+} \cdot \tilde{\mathbf{A}}^+ + \kappa_e^- \nabla_X N^{i-} \cdot \tilde{\mathbf{A}}^- \right] dA \\ &\quad + \int_{\Gamma_e} \theta_e J^i \llbracket \boldsymbol{\varphi} \rrbracket dA \\ \mathbf{R}_I^{ext} &= \mathbf{A}_{e=1}^{n_{el}} \int_{\partial \mathcal{B}_{t_e}} N^i \mathbf{T}^p dA. \end{aligned} \quad (6.5.5)$$

The average term of the product $\{ \mathbf{A} : \delta \mathbf{F} \}$, which appears in the continuous equation (6.3.5) has to be splitted in the discrete form. We introduced the abbreviations $\tilde{\mathbf{A}}^{+,-} = [\llbracket \boldsymbol{\varphi} \rrbracket \otimes \mathbf{N}] : \mathbf{A}^{+,-}$.

The weighting factors κ_e are calculated for each part of a splitted element as the area ratio. The scalar penalty factor θ_e depends on the inverse of the element measure h_e and on the material parameters λ and μ . Since an analytical analysis of the penalty factor can not be accomplished in the considered nonlinear case, we define the penalty parameter comparable to the linear elastic case, cf. [41], as $\theta_e := \vartheta[\lambda + \mu]/h_e$, and accomplish a numerical analysis concerning the minimum value of the scalar factor ϑ in section 6.7.

6.5.2. Linearized discrete weak formulation

The above discrete residual statement represents a nonlinear system of equations which can be solved efficiently within the framework of an incremental Newton-Raphson solution strategy. To this end a consistent linearization of the governing equations is performed

$$\mathbf{R}_I^{k+1} = \mathbf{R}_I^k + d\mathbf{R}_I = \mathbf{0} \quad \text{with} \quad d\mathbf{R}_I = \sum_{J=1}^{n_{np}^+ + n_{np}^-} \mathbf{K}_{IJ} d\varphi_J. \quad (6.5.6)$$

To obtain the tangential stiffness matrix \mathbf{K}_{IJ} the linearized weak form (6.3.8) is discretized. This task is straightforward, but since we have to decompose the occurring averages of products the tangential stiffness matrix takes a quite unhandy format

$$\begin{aligned} \mathbf{K}_{IJ}^{int} &= \sum_{e=1}^{n_{el}} \mathbf{A} \int_{\mathcal{B}_e \cup \mathcal{B}_d} \nabla_X N^i \cdot \mathbf{A} \cdot \nabla_X N^j dV \\ \mathbf{K}_{IJ}^{dis} &= \sum_{e=1}^{n_{el}} \int_{\Gamma_e} \left[\kappa_e^+ J^i \hat{\mathbf{A}}^+ \cdot \nabla_X N^{+j} + \kappa_e^- J^i \hat{\mathbf{A}}^- \cdot \nabla_X N^{-j} \right] dA \\ &+ \int_{\Gamma_e} \left[\kappa_e^+ \nabla_X N^{+i} \cdot \hat{\mathbf{A}}^{t+} J^j + \kappa_e^- \nabla_X N^{-i} \cdot \hat{\mathbf{A}}^{t-} J^j \right] dA \\ &+ \int_{\Gamma_e} \left[\kappa_e^+ \nabla_X N^{+i} \cdot \tilde{\mathbf{E}}^+ \cdot \nabla_X N^{+j} + \kappa_e^- \nabla_X N^{-i} \cdot \tilde{\mathbf{E}}^- \cdot \nabla_X N^{-j} \right] dA \\ &+ \int_{\Gamma_e} \theta_e J^i J^j dA, \end{aligned} \quad (6.5.7)$$

where we further introduced the abbreviations $\hat{\mathbf{A}}$, $\hat{\mathbf{A}}^t$ and $\tilde{\mathbf{E}}$ which are defined as

$$\hat{A}_{ikl} = A_{ijkl} N_j, \quad \hat{A}_{ikl}^t = \hat{A}_{kli} \quad \text{and} \quad \tilde{\mathbf{E}}^{+,-} = [[\boldsymbol{\varphi}] \otimes \mathbf{N}] : \boldsymbol{\Xi}^{+,-}. \quad (6.5.8)$$

As expected the tangential stiffness matrix turns out to be symmetric.

6.6. Implementation

The implementation of the proposed method follows the one described in section 4.6 and is shortly summarized here. The geometry of the interface is defined by means of level set functions. Thereby the interface is represented by the zeros of a function $l(\mathbf{X}, t)$ which is one dimension higher than the underlying problem. The function values of l on the node of the finite element mesh decide whether a node is on one side or on the other side of the interface, which leads to a simple algorithm to identify the splitted elements.

The introduction of the additional degrees of freedom follows the same procedure as in section 4.6. Since the interface is static, the introduction of the additional nodes and

the identification of the splitted elements can be executed in a preprocessing step. The nodal values of the level set function are calculated and if an element contains nodes with different signs of the nodal values of l , the element is intersected by the interface. Thus the intersection points of the level set and the element edges and the area of the element subdomains are determined and stored. The algorithm of a simulation is sketched in table 6.1. The integration of the weak form is accomplished by a subtriangulation of the intersected elements and usual Gauss integration in the subdomains.

| |
|--|
| identification of splitted elements, determination of intersection points |
| loop over load steps |
| global Newton iteration |
| loop over all continuous elements \mathcal{B}_e |
| determine element residua \mathbf{R}_e^{int} and their derivatives \mathbf{K}_e^{int} |
| loop over all discontinuous elements \mathcal{B}_d |
| determine the contributions of the element subdomains to \mathbf{R}_e^{int} and \mathbf{K}_e^{int} |
| determine interface residua \mathbf{R}_e^{dis} and their derivatives \mathbf{K}_e^{dis} |
| assemble global residual \mathbf{R} and tangent stiffness matrix \mathbf{K} |
| solve system of equation, check convergence |
| determine state of equilibrium |

Table 6.1.: Algorithm of the approach

6.7. Numerical examples

In the case of weak discontinuities one major task is to numerically investigate the influence of the penalty parameter ϑ on the solution. Therefore a simple example, a bimaterial bar, is considered. By means of a very coarse discretization with only two elements an eigenvalue study is accomplished to obtain information about the minimal size of the penalty parameter during a simulation. Moreover the bimaterial bar is utilized to check the convergence behavior of the approach with respect to mesh refinement. In the second example a plate with a soft circular inclusion is simulated, to analyze the stress and strain distributions.

6.7.1. Bimaterial bar

The bimaterial bar exhibits a material interface, which does not correspond to the mesh-lines. The bar is fixed on the left hand side and loaded by prescribed displacements on the right hand side, as indicated in figure 6.2. To get a first idea of the influence of the

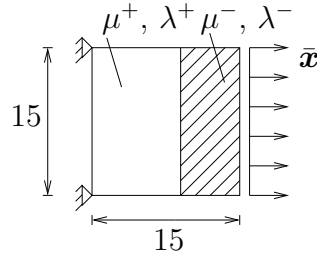


Figure 6.2.: Geometry and loading conditions of bimaterial bar

penalty parameter we assume that the bar consists only of one material, but nevertheless the interface is introduced and Nitsche's method is applied to glue together the two parts of the bar. To check the influence of the penalty parameter numerically an eigenvalue analysis of the tangential stiffness matrix is carried out. Therefore the bar is discretized

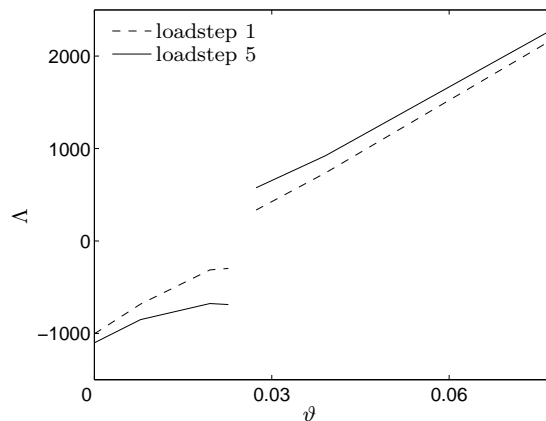


Figure 6.3.: Eigenvalues vs. penalty parameter

with only two triangular elements. The prescribed displacement is applied in five equal steps of 1.0 and the penalty parameter is varied. The material parameters are chosen as $\mu^+ = \mu^- = 77000$ and $\lambda^+ = \lambda^- = 115000$. The smallest eigenvalues of the tangential stiffness matrix of the first and the fifth loadstep are displayed in figure 6.3. In the considered example the method does not converge if the penalty factor is approximately $\vartheta \approx 0.025$. The reason for this can be found in the eigenvalue analysis: if $\vartheta \approx 0.025$, the smallest eigenvalue Λ is approximately zero, which means that the stiffness matrix becomes singular (which explains the gap in the graphical presentation). If $\vartheta < 0.025$,

the method converges but at least one eigenvalue is smaller than zero and the tangential stiffness matrix is not positive definite. The desired result is obtained, if $\vartheta \gg 0.025$: all eigenvalues of the tangential stiffness matrix are positive and \mathbf{K} is positive definite. In contrast to the linear case, the tangential stiffness matrix is varying in each load step and furthermore in each iteration increment. In order to obtain information about the

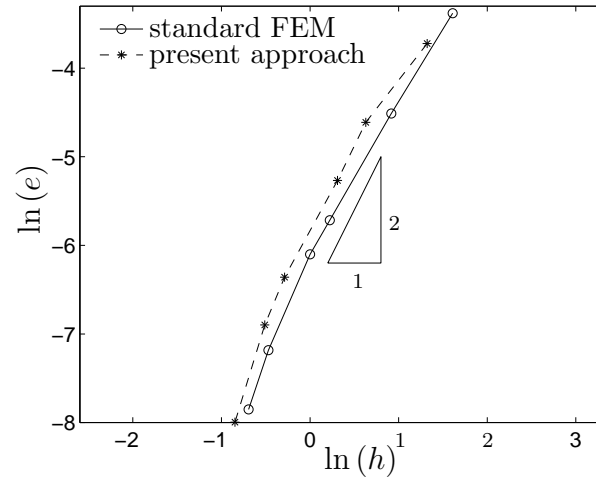


Figure 6.4.: Relative error in the total energy

development of the tangent stiffness during the deformation, the minimal eigenvalues of the stiffness matrix of the first and the final loadstep are compared in figure 6.3. For sufficiently large penalty parameter $\vartheta > 0.025$ the eigenvalues in loadstep 5 exceed these in loadstep 1, which implies that, if the penalty is large enough for the first loadstep it will be sufficient for the following ones as well. In consideration of the aforementioned results and taking into account the experiences we made by means of different numerical examples, we reason, that the penalty factor has to be sufficiently large, but does not need to change during the computation.

In the next step a 'real' bimaterial bar is considered. The penalty parameter is kept constant and the discretization is refined in order to check the convergence behavior of the method. The material parameters are fixed to $\lambda^+ = 115000$, $\mu^+ = 77000$ and $\lambda^- = 11500$, $\mu^- = 7700$. The interface is introduced, such that it does not coincide with the mesh-lines, and the prescribed displacement is equal to 5.0. Taking into account the results from the eigenvalue analysis, a sufficiently large penalty factor is chosen, namely $\vartheta = 5$ and $\theta_e = \vartheta [\lambda_{max} + \mu_{max}] / h_e$. Since an analytical solution for the present nonlinear example can not be provided, the solution of an FE calculation with 4050 elements and an explicitly meshed interface is used as a reference solution. The simulation is carried out with six different discretization and the relative error in the energy is determined as $e = |\Pi^{ref} - \Pi| / \Pi^{ref}$. The results for the present method in comparison with the results of a fitted standard finite element calculation are pictured in figure 6.4. The present

approach shows approximately the same convergence behavior as the standard finite element method, where the mesh lines are enforced to coincide with the interface.

6.7.2. Plate with inclusion

The second example deals with a plate with a soft circular inclusion. Since the problem is symmetric it is sufficient to simulate only one quarter of the structure. The geometry and the loading conditions are given in figure 6.5. The circular interface is introduced via

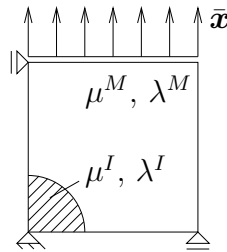


Figure 6.5.: Geometry and loading conditions, plate with circular inclusion

the zero level set of the simple function

$$L(\mathbf{X}) = [\mathbf{X} - \mathbf{X}_m] \cdot [\mathbf{X} - \mathbf{X}_m] - r^2 = 0 \quad (6.7.1)$$

whereby r is the radius of the circle and \mathbf{X}_m its center. The structure is loaded by prescribed displacements. The material parameters for the matrix and the inclusion are

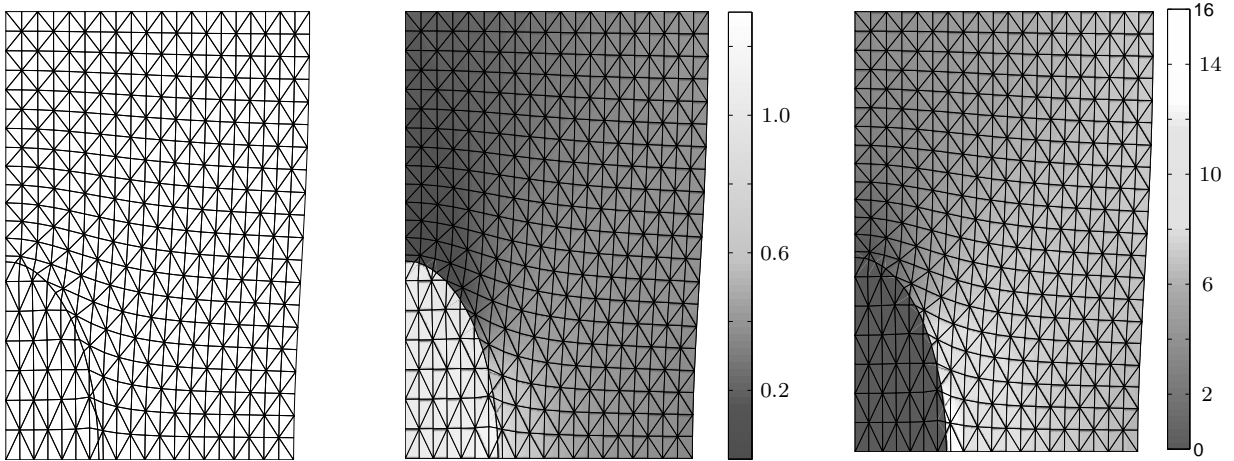


Figure 6.6.: Deformation, Green-Lagrange strains E_{22} , Cauchy stresses σ_{22}

defined as $\lambda^M = 11500$, $\mu^M = 77000$, $\lambda^I = 1150$ and $\mu^I = 770$. The penalty parameter is set to $\vartheta = 5$. In figure 6.6 the deformation of the structure, the distribution of the

Cauchy stresses σ_{22} and the Green-Lagrange strains E_{22} are pictured. As expected there are no visible jumps in the deformation map along the internal interface. The jumps in the stresses and strains are correctly determined along the internal interface and the stress and strain distributions are independent of the mesh geometry.

6.8. Summary

In the present chapter a method for the mesh-independent modeling of weak discontinuities at finite strains was introduced. The method combines the discontinuous elements, which were also applied for the modelling of propagating cracks, with Nitsche's method. Nitsche's method is extended to finite strains and applied along the discontinuity surface to enforce the continuity of the deformation map. Two numerical example verify that the method offers a numerical technique to simulate material interfaces independent of the element boundaries. The jump in the strain field is correctly captured and the convergence is comparable to a simulation with a meshed interface.

7. Conclusions

In the present work different numerical approaches for the incorporation of strong and weak discontinuities in the framework of the finite element method were introduced. The expressions strong and weak discontinuities denote either jumps in the displacement field or jumps in the strains. Strong discontinuities characterize for example cracks whereby weak discontinuities occur at material interfaces.

In the first chapter the development of strong discontinuities was restricted to particular failure surfaces. As the most natural choice interface elements were placed along the known failure surface. The characteristics of the approach is the weak enforcement of the continuity of the displacement field in the precritical state by a discontinuous Galerkin method. Thus the unphysical use of a 'dummy' stiffness was avoided.

In the following four chapters a unified framework for the mesh-independent modeling of strong and weak discontinuities in the geometrically linear and nonlinear setting was presented. A new class of discontinuous elements was formulated, which allows for the description of the discontinuity independently of the underlying mesh. The elements which are intersected by the discontinuity get additional degrees of freedom such that the element is doubled. The additional degrees of freedom are global, this permits a continuous representation of the discontinuity path. A set of discontinuous basis functions is formulated by means of two copies of the usual basis functions. One set is put to zero on one side of the discontinuity while it takes its usual values on the other side and vice versa. This set of discontinuous basis functions can be easily constructed for different types of elements of higher order and dimension and makes the approach highly flexible. In chapter 3 the discontinuous elements were applied for the modeling of cohesive crack propagation in the geometrically linear setting. Inelastic and dissipative processes were restricted to the discontinuity surface and modeled by a cohesive traction separation law. A failure criterion and a method to determine the crack propagation direction was developed. The capability of the approach was presented by numerical examples in two dimensions. The results reflected the ability of the method to simulate mesh-independent discontinuities.

The same discontinuous elements were applied in the next chapter to model weak discontinuities. The geometry of the interfaces was described by means of level set functions. To achieve the desired continuity of the displacement field, the discontinuous Galerkin method, which was applied in chapter 2, was adopted along the interfaces in the elements. This led to an additional interface contribution in the weak form, which was algorithmically handled in a similar manner as the cohesive energy contribution in the strong

discontinuity approach. This method was adopted to solve two numerical examples with material interfaces. The numerical solutions were compared with the analytical one and optimal convergence rates were obtained.

In chapter 5 the extension of the approach for cohesive crack modeling to finite strains was presented. The kinematics were extensively described. The differences compared to the geometrically linear setting were mainly found in the description of the discontinuity surface and in the formulation and linearization of the traction separation law. The approach was extended to the three dimensional modeling of planar crack growth. Implementational details of three dimensional crack propagation, concerning the discrete crack path and crack tip description and the numerical integration of the discontinuous elements were given. The performance of the method was verified by means of numerical examples in two and three dimensions.

The next chapter described the extension of the approach for the modeling of weak discontinuities to finite strains. The focus is the extension of the discontinuous Galerkin method to the geometrically nonlinear regime. A numerical study concerning the size of the penalty parameter was accomplished and the method was applied to problems including material interfaces. The results showed the capability of the method to capture the jump in the strains independent of the underlying mesh.

The developed approach for the mesh-independent modeling of strong and weak discontinuities implies the possibility of further developments in different directions. One task can be the introduction of a more sophisticated crack initiation and propagation criterion, since the applied principle stress criterion has its restrictions and can lead to physically unreasonable crack-paths. The Material Force Method which is studied in appendix C for a linear elastic fracture mechanics problem, can be a promising alternative. Furthermore the incorporation and analysis of different traction separation relations can be studied. Naturally the comparison with experiments would be necessary to adapt the cohesive laws and the parameters to particular materials.

From the numerical viewpoint the introduction of intersecting cracks can be interesting, as well as the extension of the three dimensional approach to nonplanar crack growth. Furthermore the development of discontinuous shell elements would broaden the application area of the approach.

The mesh-independent modeling of weak discontinuities becomes more important if moving interfaces are considered. The applied framework makes use of level set functions and can be expanded in a simple way to the modeling of moving interfaces, like phase transformation problems. And finally the application of the Nitsche type discontinuous Galerkin method to different fields, e. g. contact mechanics, domain decomposition methods etc., requires further analysis.

A. Miscellaneous

A.1. Notation

Throughout the work scalar quantities are denoted by nonbold symbols c , vectors and second order tensors are denoted by bold symbols \mathbf{a} and \mathbf{b} or \mathbf{A} and \mathbf{B} . Fourth or higher order tensors are indicated by nonserif bold fonts \mathbf{E} . In the following the frequently used calculation rules and their notations are summarized.

| | | |
|-----------------------------|--|----------------------------|
| contraction | $c = \mathbf{a} \cdot \mathbf{b}$ | $c = a_i b_i$ |
| | $\mathbf{a} = \mathbf{A} \cdot \mathbf{b}$ | $a_i = A_{ij} b_j$ |
| | $\mathbf{A} = \mathbf{B} \cdot \mathbf{C}$ | $A_{ij} = B_{ik} C_{kj}$ |
| double contraction | $c = \mathbf{A} : \mathbf{B}$ | $c = A_{ij} B_{ij}$ |
| | $\mathbf{A} = \mathbf{E} : \mathbf{B}$ | $A_{ij} = E_{ijkl} B_{kl}$ |
| dyadic product | $\mathbf{A} = \mathbf{a} \otimes \mathbf{b}$ | $A_{ij} = a_i b_j$ |
| | $\mathbf{E} = \mathbf{A} \otimes \mathbf{B}$ | $E_{ijkl} = A_{ij} B_{kl}$ |
| nonstandard dyadic products | $\mathbf{E} = \mathbf{A} \overline{\otimes} \mathbf{B}$ | $E_{ijkl} = A_{ik} B_{jl}$ |
| | $\mathbf{E} = \mathbf{A} \underline{\otimes} \mathbf{B}$ | $E_{ijkl} = A_{il} B_{jk}$ |

The second order unit tensor \mathbf{I} is defined as $I_{ij} = \delta_{ij}$ and the fourth order unit tensor \mathbf{I} is determined as $I_{ijkl} = \delta_{ij} \delta_{kl}$.

A.2. Derivatives

In the next part some derivatives which are frequently used, especially for the linearization of particular quantities, are recapitulated

$$\begin{aligned}
\frac{\partial \mathbf{F}}{\partial \mathbf{F}} &= \mathbf{I} \otimes \mathbf{I} & \frac{\partial \mathbf{F}^{-1}}{\partial \mathbf{F}} &= -\mathbf{F}^{-1} \otimes \mathbf{F}^{-t} \\
\frac{\partial \mathbf{F}^t}{\partial \mathbf{F}} &= \mathbf{I} \otimes \mathbf{I} & \frac{\partial \mathbf{F}^{-t}}{\partial \mathbf{F}} &= -\mathbf{F}^{-t} \otimes \mathbf{F}^{-1} \\
\frac{\partial J}{\partial \mathbf{F}} &= J \mathbf{F}^{-t} \\
\frac{\partial |\mathbf{a}|}{\partial \mathbf{a}} &= \frac{\mathbf{a}}{|\mathbf{a}|} & \frac{\partial (\mathbf{a}/|\mathbf{a}|)}{\partial \mathbf{a}} &= \frac{1}{|\mathbf{a}|} \left[\mathbf{I} - \frac{\mathbf{a}}{|\mathbf{a}|} \otimes \frac{\mathbf{a}}{|\mathbf{a}|} \right].
\end{aligned} \tag{A.2.1}$$

A.3. Jump and average terms

The existence of a discontinuity requires the definition of jump and average terms to deal with the special characteristics at the discontinuity surface. In the present work the jump and average terms of scalar, vectorial and tensorial quantities are defined similarly, that means the jump or average of a field quantity is of the same order as the field quantity itself

$$\begin{aligned}
[[a]] &= a^+ - a^- & [[\mathbf{a}]] &= \mathbf{a}^+ - \mathbf{a}^- & [[\mathbf{A}]] &= \mathbf{A}^+ - \mathbf{A}^- \\
\{a\} &= \frac{1}{2} [a^+ + a^-] & \{\mathbf{a}\} &= \frac{1}{2} [\mathbf{a}^+ + \mathbf{a}^-] & \{\mathbf{A}\} &= \frac{1}{2} [\mathbf{A}^+ + \mathbf{A}^-].
\end{aligned} \tag{A.3.1}$$

The jump and average terms of products can be separated following simple algebraic rules which can be summarized as

$$\begin{aligned}
[[ab]] &= [[a]] \{b\} + \{a\} [[b]] \\
\{ab\} &= \frac{1}{4} [[a]] [[b]] + \{a\} \{b\} \\
[[abc]] &= [[a]] \{b\} \{c\} + \{a\} [[b]] \{c\} + \{a\} \{b\} [[c]] + \frac{1}{4} [[a]] [[b]] [[c]] \\
\{abc\} &= \frac{1}{4} \{a\} [[b]] [[c]] + \frac{1}{4} [[a]] \{b\} [[c]] + \frac{1}{4} [[a]] [[b]] \{c\} + \{a\} \{b\} \{c\}.
\end{aligned} \tag{A.3.2}$$

B. Numerical study of the dG method for linear elasticity

In this section the discontinuous Galerkin method for elasticity is numerically analyzed. To get insight in its convergence behavior and the influence of the penalty parameter a model problem is considered where the dG method is applied between all element boundaries. The results are compared with the analytical solution and the solution of the continuous finite element method.

B.1. DG method for linear elasticity

The use of the discontinuous Galerkin method for linear elasticity, which is applied along certain boundaries in the approaches in the chapters 2 and 4, results in the following weak formulation

$$\begin{aligned} \int_{\mathcal{B}^+ \cup \mathcal{B}^-} \delta \boldsymbol{\epsilon} : \boldsymbol{\sigma} dV + \int_{\Gamma} \left[\llbracket \delta \mathbf{u} \rrbracket \cdot \{ \boldsymbol{\sigma} \} \cdot \bar{\mathbf{n}} + \bar{\mathbf{n}} \cdot \{ \delta \boldsymbol{\sigma} \} \cdot \llbracket \mathbf{u} \rrbracket \right] dA \\ + \int_{\Gamma} \theta \llbracket \delta \mathbf{u} \rrbracket \cdot \llbracket \mathbf{u} \rrbracket dA = \int_{\mathcal{B}^+ \cup \mathcal{B}^-} \delta \mathbf{u} \cdot \mathbf{b} dV + \int_{\partial \mathcal{B}_t} \delta \mathbf{u} \cdot \mathbf{t}^p dA. \end{aligned} \quad (\text{B.1.1})$$

If the discontinuous Galerkin method is applied in the whole domain, the boundary Γ consists of all interior element boundaries. That means that the overall number of nodes is equal to the number of elements times the number of element nodes. The additional terms along the interior boundaries ensure the continuity of the solution in a weak sense. The factor θ denotes a penalty factor which has to be sufficiently high to ensure stability of the method.

B.2. Numerical example

To gain some insight in the properties and the convergence behavior of the discontinuous Galerkin method for linear elasticity and to study the influence of the penalty parameter, see section 2.4.3, one simple example, which is taken from [51], is calculated. Bilinear quadratic elements are used.

In the example the deformation of a squared plate of the size 1×1 , which is fixed at all sides and loaded by a body force \mathbf{b} , is calculated. The choice of the body force allows for a simple analytical solution of the problem. The body force and the resulting analytical

solution are given as

$$\mathbf{b} = \begin{bmatrix} [\lambda + \mu] [1 - 2x] [1 - 2y] \\ -2\mu y [1 - y] - 2 [\lambda + 2\mu] x [1 - y] \end{bmatrix} \quad \mathbf{u} = \begin{bmatrix} 0 \\ -x y [1 - x] [1 - y] \end{bmatrix}. \quad (\text{B.2.1})$$

To calculate the error of the numerical solution, the numerically calculated displacement field \mathbf{u} is compared to the analytical one \mathbf{u}^a and the error is derived as

$$e = |\mathbf{u}^a - \mathbf{u}|, \quad (\text{B.2.2})$$

To obtain information about the size of the penalty parameter firstly an eigenvalue analysis of the stiffness matrix is accomplished. Therefore the penalty parameter is varied whereby the element size is kept constant. When the penalty factor is sufficiently large, all eigenvalues of the stiffness matrix are positive and the method is stable. For the chosen example the minimum penalty factor turns out to be $\vartheta \approx 2$, with $\theta = \vartheta/h [\lambda + \mu]$. Since the factor ϑ is independent of the element measure h , this minimum value will be used throughout the calculations with a decreasing element size.

In figure B.1 the error in the displacements is plotted against the size of the penalty pa-

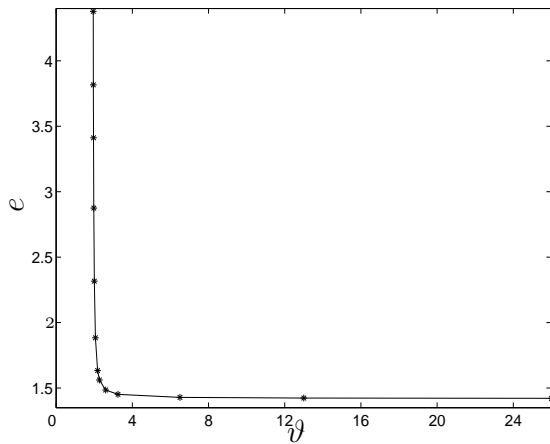


Figure B.1.: Error depending on ϑ

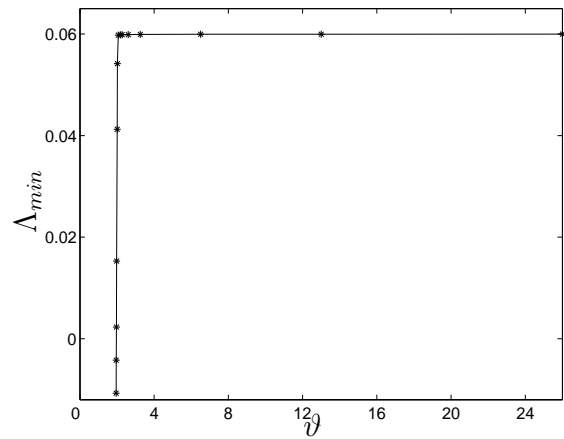


Figure B.2.: Minimal eigenvalue depending on ϑ

rameter. It is clearly visible that the error is highly reduced, when the penalty parameter exceeds its critical value. A further increase of the penalty parameter does not lead to a notable improvement of the results. The relation between the eigenvalues of the stiffness matrix and the error is clarified in figure B.2, where the minimal eigenvalue Λ_{min} of the stiffness matrix is plotted against the penalty parameter. The strong reduction of the error coincides with the change of sign of the minimal eigenvalue.

With the information about the penalty parameter the same example is calculated with different discretizations to check the convergence behavior. Thereby the penalty parameter is kept constant at $\vartheta = 5$. For comparison the example is also calculated with the continuous finite element method. In each case five discretizations are used, with 4, 16,

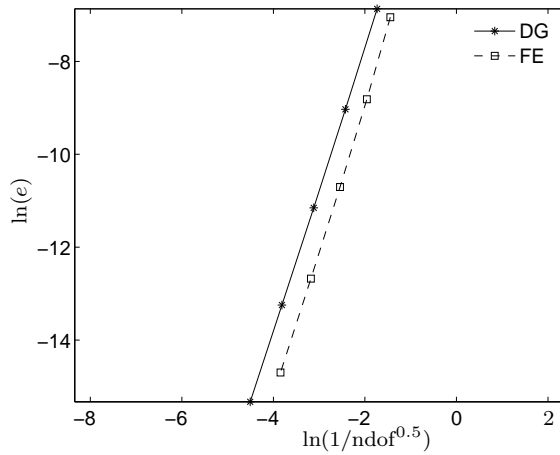


Figure B.3.: Error depending on number of dof

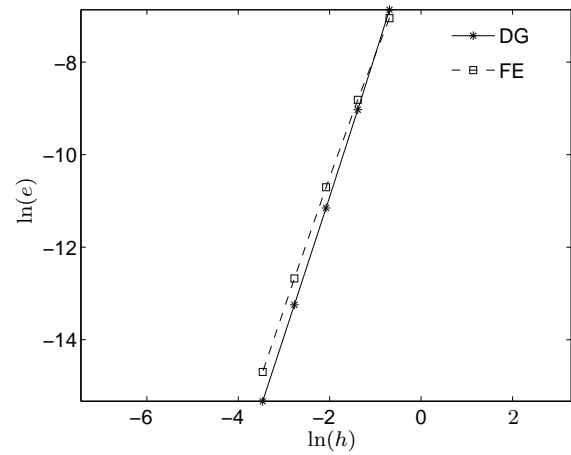


Figure B.4.: Error depending on element size

64, 256 and 1024 elements. Due to the additional degrees of freedom within the discontinuous Galerkin method, the error within the displacement field is plotted against the number of degrees of freedom in figure B.3 and against the element size in figure B.4. The results of the continuous finite element method are shown for comparison. The main result of the numerical study is that the expected quadratic convergence behavior for the discontinuous Galerkin method is obtained. Since we consider a problem with a smooth solution the continuous finite element method is superior due to the lower number of degrees of freedom.

C. Application of the Material Force Method

The method for cohesive crack modelling, which was introduced in chapter 5 for finite strains is here applied for the simulation of traction free cracks. The traction free crack surfaces are simply generated by letting the cohesive tractions vanish. By means of a numerical study the ability of the proposed approach with the discontinuous elements to reproduce classical fracture mechanics quantities like the J-integral is studied.

C.1. Motivation

The main goal of the present study is to investigate the applicability of the Material Force Method in combination with the introduced discontinuous elements in the framework of fracture mechanics. The development of the Material Force Method is essentially based on the exposition of the continuum mechanics of inhomogeneities as comprehensively outlined by Maugin [78], Gurtin [45] and Steinmann [118]. Material forces are considered as the response of variations of material placements of physical particles with respect to the ambient space. Material forces are especially suited for the assesment of general defects as inhomogeneities, interfaces, dislocations and cracks. In fracture mechanics the material forces are directly related to the classical J-integral. First numerical concepts of material forces within the FE method trace back to Braun [22] who derived node point forces from the discretized potential energy with respect to the material node point positions, that contain the material stress in the spirit of Eshelby [37], [38]. The algorithmic representation of the material balance of momentum resulting in the notion of discrete material forces is proposed as the so called Material Force Method, see [117] and [118].

In the present approach discontinuous elements are applied which allow for a representation of the crack independent of the finite element mesh. The construction of the discontinuous elements and the special treatment concerning the integration over the splitted elements are explained in the previous chapters. In the following the Material Force Method is derived, the discrete surface material forces are formulated and details concerning the special discretization are given. Finally a numerical study is accomplished to compare the results of different simulations with an analytical solution.

C.2. Material Force Method

Starting from the spatial balance of momentum $\text{Div} \mathbf{P} = \mathbf{0}$ with the assumption that no body forces act, a pull back to the material configuration is performed by premultiplying the equation with \mathbf{F}^t . With the identity

$$\mathbf{F}^t \cdot \text{Div} \mathbf{P} = \text{Div}(\mathbf{F}^t \cdot \mathbf{P}) - \nabla_X \mathbf{F}^t : \mathbf{P} \quad (\text{C.2.1})$$

and the integrability condition for \mathbf{F}

$$\nabla_X \mathbf{F}^t : \mathbf{P} = \mathbf{P} : \nabla_X \mathbf{F} \quad (\text{C.2.2})$$

the balance of momentum can be rewritten as

$$\text{Div}(\mathbf{F}^t \cdot \mathbf{P}) - \mathbf{P} : \nabla_X \mathbf{F} = \mathbf{0}. \quad (\text{C.2.3})$$

We suppose hyperelastic material behaviour with $\mathbf{P} = \partial \Psi / \partial \mathbf{F}$ and substitute

$$\mathbf{P} : \nabla_X \mathbf{F} = \nabla_X \Psi = \text{Div}(\Psi \mathbf{I}). \quad (\text{C.2.4})$$

The resulting material balance of momentum reads

$$\text{Div}(\mathbf{F}^t \cdot \mathbf{P} - \Psi \mathbf{I}) = \mathbf{0}. \quad (\text{C.2.5})$$

With the definition of the Eshelby stress tensor $\Sigma^t = \Psi \mathbf{I} - \mathbf{F}^t \cdot \mathbf{P}$ the material balance of momentum becomes

$$-\text{Div} \Sigma^t = \mathbf{0}. \quad (\text{C.2.6})$$

The strong form of the material balance of momentum is tested by material virtual displacements $\delta \Phi$. The integration over the domain and the application of the divergence theorem leads to the material virtual work

$$\int_{\partial \mathcal{B}} \delta \Phi \cdot \Sigma^t \cdot \mathbf{N}_e dA = \int_{\mathcal{B}^+ \cup \mathcal{B}^-} \nabla_X \delta \Phi : \Sigma^t dV. \quad (\text{C.2.7})$$

The left hand side can be considered as a virtual surface energy and the right hand side as a virtual internal energy. The boundary of the domain $\partial \mathcal{B}$ includes the crack surfaces, compare figure C.1. The domain is discretized by means of finite elements with shape functions N^i and we end up with the discrete algorithmic material node point forces

$$\mathfrak{F}_{sur,I} = \mathfrak{F}_{int,I} = \mathbf{A}_{e=1}^{n_{el}} \int_{\mathcal{B}^+ \cup \mathcal{B}^-} \Sigma^t \cdot \nabla_X N^i dV. \quad (\text{C.2.8})$$

This material node point forces correspond to variations relative to the ambient material at fixed spatial positions. During the simulation the material forces are calculated in a

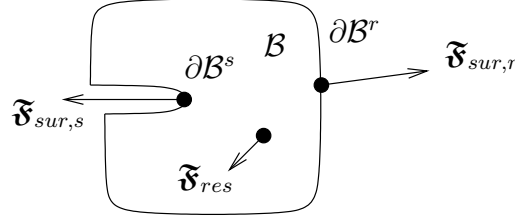


Figure C.1.: Balance of discrete material node point forces

postprocessing step once the spatial problem has been solved.

The boundary of the domain \mathcal{B} is subdivided into a regular part $\partial\mathcal{B}^r$ and a singular part $\partial\mathcal{B}^s$, compare figure C.1. The discrete singular material surface force $\mathfrak{F}_{sur,s}$ acting on the crack tip, thus on the singular part of the boundary, is balanced by the discrete material surface forces on the regular part of the boundary $\mathfrak{F}_{sur,r}$. In addition spurious material forces \mathfrak{F}_{res} within the domain occur which stem from an insufficient discretization accuracy. An improved value for the discrete singular material force can be obtained by the sum of all discrete material forces within the domain, compare [28]

$$\mathfrak{F}_{sur,s} = \sum_{I \in \mathcal{B} \setminus \partial\mathcal{B}^r} \mathfrak{F}_{sur,s,i} + \mathfrak{F}_{res,i}. \quad (\text{C.2.9})$$

In the present approach this result is significant since no node exists at the crack tip and therefore the discrete singular material surface force $\mathfrak{F}_{sur,s}$ can only be calculated by the sum of the discrete material forces within the domain. One has to note that in equation (C.2.9) the sum excludes the regular part of the boundary. Usually this can be taken into account by summing over all nodes except these lying at the regular boundary. The present approach entails the difficulty that no nodes are located at the crack surfaces. That means that these regular material surface forces are distributed among the nodes within the domain. Therefore we restrict our approach to mode I problems where the Eshelby surface tractions at the crack surfaces are balanced and have no influence on the discrete material forces. If unsymmetric problems are considered a boundary integral over the crack surfaces $\Gamma^{+,-}$ has to be calculated to eliminate the contributions of the boundary Eshelby tractions

$$\mathfrak{F}_{sur,\Gamma,I} = \sum_{e=1}^{n_{el}} \int_{\Gamma^+} N^i \Sigma^{t+} \cdot \mathbf{N} dA + \int_{\Gamma^-} N^i \Sigma^{t-} \cdot \mathbf{N} dA. \quad (\text{C.2.10})$$

Thereby $\Sigma^{+,-}$ denotes the Eshelby stress tensor calculated on either side of the discontinuity and \mathbf{N} denotes the normal vector, pointing from \mathcal{B}^- to \mathcal{B}^+ . Then the discrete material surface forces resulting from this boundary integral have to be subtracted from the sum of discrete material forces

$$\mathfrak{F}_{sur,s} = \sum_{I \in \mathcal{B} \setminus (\partial\mathcal{B}^r \setminus \Gamma)} \mathfrak{F}_{sur,s,i} + \mathfrak{F}_{res,i} - \mathfrak{F}_{sur,\Gamma,I}. \quad (\text{C.2.11})$$

However, in the present application we consider only mode I failure, where the Eshelby tractions on the crack surfaces are balanced.

In the present approach discontinuous elements are applied which exhibit additional degrees of freedom. Naturally material node point forces occur at the new nodes which are close to the crack tip. Since the discrete material node point forces constitute the discrete representation of the Eshelby stresses within the elements, the discrete material forces on the new degrees of freedom simply result from the distribution of the Eshelby stress within the 'real' part of the element. Hence the material node point forces of all nodes, old and new ones, are added up to constitute the discrete singular material surface force.

C.3. Numerical example

In the present numerical example a plane strain single edge notched specimen is considered. The specimen is loaded by a uniaxial tensile stress, perpendicular to the notch. The

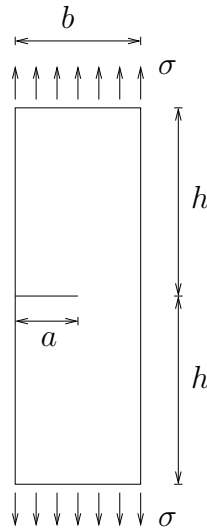


Figure C.2.: Single edge notched specimen

example is selected since the results can be compared with the analytical solution for the stress intensity factors. The geometry of the specimen is given as $a = 5 \text{ mm}$, $b = 10 \text{ mm}$ and $h = 30 \text{ mm}$, compare figure C.2. The tensile stress is $\sigma = 10 \text{ N/mm}^2$ and the material parameters are taken from [118] as $E = 206900 \text{ N/mm}^2$ and $\nu = 0.29$. Lateral movements of the nodes at the top and bottom surface are unconstrained. The applied load magnitude along with the material parameters results in small deformations and avoids geometrical nonlinearities.

The simulation is accomplished with four different discretizations with 625, 1178, 1734 and 2336 linear triangular elements to check the convergence of the method. The notch is introduced through the elements, independent of the discretization. The analytical

solution for the stress intensity factor is taken from [107] and specifies the stress intensity factor for the present geometry as $K_1/K_0 = 2.8425$ with $K_0 = \sigma\sqrt{\pi a}$. The results for the singular material node point force, which are obtained in the simulation are converted into comparable stress intensity factors. Only the contribution of the material force parallel to the crack surfaces $\mathfrak{F}_{sur,s}^1$ is considered, which is equivalent to the classical J-integral. However, the contribution of the material force perpendicular to the crack surfaces is approximately zero. The relation between the stress intensity factors and the J-integral is given as $K_1 = \sqrt{J E'}$ with $E' = E/(1 - \nu^2)$ for plane strain conditions. Table C.1 summarizes the stress intensity factors, calculated with different discretizations, and the errors in comparison with the analytical solution. The results show significant deviations

| n_{el} | $\sqrt{\mathfrak{F}_{sur,s}^1 E' / (\sigma^2 \pi a)}$ | deviation |
|----------|---|-----------|
| 625 | 2.477 | 12.86 % |
| 1178 | 2.532 | 10.92 % |
| 1734 | 2.648 | 6.84 % |
| 2336 | 2.682 | 5.64 % |

Table C.1.: Convergence of discrete material force

compared to the analytical results but also imply convergence towards the reference value. The smallest relative error is equal to 5.64%. The magnitude of the errors is due to the insufficient approximation of the singular stress distribution close to the crack tip. The utilized linear triangular elements can not accurately reproduce the stresses and this is reflected in the high errors of the derived material forces. An improvement of the results can be obtained by taking into account the singular stress distributions by special crack tip elements as in [118] or by the use of special enrichment functions in the vicinity of the crack tip, as supposed in [87]. However, the present results are effectively equal to the results obtained by standard finite element computations with comparable meshes and an explicitly meshed crack.

Bibliography

- [1] ALFANO, G. & M. A. CRISFIELD [2001]. ‘Finite element interface models for the delamination analysis of laminated composites: mechanical and computational issues.’ *International Journal for Numerical Methods in Engineering*, **50**, pp. 1701–1736.
- [2] AREIAS, P. M. A. & T. BELYTSCHKO [2005]. ‘Analysis of three-dimensional crack initiation and propagation using the extended finite element method.’ *International Journal for Numerical Methods in Engineering*, **63**(5), pp. 760–788.
- [3] AREIAS, P. M. A. & T. BELYTSCHKO [2005]. ‘Non-linear analysis of shells with arbitrary evolving cracks using XFEM.’ *International Journal for Numerical Methods in Engineering*, **62**, pp. 384–415.
- [4] ARMERO, F. [1999]. ‘Large-scale modeling of localized dissipative mechanisms in a local continuum: applications to the numerical simulation of strain localization in rate-dependent inelastic solids.’ *Mechanics of Cohesive-Frictional Materials*, **4**, pp. 101–131.
- [5] ARMERO, F. & K. GARIKIPATI [1996]. ‘An analysis of strong discontinuities in multiplicative finite strain plasticity and their relation with the numerical simulation of strain localization in solids.’ *International Journal of Solids and Structures*, **33**, pp. 2863–2885.
- [6] ARNOLD, D. N. [1982]. ‘An interior penalty finite element method with discontinuous elements.’ *SIAM Journal on Numerical Analysis*, **19**(4), pp. 742–760.
- [7] ARNOLD, D. N., F. BREZZI, B. COCKBURN & L. D. MARINI [2002]. ‘Unified analysis of discontinuous Galerkin methods for elliptic problems.’ *SIAM Journal on Numerical Analysis*, **39**(5), pp. 1749–1779.
- [8] BABUŠKA, I. [1970]. ‘The finite element method for elliptic equations with discontinuous coefficients.’ *Computing*, **5**, pp. 207–213.
- [9] BABUŠKA, I. & J. M. MELENK [1997]. ‘The partition of unity method.’ *International Journal for Numerical Methods in Engineering*, **40**, pp. 727–758.
- [10] BARENBLATT, G. I. [1962]. ‘The mathematical theory of equilibrium of cracks in brittle fracture.’ *Advances in Applied Mechanics*, **7**, pp. 55–129.
- [11] BARRETT, J. W. & C. M. ELLIOT [1987]. ‘Fitted and unfitted finite-element methods for elliptic equations with smooth interfaces.’ *IMA Journal of Numerical Analysis*, **7**, pp. 283–300.
- [12] BATHE, K.-J. [1996]. *Finite Element Procedures*. Prentice Hall.

- [13] BECKER, R., P. HANSBO & R. STENBERG [2003]. ‘A finite element method for domain decomposition with non-matching grids.’ *Mathematical Modelling and Numerical Analysis*, **37**, pp. 209–225.
- [14] BELYTSCHKO, T. & T. BLACK [1999]. ‘Elastic crack growth in finite elements with minimal remeshing.’ *International Journal for Numerical Methods in Engineering*, **45**, pp. 601–620.
- [15] BELYTSCHKO, T., H. CHEN, J. XU & G. ZI [2003]. ‘Dynamic crack propagation based on loss of hyperbolicity and a new discontinuous enrichment.’ *International Journal for Numerical Methods in Engineering*, **58**(1873-1905).
- [16] BELYTSCHKO, T., J. FISH & B. E. ENGELMANN [1988]. ‘A finite element with embedded localization zones.’ *Computer Methods in Applied Mechanics and Engineering*, **70**, pp. 59–89.
- [17] BELYTSCHKO, T., N. MOËS, S. URSUI & C. PARIMI [2001]. ‘Arbitrary discontinuities in finite elements.’ *International Journal for Numerical Methods in Engineering*, **50**, pp. 993–1013.
- [18] BOLZON, G. & A. CORIGLIANO [2000]. ‘Finite elements with embedded displacement discontinuity: a generalized variable formulation.’ *International Journal for Numerical Methods in Engineering*, **49**(1227-1266).
- [19] BONET, J. & R. D. WOOD [1997]. *Nonlinear continuum mechanics for finite element analysis*. Cambridge University Press.
- [20] DE BORST, R. [2001]. ‘Some recent issues in computational failure mechanics.’ *International Journal for Numerical Methods in Engineering*, **52**, pp. 63–95.
- [21] DE BORST, R., M. A. GUTIÉRREZ, G. N. WELLS, J. J. C. REMMERS & H. ASKES [2004]. ‘Cohesive-zone models, higher-order continuum theories and reliability methods for computational failure analysis.’ *International Journal for Numerical Methods in Engineering*, **60**, pp. 289–315.
- [22] BRAUN, M. [1997]. ‘Configurational forces induced by finite-element discretization.’ *Proc. Estonian Acad. Sci. Phys. Math.*, **46**(24-31).
- [23] CAMACHO, G. T. & M. ORTIZ [1996]. ‘Computational modelling of impact damage in brittle failure.’ *International Journal of Solids and Structures*, **33**(20-22), pp. 2899–2938.
- [24] CHESSA, J. & T. BELYTSCHKO [2003]. ‘An extended finite element method for two-phase fluids.’ *Journal of Applied Mechanics*, **70**(1), pp. 10–17.
- [25] CHESSA, J., P. SMOLINSKI & T. BELYTSCHKO [2002]. ‘The extended finite element method (XFEM) for solidification problems.’ *International Journal for Numerical Methods in Engineering*, **53**(8), pp. 1959–1977.

-
- [26] COCKBURN, B., G. E. KARNIADAKIS & C.-W. SHU [2000]. *Discontinuous Galerkin Methods: Theory, Computation and Applications*. Springer-Verlag.
- [27] DAUX, C., N. MOËS, J. DOLBOW, N. SUKUMAR & T. BELYTSCHKO [2000]. ‘Arbitrary branched and intersecting cracks with the extended finite element method.’ *International Journal for Numerical Methods in Engineering*, **48**, pp. 1741–1760.
- [28] DENZER, R., F. J. BARTH & P. STEINMANN [2003]. ‘Studies in elastic fracture mechanics based on the material force method.’ *International Journal for Numerical Methods in Engineering*, **58**, pp. 1817–1835.
- [29] DOLBOW, J., N. MÖES & T. BELYTSCHKO [2000]. ‘Modeling fracture in Mindlin-Reissner plates with the extended finite element method.’ *International Journal of Solids and Structures*, **37**, pp. 7161–7183.
- [30] DOLBOW, J., N. MÖES & T. BELYTSCHKO [2001]. ‘An extended finite element method for modeling crack growth with friction contact.’ *Computer Methods in Applied Mechanics and Engineering*, **190**, pp. 6825–6846.
- [31] DOLBOW, J. E. [1999]. *An Extended Finite Element Method with Discontinuous Enrichment for Applied Mechanics*. Ph.D. thesis, Northwestern University, Evanston, Illinois, USA.
- [32] DOLBOW, J. E., E. FRIED & H. JI [2004]. ‘Chemically-induced swelling of hydrogels.’ *Journal of the Mechanics and Physics of Solids*, **52**(1), pp. 51–84.
- [33] DOUGLAS, J., J. & T. DUPONT [1976]. ‘Interior penalty procedures for elliptic and parabolic galerkin methods.’ *Lecture Notes in Physics, Springer-Verlag, Berlin*, **58**.
- [34] DUGDALE, D. S. [1960]. ‘Yielding of steel sheets containing slits.’ *Journal of Mechanics and Solids*, **8**, pp. 100–108.
- [35] EHRLICH, D. & F. ARMERO [2005]. ‘Finite element methods for the analysis of softening plastic hinges in beams and frames.’ *Computational Mechanics*, **35**, pp. 237–264.
- [36] ENGEL, G., K. GARIKIPATI, T. J. R. HUGHES, M. G. LARSON, L. MAZZEI & R. L. TAYLOR [2002]. ‘Continuous/discontinuous finite element approximations of fourth order elliptic problems in structural and continuum mechanics with application to thin beams and plates, and strain gradient plasticity.’ *Computer Methods in Applied Mechanics and Engineering*, **191**, pp. 3669–3750.
- [37] ESHELBY, J. D. [1951]. ‘The force on an elastic singularity.’ *Philosophical transactions of the Royal Society of London A*, **244**, pp. 87–112.
- [38] ESHELBY, J. D. [1975]. ‘The elastic energy-momentum tensor.’ *J. Elasticity*, **5**, pp. 321–335.
- [39] FALK, M. L., A. NEEDLEMAN & J. RICE [2001]. ‘A critical evaluation of cohesive zone models of dynamic fracture.’ *Journal de Physique*, **5**, pp. 43–50.

- [40] FERNÁNDEZ-MÉNDEZ, S. & A. HUERTA [2004]. ‘Imposing essential boundary conditions in mesh-free methods.’ *Computer Methods in Applied Mechanics and Engineering*, **193**, pp. 1257–1275.
- [41] FRITZ, A., S. HÜBER & B. I. WOHLMUTH [2003]. ‘A comparison of mortar and nitsche techniques for linear elasticity.’ *Preprint, Universität Stuttgart*, **008**.
- [42] GASSER, T. C. & G. A. HOLZAPFEL [2003]. ‘Geometrically non-linear and consistently linearized embedded strong discontinuity models for 3d problems with an application to the dissection analysis of soft biological tissues.’ *Computer Methods in Applied Mechanics and Engineering*, **192**, pp. 5059–5098.
- [43] GASSER, T. C. & G. A. HOLZAPFEL [2005]. ‘Modeling 3d crack propagation in unreinforced concrete using PUFEM.’ *Computer Methods in Applied Mechanics and Engineering*, **194**(25-26), pp. 2859–2896.
- [44] GRIEBEL, M. & M. A. SCHWEITZER [2002]. ‘A particle-partition of unity method. Part v: Boundary conditions.’ In *Geometric Analysis and Nonlinear Partial Differential Equations*, edited by S. Hildebrandt & H. Karcher, pp. 517–540. Springer, Berlin.
- [45] GURTIN, M. E. [1999]. *Configurational forces as basic concepts of continuum physics*. Springer.
- [46] HANSBO, A. & P. HANSBO [2002]. ‘An unfitted finite element method, based on Nitsche’s method, for elliptic interface problems.’ *Computer Methods in Applied Mechanics and Engineering*, **191**, pp. 5537–5552.
- [47] HANSBO, A. & P. HANSBO [2004]. ‘A finite element method for the simulation of strong and weak discontinuities in solid mechanics.’ *Computer Methods in Applied Mechanics and Engineering*, **193**, pp. 3523–3540.
- [48] HANSBO, A., P. HANSBO & M. G. LARSON [2003]. ‘A finite element method on composite grids based on Nitsche’s method.’ *Mathematical Modelling and Numerical Analysis*, **37**(3), pp. 495–514.
- [49] HANSBO, P. & M. G. LARSON [2002]. ‘A discontinuous Galerkin method for the plate equation.’ *CALCOLO*, **39**, pp. 41–59.
- [50] HANSBO, P. & M. G. LARSON [2002]. ‘Discontinuous Galerkin methods for incompressible and nearly incompressible elasticity by Nitsche’s method.’ *Computer Methods in Applied Mechanics and Engineering*, **191**, pp. 1895–1908.
- [51] HANSBO, P. & M. G. LARSON [2003]. ‘Discontinuous Galerkin and the Crouzeix-Raviart element: Application to elasticity.’ *Mathematical Modelling and Numerical Analysis*, **37**, pp. 63–72.
- [52] HASHAGEN, F. [1998]. *Numerical analysis of failure mechanisms in fibre metal laminates*. Ph.D. thesis, Technische Universiteit Delft, Delft, Nederlands.

-
- [53] HEINRICH, B. & S. NICAISE [2003]. ‘Nitsche mortar finite element method for transmission problems with singularities.’ *IMA Journal of Numerical Analysis*, **23**, pp. 331–358.
- [54] HEINRICH, B. & K. PIETSCH [2002]. ‘Nitsche type mortaring for some elliptic problem with corner singularities.’ *Computing*, **68**, pp. 217–238.
- [55] HILLERBORG, A., P. E. PETERSSON & M. MODÉER [1976]. ‘Analysis of crack formation and crack growth in concrete by means of fracture mechanics and finite elements.’ *Cement and Concrete Research*, **6**, pp. 773–782.
- [56] HOLZAPFEL, G. A. [2000]. *Nonlinear solid mechanics*. Wiley.
- [57] HUGHES, T. J. R. [2000]. *The Finite Element Method*. Dover Publications.
- [58] JI, H., D. CHOPP & J. E. DOLBOW [2002]. ‘A hybrid extended finite element/ level set method for modeling phase transformations.’ *International Journal for Numerical Methods in Engineering*, **54**, pp. 1209–1233.
- [59] JI, H. & J. E. DOLBOW [2004]. ‘On strategies for enforcing interfacial constraints and evaluating jump conditions with the extended finite element method.’ *International Journal for Numerical Methods in Engineering*, **61**(14), pp. 2508–2535.
- [60] JIRÁSEK, M. [2000]. ‘Comparative study on finite elements with embedded cracks.’ *Computer Methods in Applied Mechanics and Engineering*, **188**, pp. 307–330.
- [61] JIRÁSEK, M. & T. ZIMMERMANN [2001]. ‘Embedded crack model. Part i: basic formulation.’ *International Journal for Numerical Methods in Engineering*, **50**, pp. 1269–1290.
- [62] JIRÁSEK, M. & T. ZIMMERMANN [2001]. ‘Embedded crack model. Part ii: combination with smeared cracks.’ *International Journal for Numerical Methods in Engineering*, **50**, pp. 1291–1305.
- [63] KARIHALOO, B. L. & Q. Z. XIAO [2003]. ‘Modelling of stationary and growing cracks in FE framework without remeshing: a state of the art review.’ *Computers and Structures*, **81**, pp. 119–129.
- [64] KLISINSKI, M., K. RUNESSON & S. STURE [1991]. ‘Finite element with inner softening band.’ *Journal of Engineering Mechanics, ASCE*, **117**, pp. 575–587.
- [65] KRONGAUZ, Y. & T. BELYTSCHKO [1998]. ‘EFG approximation with discontinuous derivatives.’ *International Journal for Numerical Methods in Engineering*, **41**, pp. 1215–1233.
- [66] LARSSON, R. & M. FAGERSTRÖM [2005]. ‘A framework for fracture modelling based on the material forces concept with XFEM kinematics.’ *International Journal for Numerical Methods in Engineering*, **62**(13), pp. 1763–1788.

- [67] LARSSON, R. & N. JANSSON [2002]. ‘Geometrically non-linear damage interface based on regularized strong discontinuities.’ *International Journal for Numerical Methods in Engineering*, **54**, pp. 473–497.
- [68] LARSSON, R., S. P. & K. RUNESSON [1999]. ‘Finite element embedded localization band for finite strain plasticity based on a regularized strong discontinuity.’ *Mechanics of Cohesive-Frictional Materials*, **4**(2), pp. 171–194.
- [69] LARSSON, R., K. RUNESSON & N. S. OTTOSEN [1993]. ‘Discontinuous displacement approximation for capturing plastic localization.’ *International Journal for Numerical Methods in Engineering*, **36**, pp. 2087–2105.
- [70] LEPPIN, C. [2000]. *Ein diskontinuierliches Finite-Elemente-Modell für Lokalisierungsversagen in metallischen und granularen Materialien*. Ph.D. thesis, Universität Hannover, Hannover, Germany.
- [71] LEW, A., P. NEFF, D. SULSKY & M. ORTIZ [2004]. ‘Optimal bv estimates for a discontinuous galerkin method for linear elasticity.’ *Applied Mathematics Research Express*, **3**, pp. 73–106.
- [72] LI, H. & N. CHANDRA [2003]. ‘Analysis of crack growth and crack-tip plasticity in ductile materials using cohesive zone models.’ *International Journal of Plasticity*, **19**, pp. 849–882.
- [73] LI, Z. [1999]. ‘The immersed interface method using a finite element method.’ *Applied Numerical Mathematics*, **27**(3), pp. 253–267.
- [74] LÖBLEIN, J. [2004]. *Ein Modell zur Beschreibung finiter anisotroper elsto-plastischer Deformationen unter Berücksichtigung diskreter Rissausbreitung*. Ph.D. thesis, Universität Duisburg-Essen, Essen, Germany.
- [75] LOFTI, H. R. & P. B. SHING [1995]. ‘Embedded representation of fracture in concrete with mixed finite elements.’ *International Journal for Numerical Methods in Engineering*, **38**(8), pp. 1307–1325.
- [76] MACKINNON, R. J. & G. F. CAREY [1987]. ‘The treatment of material discontinuities in finite element computations.’ *International Journal for Numerical Methods in Engineering*, **24**, pp. 393–417.
- [77] MARSDEN, J. E. & T. J. R. HUGHES [1994]. *Mathematical Foundations of Elasticity*. Dover Publications.
- [78] MAUGIN, G. A. [1993]. *Material Inhomogeneities in Elasticity*. Chapman & Hall, London.
- [79] MELENK, J. M. & I. BABUŠKA [1996]. ‘The partition of unity finite element method: basic theory and applications.’ *Computer Methods in Applied Mechanics and Engineering*, **139**, pp. 289–314.

-
- [80] MERGHEIM, J., E. KUHL & P. STEINMANN [2004]. ‘A hybrid discontinuous Galerkin/interface method for the computational modelling of failure.’ *Communications in Numerical Methods in Engineering*, **20**, pp. 511–519.
- [81] MERGHEIM, J., E. KUHL & P. STEINMANN [2005]. ‘A finite element method for the computational modelling of cohesive cracks.’ *International Journal for Numerical Methods in Engineering*, **63**(2), pp. 276–289.
- [82] MERGHEIM, J., E. KUHL & P. STEINMANN [2005]. ‘A finite element method for the computational modelling of cohesive cracks at large strains.’ *International Journal for Numerical Methods in Engineering*, **submitted**.
- [83] MERGHEIM, J. & P. STEINMANN [2005]. ‘A geometrically nonlinear FE approach for the simulation of strong and weak discontinuities.’ *Computer Methods in Applied Mechanics and Engineering*, **submitted**.
- [84] MIEHE, C. & J. SCHRÖDER [1994]. ‘Post critical discontinuous localization analysis of small-strain softening elastoplastic solids.’ *Archive of Applied Mechanics*, **64**, pp. 267–285.
- [85] MOËS, N. & T. BELYTSCHKO [2002]. ‘Extended finite element method for cohesive crack growth.’ *Engineering Fracture Mechanics*, **69**(7), pp. 813–833.
- [86] MOËS, N., M. CLOIREC, P. CARTRAUD & J. F. REMACLE [2003]. ‘A computational approach to handle complex microstructure geometries.’ *Computer Methods in Applied Mechanics and Engineering*, **192**, pp. 3163–3177.
- [87] MOËS, N., J. DOLBOW & T. BELYTSCHKO [1999]. ‘A finite element method for crack growth without remeshing.’ *International Journal for Numerical Methods in Engineering*, **46**, pp. 131–150.
- [88] MOLARI, L., G. N. WELLS, K. GARIKIPATI & F. UBERTINI [2004]. ‘A discontinuous Galerkin method for strain-gradient-dependent damage: study of interpolations, convergence and two dimensional problems.’ *preprint*, (arXiv:physics/0411022v1).
- [89] MOSLER, J. [2002]. *Finite Elemente mit sprungstetigen Abbildungen des Verschiebungsfeldes für numerische Analysen lokalisierter Versagenszustände in Tragwerken*. Ph.D. thesis, Ruhr-Universität Bochum, Germany.
- [90] MOSLER, J. & G. MESCHKE [2003]. ‘3d modelling of strong discontinuities in elastoplastic solids: fixed and rotating localization formulations.’ *International Journal for Numerical Methods in Engineering*, **57**, pp. 1553–1576.
- [91] NEEDLEMAN, A. [1987]. ‘A continuum model for void nucleation by inclusion debonding.’ *Journal of Applied Mechanics*, **54**, pp. 525–531.
- [92] NEEDLEMAN, A. [1990]. ‘An analysis of decohesion along an imperfect interface.’ *International Journal of Fracture*, **42**, pp. 21–40.

- [93] NGUYEN, O. & N. CHANDRA [2002]. ‘Analysis of energy balance when using cohesive zone models to simulate fracture processes.’ *Engineering Fracture Mechanics*, **124**(4), pp. 440–450.
- [94] NGUYEN, O., E. A. REPETTO, M. ORTIZ & R. A. RADOVITZKY [2001]. ‘A cohesive model of fatigue crack growth.’ *Engineering Fracture Mechanics*, **110**, pp. 351–369.
- [95] NITSCHKE, J. [1970]. ‘Über ein Variationsprinzip zur Lösung von Dirichlet-Problemen bei Verwendung von Teilräumen, die keinen Randbedingungen unterworfen sind.’ *Abh. Math. Univ. Hamburg*, **36**, pp. 9–15.
- [96] OLIVER, J. [1996]. ‘Modelling strong discontinuities in solid mechanics via strain softening constitutive equations. Part 1: fundamentals and Part 2: numerical simulation.’ *International Journal for Numerical Methods in Engineering*, **39**, pp. 3575–3623.
- [97] OLIVER, J., A. E. HUESPE, M. D. G. PULIDO & E. SAMANIEGO [2003]. ‘On the strong discontinuity approach in finite deformation setting.’ *International Journal for Numerical Methods in Engineering*, **56**, pp. 1051–1082.
- [98] OLIVER, J., A. E. HUESPE & E. SAMANIEGO [2003]. ‘A study on finite elements for capturing strong discontinuities.’ *International Journal for Numerical Methods in Engineering*, **56**, pp. 2135–2161.
- [99] ORTIZ, M. [1988]. ‘Microcrack coalescence and macroscopic crack growth initiation in brittle solids.’ *International Journal of Solids and Structures*, **24**, pp. 231–250.
- [100] ORTIZ, M., Y. LEROY & A. NEEDLEMAN [1987]. ‘A finite element method for localized failure analysis.’ *Computer Methods in Applied Mechanics and Engineering*, **61**, pp. 189–214.
- [101] ORTIZ, M. & A. PANDOLFI [1999]. ‘Finite-deformation irreversible cohesive elements for three-dimensional crack-propagation analysis.’ *International Journal for Numerical Methods in Engineering*, **44**, pp. 1267–1282.
- [102] OSHER, S. & J. A. SETHIAN [1988]. ‘Fronts propagating with curvature-dependent speed: Algorithms based on hamilton-jacobi formulations.’ *Journal of Computational Physics*, **79**(1), pp. 12–49.
- [103] PANDOLFI, A., P. KRYSL & M. ORTIZ [1998]. ‘Finite element simulation of ring expansion and fragmentation: the capturing of length and time scales through cohesive models of fracture.’ *International Journal of Fracture*, **95**, pp. 279–297.
- [104] PAPOULIA, K. D., C.-H. SAM & S. A. VAVASIS [2003]. ‘Time continuity in cohesive finite element modeling.’ *International Journal for Numerical Methods in Engineering*, **58**, pp. 679–701.

-
- [105] RIVIÈRE, B., S. SHAW, M. WHEELER & J. R. WHITMAN [2003]. ‘Discontinuous Galerkin finite element methods for linear elasticity and quasistatic linear viscoelasticity.’ *Numerische Mathematik*, **95**, pp. 347–376.
- [106] RIVIÈRE, B. & M. F. WHEELER [2000]. ‘Optimal error estimates for discontinuous Galerkin methods applied to linear elasticity problems.’ *TICAM Report 00-30*.
- [107] ROOKE, D. P. & D. J. CARTWRIGHT [1976]. *Compendium of stress intensity factors*. H.M. Stationary Office, London, UK.
- [108] SCHELLEKENS, J. C. J. [1992]. *Computational strategies for composite structures*. Ph.D. thesis, Technische Universiteit Delft, Delft, Netherlands.
- [109] SCHELLEKENS, J. C. J. & R. DE BORST [1993]. ‘On the numerical integration of interface elements.’ *International Journal for Numerical Methods in Engineering*, **36**, pp. 43–66.
- [110] SCHLANGEN, E. [1993]. *Experimental and numerical analysis of fracture processes in concrete*. Ph.D. thesis, Delft University of Technology, Delft, Netherlands.
- [111] SETHIAN, J. A. [1999]. *Level Set Methods and Fast Marching Methods: Evolving Interfaces in Computational Geometry, Fluid Mechanics, Computer Vision and Material Science*. Cambridge University Press, Cambridge, UK.
- [112] SIMO, J. C. & F. ARMERO [1992]. ‘Geometrically non-linear enhanced strain mixed methods and the method of incompatible modes.’ *International Journal for Numerical Methods in Engineering*, **33**, pp. 1414–1449.
- [113] SIMO, J. C., F. ARMERO & R. L. TAYLOR [1993]. ‘Improved versions of assumed enhanced strain tri-linear elements for 3d finite deformation problems.’ *Computer Methods in Applied Mechanics and Engineering*, **110**, pp. 359–386.
- [114] SIMO, J. C., J. OLIVER & F. ARMERO [1993]. ‘An analysis of strong discontinuities induced by strain-softening in rate-independent inelastic solids.’ *Computational Mechanics*, **12**, pp. 277–296.
- [115] SIMO, J. C. & S. RIFAI [1990]. ‘A class of mixed assumed strain methods and the method of incompatible modes.’ *International Journal for Numerical Methods in Engineering*, **29**, pp. 1595–1638.
- [116] SIMONE, A. [2003]. *Continuous-Discontinuous Modelling of Failure*. Ph.D. thesis, Technische Universiteit Delft, Delft, Netherlands.
- [117] STEINMANN, P. [2000]. ‘Application of material forces to hyperelastostatic fracture mechanics. I. continuum mechanical setting.’ *International Journal of Solids and Structures*, **37**, pp. 7371–7391.
- [118] STEINMANN, P., D. ACKERMANN & F. J. BARTH [2001]. ‘Application of material forces to hyperelastostatic fracture mechanics. II. computational setting.’ *International Journal of Solids and Structures*, **38**, pp. 5509–5526.

- [119] STEINMANN, P. & P. BETSCH [2000]. ‘A localization capturing fe-interface based on regularized strong discontinuities at large inelastic strains.’ *International Journal of Solids and Structures*, **37**, pp. 4061–4082.
- [120] STEINMANN, P. & O. HÄSNER [2005]. ‘On material interfaces in thermomechanical solids.’ *Archive of Applied Mechanics*, DOI: [10.1007/s00419-005-0383-8](https://doi.org/10.1007/s00419-005-0383-8).
- [121] STEINMANN, P., R. LARSSON & K. RUNESSON [1997]. ‘On the localization properties of multiplicative hyperelasto-plastic continua with strong discontinuities.’ *International Journal of Solids and Structures*, **34**, pp. 969–990.
- [122] STENBERG, R. [1998]. ‘Mortaring by a method of Nitsche.’ In *Computational Mechanics, New Trends and Applications*, edited by S. Idelsohn, E. Onate & E. Dvorkin, pp. 1–6. CIMNE, Barcelona, Spain.
- [123] STOLARSKA, M., D. L. CHOPP, N. MÖES & T. BELYTSCHKO [2001]. ‘Modelling crack growth by level sets in the extended finite element method.’ *International Journal for Numerical Methods in Engineering*, **51**(8), pp. 943–960.
- [124] SUKUMAR, N., D. L. CHOPP, N. MÖES & T. BELYTSCHKO [2001]. ‘Modelling holes and inclusions by level sets in the extended finite-element method.’ *Computer Methods in Applied Mechanics and Engineering*, **190**, pp. 6183–6200.
- [125] SUKUMAR, N., N. MÖES, B. MORAN & T. BELYTSCHKO [2000]. ‘Extended finite element method for three-dimensional crack modeling.’ *International Journal for Numerical Methods in Engineering*, **48**(11), pp. 1549–1570.
- [126] TRUESDELL, C. & W. NOLL [1992]. *The non-linear field theories of mechanics*. Springer-Verlag, Berlin.
- [127] TVEERGARD, V. & J. W. HUTCHINSON [1992]. ‘The relation between crack growth resistance and fracture process parameters in elastic-plastic solids.’ *Journal of the Mechanics and Physics of Solids*, **40**, pp. 1377–1397.
- [128] WELLS, G. N. [2001]. *Discontinuous modelling of strain localisation and failure*. Ph.D. thesis, Technische Universiteit Delft, Delft, Netherlands.
- [129] WELLS, G. N., K. GARIKIPATI & L. MOLARI [2004]. ‘A discontinuous Galerkin formulation for a strain gradient-dependent damage model.’ *Computer Methods in Applied Mechanics and Engineering*, **193**, pp. 3633–3645.
- [130] WELLS, G. N. & L. J. SLUYS [2001]. ‘A new method for modelling cohesive cracks using finite elements.’ *International Journal for Numerical Methods in Engineering*, **50**, pp. 2667–2682.
- [131] WELLS, G. N., L. J. SLUYS & R. DE BORST [2002]. ‘A consistent geometrically non-linear approach for delamination.’ *International Journal for Numerical Methods in Engineering*, **54**, pp. 1333–1355.

-
- [132] WELLS, G. N., L. J. SLUYS & R. DE BORST [2002]. ‘Simulating the propagation of displacement discontinuities in a regularized strain-softening medium.’ *International Journal for Numerical Methods in Engineering*, **53**, pp. 1235–1256.
- [133] WHEELER, M. F. [1978]. ‘An elliptic collocation-finite element method with interior penalties.’ *SIAM Journal on Numerical Analysis*, **15**(1), pp. 152–162.
- [134] WIHLER, T. P. [2002]. *Discontinuous Galerkin FEM for Elliptic Problems in Polygonal Domains*. Ph.D. thesis, Swiss Federal Institute of Technology Zürich, Zürich, Switzerland.
- [135] WRIGGERS, P. [2001]. *Nichtlineare Finite-Element-Methoden*. Springer-Verlag.
- [136] WRIGGERS, P. [2002]. *Computational Contact Mechanics*. Wiley-Verlag.
- [137] XU, X. P. & A. NEEDLEMAN [1994]. ‘Numerical simulation of fast crack growth in brittle solids.’ *Journal of the Mechanics and Physics of Solids*, **42**, pp. 1397–1434.
- [138] ZI, G. & T. BELYTSCHKO [2003]. ‘New crack-tip elements for XFEM and applications to cohesive cracks.’ *International Journal for Numerical Methods in Engineering*, **57**, pp. 2221–2240.
- [139] ZIENKIEWICZ, O. C. & R. L. TAYLOR [2000]. *The Finite Element Method, Volume I: The Basis*. Butterworth Heinemann.
- [140] ZIENKIEWICZ, O. C. & R. L. TAYLOR [2000]. *The Finite Element Method, Volume II: Solid Mechanics*. Butterworth Heinemann.

Curriculum Vitae

| | |
|-------------------|---|
| Name | Julia Mergheim |
| Nationality | German |
| Date of Birth | 20. März 1978, Bochum |
| 08/1984 – 06/1988 | Grundschule, Liboriusstraße, Bochum |
| 08/1988 – 05/1997 | Hildegardisgymnasium, Bochum |
| 10/1997 – 09/2002 | Civil Engineering, Ruhr-Universität, Bochum |
| since 10/2002 | Ph.D. Student, University of Kaiserslautern, Chair of Applied Mechanics (Prof. Dr.-Ing. P. Steinmann) |